PRESSURE FIELD ESTIMATION FROM PARTICLE IMAGE VELOCIMETRY DATA

A THESIS SUBMITTED TO
THE GRADUATE SCHOOL OF NATURAL AND APPLIED SCIENCES
OF
MIDDLE EAST TECHNICAL UNIVERSITY

BY

ERKAN GÜNAYDINOĞLU

IN PARTIAL FULFILLMENT OF THE REQUIREMENTS
FOR
THE DEGREE OF DOCTOR OF PHILOSOPHY
IN
AEROSPACE ENGINEERING

SEPTEMBER 2018

Approval of the thesis:

PRESSURE FIELD ESTIMATION FROM PARTICLE IMAGE VELOCIMETRY DATA

submitted by **ERKAN GÜNAYDINOĞLU** in partial fulfillment of the requirements for the degree of **Doctor of Philosophy in Aerospace Engineering Department, Middle East Technical University** by,

Prof. Dr. Halil Kalıpçılar _____
Dean, Graduate School of **Natural and Applied Sciences**

Prof. Dr. Ozan Tekinalp _____
Head of Department, **Aerospace Engineering**

Prof. Dr. D. Funda Kurtuluş _____
Supervisor, **Aerospace Engineering Department, METU**

Examining Committee Members:

Assoc. Prof. Dr. Oğuz Uzol
Aerospace Engineering Department , METU _____

Prof. Dr. D. Funda Kurtuluş
Aerospace Engineering Department , METU _____

Assoc. Prof. Dr. M. Metin Yavuz
Mechanical Engineering Department, METU _____

Assist. Prof. Dr. Mustafa Kaya
Aeronautical Engineering Department, AYBU _____

Assist. Prof. Dr. Munir Elfarra
Aeronautical Engineering Department, AYBU _____

Date: _____

I hereby declare that all information in this document has been obtained and presented in accordance with academic rules and ethical conduct. I also declare that, as required by these rules and conduct, I have fully cited and referenced all material and results that are not original to this work.

Name, Last Name: Erkan Günaydınoğlu

Signature :

ABSTRACT

PRESSURE FIELD ESTIMATION FROM PARTICLE IMAGE VELOCIMETRY DATA

Günaydınoğlu, Erkan
Ph.D., Department of Aerospace Engineering
Supervisor : Prof. Dr. D. Funda Kurtuluş

September 2018, 117 pages

In this thesis, a methodology is proposed to estimate pressure fields from particle image velocimetry measurements. The methodology uses the velocity fields acquired from the experiments as initial and boundary condition and employs Semi-Implicit Method for Pressure Linked Equations algorithm to solve governing equations. Finite volume method is employed with high order discretization scheme for solution of steady and transient flows. The methodology is validated with theoretical flows and further verified with conventional pressure measurement tools. The sensitivity of the methodology to the velocity field error is also assessed. Method estimates the pressure fields exactly for error free velocity fields. Moreover, method can correct the flow-fields to accurate values even with extremely high experimental uncertainties and errors. The methodology is further employed on a flapping airfoil experiment and capability of pressure estimation is tested for highly vortical flows. The proposed methodology offers a reliable, non-intrusive, global pressure measurements simultaneously with the corresponding velocity fields. Due to the error-correcting nature, it could also be used for quantifying the uncertainties of experimental systems or

calibrating numerical tools.

Keywords: Experimental Aerodynamics, Computational Fluid Dynamics, Semi-Implicit Method for Pressure Linked Equations, SIMPLE, Hydrodynamics

ÖZ

PARÇACIK GÖRÜNTÜLEMELİ HIZÖLÇER VERİLERİNDEN BASINÇ ALANI KESTİRİMİ

Günaydınoğlu, Erkan
Doktora, Havacılık ve Uzay Mühendisliği Bölümü
Tez Yöneticisi : Prof. Dr. D. Funda Kurtuluş

Eylül 2018 , 117 sayfa

Bu tezde, parçacık görüntülemeli hızölçer verilerinden basınç alanı elde etmek için bir yöntem önerilmiştir. Önerilen yöntemde, deneylerden elde edilen hız alanları, başlangıç ve sınır koşulu olarak kullanılarak, Basınç Bağlantılı Denklemler için Yarı Örtük Yöntem algoritması ile korunum denklemleri çözülmektedir. Zamandan bağımsız ve daimi akışların çözümleri için yüksek mertebeli ayrıştırma şemaları ile sonlu hacimler yöntemi kullanılmıştır. Önerilen yöntem teorik akışlar ile doğrulanmış ve takiben sonuçlar klasik basınç ölçüm araçları ile karşılaştırılmıştır. Yöntemin, girdi olarak kullanılan hız verilerindeki hatalara karşı duyarlılığı da değerlendirilmiştir. Hata içermeyen hız alanları ile yöntem kesin basınç alanını vermek ile birlikte çok yüksek mertebedeki hatalarda dahi düşük hata ile çözüm verebilmektedir. Yöntemin yüksek girdaplılıklı akışlardaki yeteneğini değerlendirmek için çırpan kanat çevresindeki akışın basınç alanı ölçülmüştür. Önerilen yöntem ile akış alanına müdahale etmeyen, bölgesel ve hız alanı ile eşzamanlı güvenilir basınç ölçümleri yapılabilmektedir. Ayrıca hataları düzelten doğası gereği, önerilen yöntem deneysel sistemlerin belirsizliklerini ölçmek ve hesaplamalı yöntemleri kalibre etmek için de kullanılabilir.

Anahtar Kelimeler: Deneysel Aerodinamik, Hesaplamalı Akışkanlar Dinamiği, Basınç Bağlantılı Denklemler için Yarı Örtük Yöntem, SIMPLE, Hidrodinamik

To my dearest parents Besime and Hıdır Günaydınoğlu...

ACKNOWLEDGMENTS

I would like to express my deep and sincere gratitude to my supervisor Prof. Dr. D. Funda Kurtuluş, whose kindness, patience, academic experience and knowledge is invaluable for me at all steps of this thesis study. Without her enthusiasm, energy and support, I could not be able to complete this study.

I would like to thank my thesis committee members Assoc. Prof. Dr. Oğuz Uzol and Assoc. Prof. Dr. Metin Yavuz for their contributions during semiannual meetings.

I would like to thank Dr. Engin Leblebici, Dr. Kenan Cengiz and Dr. Hooman Hazaveh for technical asisstance and fruitful discussions.

Lastly, but most importantly, I would like to express my eternal gratitude to my parents for their love, support and encouragement throughout my life.

TABLE OF CONTENTS

LIST OF TABLES

TABLES

LIST OF FIGURES

FIGURES

LIST OF SYMBOLS

Roman Symbols

A	Area
a	General coefficient term
b	Mass source term
c	Chord length
C_p	Pressure coefficient
D	Diffusive conductance
F	Convective mass flux per unit area
k	Thermal conductivity
P	Pressure
Pe	Peclet number
q	Dynamic pressure
Re	Reynolds number
S	Source term
St	Strouhal number
t	Time
T	Temperature
u, v	Velocity components
x, y	Spatial Cartesian coordinates
V	Velocity
$\mathcal{V}$	Volume

Greek Symbols

α	Relaxation factor
α	Pitch angle
β	Yaw angle
μ	Dynamic viscosity
ϕ	General flow variable
Γ	Diffusive conductance
Φ	Dissipation function
ρ	Density
θ	Angular position of the airfoil
ω	Vorticity

Subscripts

∞	Free-stream values
$_0$	Characteristic values
N, n	North
S, s	South
E, e	East
W, w	West

Superscripts

$\hat{u}, \hat{v}$	Pseudo-velocities

LIST OF ABBREVIATIONS

AOA	Angle of Attack
CD	Central Differencing
CV	Control Volume
CFD	Computational Fluid Dynamics
DCS	Deferred Correction Source
DNS	Direct Numerical Simulation
FHP	Five Hole Probe
FOV	Field of View
HD	Hybrid Differencing
LUD	Linear Upwind Differencing
PIV	Particle Image Velocimetry
PPE	Pressure Poisson Equation
PSP	Pressure Sensitive Paint
PTV	Particle Tracking Velocimetry
RMS	Root Mean Square
RANS	Reynolds Averaged Navier-Stokes Equation
SIMPLE	Semi Implicit Method for Pressure Linked Equations
SIMPLER	Semi Implicit Method for Pressure Linked Equations Revised
QUICK	Quadratic Upstream Interpolation for Convective Kinetics
TDMA	Tri-diagonal Matrix Algorithm
TVD	Total Variation Diminishing
UD	Upwind Differencing
UMIST	Upstream Monotonic Interpolation for Scalar Transport
WS	Window Size

CHAPTER 1

INTRODUCTION

Pressure measurements are one of the essential tools in aerodynamic design of air vehicles not only in terms of surface loadings but also for the aeroacoustic and other flow-induced loads and phenomena. The former has been successfully measured with techniques ranging from flush-mounted transducers to pressure sensitive paints (PSP) which are matured in time to serve for accuracy, size, frequency response, etc. requirements. Unsteady pressure fields are still demanding alternative measurement techniques for which available conventional tools are partially inadequate due to being either intrusive, pointwise or steady. Recent advances in camera and laser technologies lead to seek possibilities of extracting pressure from particle image velocimetry (PIV) measurements to have non-intrusive, unsteady, global pressure fields simultaneously with corresponding velocity field. Within this context, estimating pressure from PIV measurements has gained significant interest from several investigators since two decades from introduction of the concept [1, 2].

Despite of the significant efforts, still not a consensus is reached on the optimal procedure for pressure estimation from PIV. Most of the studies are based on either integrating the pressure gradient term in the Navier-Stokes equations spatially or solving the Pressure Poisson Equation (PPE) in the flow-field with acquired velocity field. Limited number of studies focus on other methods such as employing computational fluid dynamics (CFD) algorithms, statistical tools, image processing practices, etc. [3–8]. Even if the earlier works on the spatial integration method tried to measure the material acceleration via multiple camera and laser systems [9–15], recent trend is to rely on classical arrangement thanks to the adequately high acquisition rates of PIV systems [16]. Thus, newly developed pressure estimation methods could easily be

implemented to existing PIV systems without any modification.

Spatial integration and PPE solution methods lack due to the fact that neither of them has an error correcting behavior. Thus, recently a great effort is paid to characterize the error sensitivity of these two pressure estimation methods to assess the quality of output [17–22]. Rather than the lack of error correcting nature, there are different sources, which may lead to accumulation of errors. In terms of solution of PPE to achieve pressure field, the problem is twofold. First, PPE is a boundary value problem that requires boundary condition information, which should be supplied by the end user. Even if the use Bernoulli's equation at inviscid boundaries and integration of Navier-Stokes equations at viscous boundaries became a common practice, boundary condition implementation may not be that straightforward for complex flows. Second, the partial differential equations to be solved are in elliptic form, which dictates that any error in the flow-field will be distributed in all directions on the whole flow-field. Since any error in artificially prescribed boundary conditions will accumulate with each iteration, the solution may diverge even with small deviations from the real flow [17]. In spatial integration method, pressure at a point is computed by integrating the pressure gradient spatially from boundaries and naturally, at each integration step numerical errors are accumulated. Due to the great number of integrations, accumulated errors may be significant, even may corrupt the whole data in most of the cases. Several algorithms are proposed [11, 23] to resolve this issue and path sensitivity of integration methods.

Motivation of the thesis is to construct a pressure determination procedure that does not require end-user to prescribe any boundary condition and inherently possesses an error-correcting nature on the input velocity data. To achieve this, Semi Implicit Method for Pressure Linked Equations Revised (SIMPLER) algorithm of Patankar is employed to incompressible steady and transient flows with high order finite volume discretization [24, 25]. Proposed procedure starts with interpolating the acquired velocity data on a staggered computational grid. This experimental velocity field is used as an initial flow-field for the SIMPLER algorithm. Then, continuity equation, in the form of pressure equation for incompressible flows, is solved with this velocity field to have an initial pressure field. Momentum equations are solved with calculated pressure field and then pressure correction equation is solved for calculating the mass

imbalance in continuity equation. Using this mass imbalance term current velocity field is corrected. Repeating this procedure until convergence provides not only pressure field satisfying governing equations, but also the corrections on measured velocity data to force continuity. This corrective behavior promises more than just estimating pressure; such as quantifying the uncertainties in PIV system, assessing error sensitivity of experiments or calibrating the numerical tools.

The thesis consists of six chapters and proceeds as follows: the state-of-art for pressure determination from PIV measurements are reviewed in Chapter 2. Numerical implementation of the SIMPLER algorithm to planar PIV data is described in Chapter 3. Validation of the methodology with analytical flows and error sensitivity studies are reported in Chapter 4. The pressure field estimated from proposed methodology is also validated with the five hole probe results and reported together with an application on a flapping wing PIV experiment in Chapter 5. Finally, the effort spent on the current pressure estimation methodology are concluded in Chapter 6 with recommended future work and possible improvements.

CHAPTER 2

LITERATURE REVIEW

This chapter is devoted to the in-depth review of the literature on pressure estimation methods from PIV. Similarly, a few specific algorithms have been proposed for pressure estimation with particle tracking velocimetry (PTV) data [26–31]. Even if PTV pressure methods are briefly reviewed in this chapter, PTV applications are in generally out of scope of current thesis. On the other hand, if one interpolates the scattered PTV data to a regular grid, the current method may directly be applied to PTV data [32].

Figure 2.1 shows the operating principles of a classical PIV arrangement. The first step in the procedure is to capture a pair of images of laser-illuminated flow-field seeded with neutrally buoyant, homogeneous, flow-tracking particles [33]. The images are divided into interrogation windows containing 10 to 20 particles [34]. The interrogation windows of image pairs are cross-correlated in both directions. The peak value of the cross-correlation denotes collective displacement of the particles in interrogation window. Consequently, dividing the displacement vector to the time difference between the image pairs gives the velocity vector. Since all particles in the same interrogation window result one velocity vector, any velocity gradient in the interrogation window introduces an error. Thus, it is significant to arrange the window size to have smallest possible velocity gradient inside. Detailed information on the principles, applications and recommended practices of PIV could be found in [35,36].

Mainly, two methods, being spatial integration of pressure gradient and solution of pressure Poisson equation, are used in significant portion of the available literature. In the following subsections, these two methods are discussed in terms of their principles, applications and deficiencies. The last subsection reviews other pressure es-

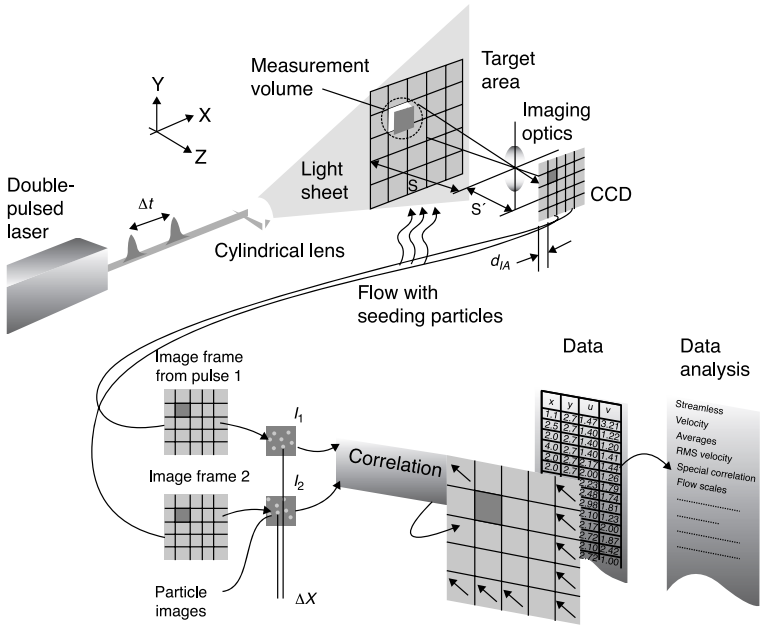

Figure 2.1: Operating principles of particle image velocimetry, depicted from [33], originally from [37].

timation methods which are mostly based on implementation of CFD algorithms for pressure estimation purposes.

2.1 Spatial Integration of Pressure Gradient

The incompressible Navier-Stokes equations with constant viscosity could be arranged as

$$\nabla p = -\rho \frac{\mathrm{D}\vec{V}}{\mathrm{D}t} + \mu \nabla^2 \vec{V} \tag{2.1}$$

where $\vec{V}$, p, ρ, μ and t are velocity, pressure, density, viscosity and time, respectively . The term $\frac{\mathrm{D}\vec{V}}{\mathrm{D}t}$ is material derivative of velocity, which is also referred as material acceleration. The way one approaches the fluid motion results in different ways to calculate material acceleration. If the material acceleration is calculated by tracking fluid particles, the approach is called Lagrangian description of fluid motion and the

material acceleration is given as

$$\frac{\mathrm{D}\vec{V}}{\mathrm{D}t} = \frac{d\vec{V_p}}{dt} = \frac{d\vec{V}(\vec{x_p}, t)}{dt} \tag{2.2}$$

where $\vec{x_p}$ and $\vec{V_p}$ are the position and velocity of the fluid particle at time instant t. This point of view is most suitably for PTV experiments since the method depends on tracking discrete particles in the flow-field. Thus, pressure estimation from PTV is also called as Lagrangian Particle Tracking (LPT) in the available literature due to the extensive employment of Lagrangian point of view for PTV measurements [19]. One of the earlier works is performed by La Porta *et al.* [38] in 2001 by employing a strip detector adapted from high-energy physics to measure particle accelerations in fully developed turbulent flow with an acquisition rate up to 70 kHz. On the other hand, if fluid parcels entering a fixed control volume in space is considered, one would reach Eulerian description of fluid motion. The material acceleration in Eulerian approach is given as

$$\frac{\mathrm{D}\vec{V}}{\mathrm{D}t} = \frac{\partial\vec{V}}{\partial t} + (\vec{V}\cdot\nabla)\vec{V} \tag{2.3}$$

The first term on the right hand side of Equation 2.3 is the local acceleration whereas the second term is known as convective acceleration. Eulerian approach is more applicable to the PIV studies due to the structural similarity between fixed control volumes and interrogation windows [2].

All the terms on the right hand side of Equation 2.1 are known from PIV experiments. So both sides of Equation 2.1 should be integrated spatially to achieve the pressure field. One advantage here is that pressure is a scalar variable, so integration may be pursued in any direction. On the other hand, even if the integration is free from direction, number of integrations may introduce additional errors and averaging of the pressure output. Several researchers proposed different algorithms for definition of integration path. One of the simplest methods is proposed by Dabiri *et al.* [39] known as eight-path-integration. In this method, the pressure gradient is integrated along eight paths originating from corresponding boundary points at top, bottom, left, right, upper-left, upper-right, lower-left and lower-right towards the point of interest.

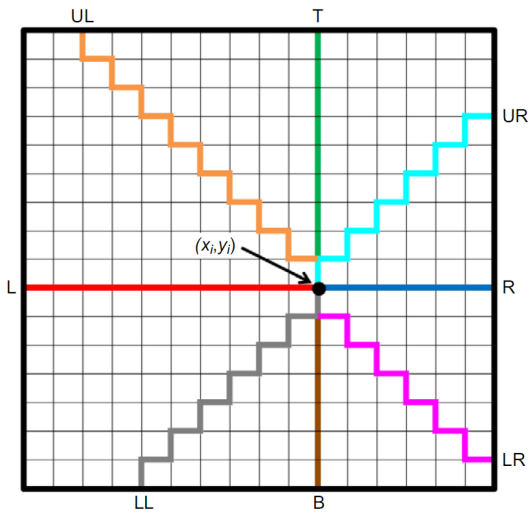

Figure 2.2: Eight-path integration method for inner point of interest (x_i, y_i) from [39].

Figure 2.2 shows eight integration paths for interior point (x_i, y_i). Later, Charonko *et al.* [17] showed that this method is highly sensitive to input data.

Liu and Katz [11, 41–43] offered and examined several omni-directional integration algorithms such as shortest path, real boundary originated and virtual boundary originated. From the proposed methods, virtual boundary omni-directional integration showed the most promising results except the location dependence due to denser distribution at regions closer to the starting point of integration. In this method, as shown on the left of Figure 2.3, integration starts from a point on the virtual boundary and passes through the real integration domain. The measurement points closer to the source point contributes more to final pressure estimation than further points which creates a non-uniform weighting. This non-uniform weighting problem could be observed for the top cells of the left grid in Figure 2.3 as a denser distribution of integration paths. The location dependence of integration is later removed by imposing a new algorithm so-called Parallel Ray Omni-Directional Integration method [40]. In this method, the point where integration paths are originated is located to infinity, which results as a set of parallel integration paths exhibiting equal contribution to the final pressure estimation. To achieve omni-directional paths, the parallel rays are rotated together with equal angles.

In most of the spatial integration studies, the flow-field is assumed to be far from the viscous regions. Thus, the viscous term on the right-hand side of the Equation 2.1

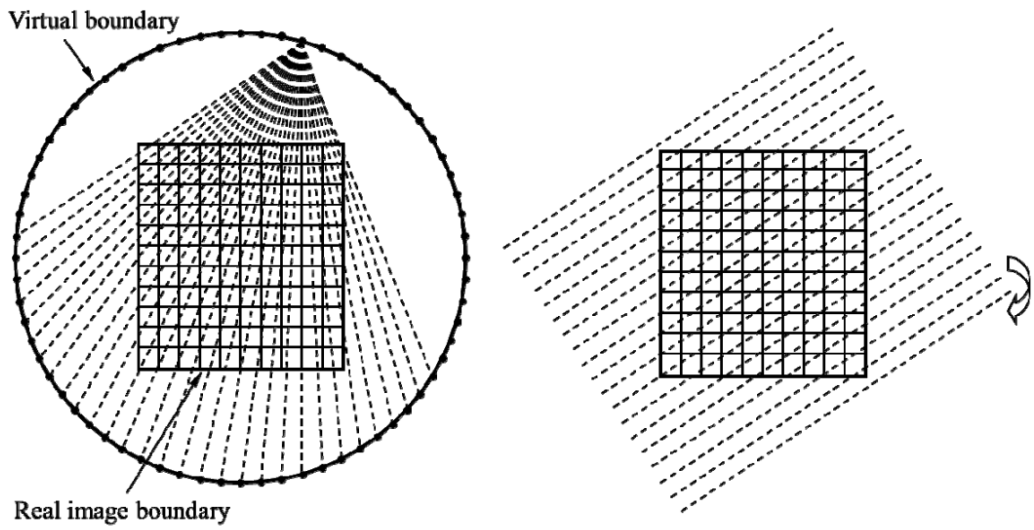

Figure 2.3: Virtual boundary (left) and rotating parallel ray (right) omni-directional integration algorithms [40].

would be negligible and excluding this term will lead to have the pressure gradient to be equal to material acceleration. In several independent studies, it is shown that the contribution of viscous terms on final pressure estimation would be two order of magnitude lower than the acceleration term for convective flows [41, 44, 45]. Even if this assumption strongly ease application of the method, sensitivity of solution to viscous contribution should be studied for specific cases.

2.2 Solution of Pressure Poisson Equation

Numerical solution of pressure Poisson equation is another common method for estimating pressure from PIV experiments. The PPE is derived by taking the divergence of the incompressible Navier-Stokes equation with constant viscosity. Taking divergence of both sides of Equation 2.1 gives

$$\nabla \cdot (\nabla p) = \nabla \cdot \left(-\rho \frac{\mathrm{D}\vec{V}}{\mathrm{D}t} + \mu \nabla^2 \vec{V} \right) \tag{2.4}$$

plugging the material acceleration definition in Equation 2.3 to 2.4 gives

$$\nabla^2 p = -\rho \frac{\partial}{\partial t}(\nabla \cdot \vec{V}) - \rho \nabla \cdot (\vec{V} \cdot \nabla)\vec{V} + \mu \nabla^2 (\nabla \cdot \vec{V}) \tag{2.5}$$

Recalling the divergence free nature of incompressible flows, $\nabla \cdot \vec{V} = 0$, gives three-dimensional pressure Poisson equation as follows:

$$\nabla^2 p = -\rho \nabla \cdot (\vec{V} \cdot \nabla)\vec{V} \tag{2.6}$$

For two-dimensional, incompressible flow pressure Poisson equation is given in Cartesian coordinates as

$$\frac{\partial^2 p}{\partial x^2} + \frac{\partial^2 p}{\partial y^2} = -\rho \left(\left(\frac{\partial u}{\partial x} \right)^2 + 2 \frac{\partial u}{\partial y} \frac{\partial v}{\partial x} + \left(\frac{\partial v}{\partial y} \right)^2 \right) \tag{2.7}$$

PPE could be discretized on two dimensional, equisized grids in the following form that is known as discrete pressure Poisson equation:

$$(\nabla^2 p)_{i,j} = \frac{1}{\Delta x^2}(p_{i+1,j} + p_{i-1,j} + p_{i,j-1} + p_{i,j+1} - 4p_{i,j}) = s_{i,j} \tag{2.8}$$

where the source term, $s_{i,j}$ is the right-hand side of Equation 2.7 and consists of all known parameters from PIV measurements. Using central difference gives the source term $s_{i,j}$ as follows:

$$s_{i,j} = -\rho \left(\left(\frac{u_{i+1,j} - u_{i-1,j}}{2\Delta x} \right)^2 + 2 \frac{u_{i,j+1} - u_{i,j-1}}{2\Delta x} \frac{v_{i+1,j} - v_{i-1,j}}{2\Delta x} + \left(\frac{v_{i,j+1} - v_{i,j-1}}{2\Delta x} \right)^2 \right) \tag{2.9}$$

Then, the problem becomes a set of linear algebraic equations and could be solved

with an iterative method. The final form of the pressure at any point is given as

$$p_{i,j} = \frac{1}{4}(p_{i+1,j} + p_{i-1,j} + p_{i,j-1} + p_{i,j+1} - \Delta x^2 s_{i,j}) \tag{2.10}$$

In Poisson formulation, both unsteady and viscous terms disappear, but this does not imply that the pressure could be estimated from instantaneous velocity fields only. The time-dependent information still needed at the boundary conditions, such as Neumann boundary conditions by imposing pressure gradient or Dirichlet boundary condition by imposing pressure itself [45]. The effects of the boundary condition types to the pressure estimation methodology is also extensively investigated and it is shown that Dirichlet boundary conditions result as more accurate final pressure estimations [46]. PPE is an elliptic type partial differential equation and any error in the solution field propagates omni-directionally. This arises the problem in declaring non-precise boundary conditions in the flow-field. Several routines and methods are applied to handle this sensitivity [18]. Auteri *et al.* proposed a procedure based on Glowinski and Pironneau method [47] to achieve exact integral conditions in the form of fully Dirichlet boundary conditions for uncoupled solution of incompressible Navier-Stokes equations [48].

2.3 Other Methods

The pressure field calculation from velocity field is a common practice in Computational Fluid Dynamics (CFD) studies. One of these attempts is performed by Hosokawa *et al.* [4] by imposing Solution Algorithm (SOLA) [49] to estimate pressure around a bubble. They examined three different forms of the algorithm and assessed the estimated pressure sensitivity to velocity field errors. In case of good quality velocity data, proposed method could give accurate results for laminar flows.

Okuno *et al.* [8] formulated image measurement process into a multi-objective problem. The image processing is identified as a dynamical system with constraints of governing equations. The problem is solved through employing evolution programming with the target of minimizing the residues aroused due to the imbalance in governing equations. Even if the main aim of the study is to enhance the velocity field

acquisition, this study is still stays as one of the earliest multidisciplinary attempts in pressure estimation from PIV data.

To the author's best knowledge, Jaw *et al.* [3] performed the only study that employs SIMPLER algorithm for pressure estimation from PIV measurements. They used the algorithm with finite analytic method for only steady flows with first order discretization schemes. The method promises great outcomes such as error correcting nature and does not demand any boundary condition implementation. It is believed that the rare use of finite analytic method and relatively brief introduction of the methodology have limited the use of SIMPLER algorithm for pressure estimation studies in available literature. SIMPLE family algorithms are one of the most commonly used algorithms in commercial and educational CFD codes. Detailed application, theory and programming fundamentals of the algorithm could be reached in any fundamental CFD book [50–53]. For solution of the flow-field we chose to implement finite volume method which is the original methodology used by Patankar for proposition of the algorithm [25]. Moreover, we improved pressure estimation method to handle also the transient flows. Special attention is paid to use higher order discretization schemes, which uses greater number of cells in computations to increase numerical accuracy. As a result current method could easily estimate pressure field satisfying governing equations and correct the experimental errors in the input velocity field. Further, the method could be used as an supplementary tool for quantifying the experimental uncertainty of the PIV systems which is a topic of great interest [54–61].

CHAPTER 3

NUMERICAL METHODOLOGY

The conservative form of the system of equations that governs unsteady, three-dimensional fluid flow and heat transfer of a compressible Newtonian fluid is given as follows:

continuity equation,

$$\frac{\partial \rho}{\partial t} + \nabla \cdot (\rho \vec{V}) = 0 \tag{3.1}$$

x-momentum equation,

$$\frac{\partial (\rho u)}{\partial t} + \nabla \cdot (\rho \vec{V} u) = -\frac{\partial p}{\partial x} + \nabla \cdot (\mu \nabla u) + S_u \tag{3.2}$$

y-momentum equation,

$$\frac{\partial (\rho v)}{\partial t} + \nabla \cdot (\rho \vec{V} v) = -\frac{\partial p}{\partial y} + \nabla \cdot (\mu \nabla v) + S_v \tag{3.3}$$

z-momentum equation,

$$\frac{\partial (\rho w)}{\partial t} + \nabla \cdot (\rho \vec{V} w) = -\frac{\partial p}{\partial z} + \nabla \cdot (\mu \nabla w) + S_w \tag{3.4}$$

Energy equation,

$$\frac{\partial (\rho i)}{\partial t} + \nabla \cdot (\rho \vec{V} i) = -p \nabla \cdot \vec{V} + \nabla \cdot (k \nabla T) + \Phi + S_i \tag{3.5}$$

where ρ, S, μ, k, Φ, $\vec{V}$ are density, source term, dynamic viscosity, thermal conductivity, dissipation function and velocity field, respectively. The structural commonalities between the conservation equations may benefit from forming a general type of equation for an ease of application of numerical schemes and interpretation of the physical role of the terms in those equations. Equation 3.6 is the resulting *transport equation* for the general variable ϕ:

$$\frac{\partial (\rho \phi)}{\partial t} + \nabla \cdot (\rho \vec{V} \phi) = \nabla \cdot (\Gamma \nabla \phi) + S_\phi \tag{3.6}$$

where Γ is defined to be the diffusion coefficient for the scalar property ϕ. The general transport equation emphasizes different transport processes of ϕ. The first term on the left hand side of the equation is the transient term and indicates the time rate of change of ϕ. The second term, convective term, denotes the net rate of flow out of the fluid element. The first term on the right hand side, diffusive term, denotes the rate of increase of ϕ due to diffusion in the flow-field. The last term is the source term and denotes the increase of the ϕ due to sources. For generalization, uncommon terms are hidden in the source term, such as the pressure gradient in the momentum equation. Setting the general variable ϕ to 1, u, v, w and i (or T). and selecting the appropriate values for source terms and the diffusion coefficient gives conservation of mass, momentum and energy, respectively.

PIV does not take temperature into account so hereafter we will omit the energy conservation in the methodology. On the other hand, even the methodology could be successfully applied to the three-dimensional flows, the application of the thesis will focus on two-dimensional, planar PIV measurements, so z-momentum is also out of interest for further sections. In this scope, the governing equations for two-dimensional, incompressible flow-fields with constant viscosity read:

continuity equation,

$$\frac{\partial}{\partial x}(\rho u) + \frac{\partial}{\partial y}(\rho v) = 0 \tag{3.7}$$

x-momentum equation,

$$\frac{\partial(\rho u)}{\partial t} + \frac{\partial}{\partial x}(\rho u u) + \frac{\partial}{\partial y}(\rho v u) = -\frac{\partial p}{\partial x} + \frac{\partial}{\partial x}\left(\mu \frac{\partial u}{\partial x}\right) + \frac{\partial}{\partial y}\left(\mu \frac{\partial u}{\partial y}\right) + S_u \tag{3.8}$$

y-momentum equation,

$$\frac{\partial(\rho v)}{\partial t} + \frac{\partial}{\partial x}(\rho u v) + \frac{\partial}{\partial y}(\rho v v) = -\frac{\partial p}{\partial y} + \frac{\partial}{\partial x}\left(\mu \frac{\partial v}{\partial x}\right) + \frac{\partial}{\partial y}\left(\mu \frac{\partial v}{\partial y}\right) + S_v \tag{3.9}$$

3.1 One-Dimensional Convection-Diffusion Problem

The methodology could be described on a steady, one-dimensional convection-diffusion problem in the absence of any source term. Transportation of the property ϕ with dif-

fusion and convection is governed by

$$\frac{d}{dx}(\rho u \phi) = \frac{d}{dx}\left(\Gamma \frac{d\phi}{dx}\right) \tag{3.10}$$

On top of it, flow should satisfy the continuity

$$\frac{d(\rho u)}{dx} = 0 \tag{3.11}$$

The control volume including center node P is bounded by faces w and e and has nodes W and E in the neighborhood. Lower case letters denote faces whereas the upper-case letters are showing the nodes where δ is the distance between the faces and nodes, faces and faces, etc.

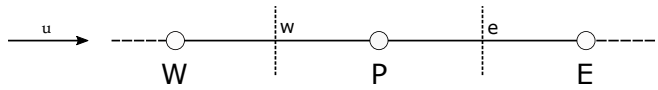

Figure 3.1: One dimensional control volume around point P

Integration of the transport equation (3.10) for the one-dimensional control volume around node P gives

$$(\rho u A \phi)_e - (\rho u A \phi)_w = \left(\Gamma A \frac{d\phi}{dx}\right)_e - \left(\Gamma A \frac{d\phi}{dx}\right)_w \tag{3.12}$$

Similarly, integration of the continuity equation (3.11) for the one-dimensional control volume around node P gives

$$(\rho u A)_e - (\rho u A)_w = 0 \tag{3.13}$$

The terms in equation 3.12 should be approximated for discretization of convection-diffusion problem. Here two new variables F and D could be defined as being the convective mass flux per unit area and diffusion conductance:

$$F \equiv \rho u \qquad\qquad D \equiv \frac{\Gamma}{\delta x} \tag{3.14}$$

The values of F and D at the cell faces are given as

$$F_w = (\rho u)_w \qquad\qquad F_e = (\rho u)_e \tag{3.15}$$

$$D_w = \frac{\Gamma_w}{\delta x_{_{WP}}} \qquad\qquad D_e = \frac{\Gamma_e}{\delta x_{_{PE}}} \tag{3.16}$$

where $\delta x_{_{WP}}$ defines the distance between centers of W and P cells in $x-$direction.

One may easily assume to have the same grid size along the x-direction (i.e. $A_w = A_e = A$) by considering that the PIV interrogation windows are being with the same size. So, the area in equations 3.12 and 3.13 could be eliminated from both sides. Then, the integrated transport equation (3.12) could be discretized via central differencing scheme with the new variables F and D as

$$F_e\phi_e - F_w\phi_w = D_e(\phi_E - \phi_P) - D_w(\phi_P - \phi_W) \tag{3.17}$$

After eliminating the area from the integrated continuity equation (3.13), it could be written as

$$F_e - F_w = 0 \tag{3.18}$$

Values of the transported property ϕ is stored at the nodes. To be able to solve the transport equation, face values of ϕ should be calculated. Different numerical schemes are employed to achieve this and a few of available schemes would be described in upcoming sections with their specific characteristics.

3.2 Discretization Schemes

3.2.1 Properties of Discretization Schemes

Any consistent discretization scheme to give physically realistic solution should satisfy three main requirements such as *conservativeness*, *transportiveness* and *boundedness*.

Conservativeness:

There should be consistent relation for the flux calculation across the control volume faces. The flux of ϕ leaving the control volume should be equal to the flux of ϕ entering the control volume through the same face. Conservativeness could be defined as flux consistency at the control volume faces.

Boundedness:

The discretized equations are set of algebraic equations and need to be solved by iterative methods. Scarborough [62] shows that a sufficient condition for a convergent iterative method in terms of coefficients of ϕ is

$$\frac{\Sigma|a_{nb}|}{|a_P^{'}|} \qquad \begin{cases} \leq 1 & \text{at all nodes} \\ < 1 & \text{at one node at least} \end{cases} \tag{3.19}$$

where $a_P^{'}$ is the net coefficient at the central node, i.e. $a_P^{'} = a_P - S_P$ and $\Sigma|a_{nb}|$ is the sum of all coefficients at the neighboring nodes. S_P is the linearized component of the source term that depends on ϕ_P.

Boundedness emphasizes that the interior values of ϕ in a control volume should be bounded by its boundary values in the absence of any source. Another important requirement for boundedness is that *all coefficients of the discretized equation should have the same sign.* This requirement results as having an increase in ϕ in any cell would lead an increase in ϕ at neighboring cells.

Transportiveness:

The discretization scheme should consider the physical phenomenon accurately to be able to give physically realistic solutions. In this scope, one may expect to have consistent behavior from the discretization scheme with varying strengths of two distinct transport mechanisms, i.e. convection and diffusion. To evaluate this, non-dimensional cell Peclet number, which is the ratio of relative strengths of convection to diffusion, could be defined as

$$Pe = \frac{F}{D} = \frac{\rho u}{\Gamma/\delta x} \tag{3.20}$$

where δx is the characteristic length - cell width for rectangular grids. If one specifically focuses on the momentum conservation, diffusion coefficient (Γ) would be the dynamic viscosity (μ) and the cell Peclet number will be identical to the cell Reynolds number given as

$$Pe_{\Delta} = \frac{F}{D} = \frac{\rho u}{\mu/\delta x} = \frac{\rho u \delta x}{\mu} = Re_{\Delta} \tag{3.21}$$

At this point, we may return to the one dimensional case. Let's consider the center node P is bounded by neighboring W and E cells and flow is from west to east. If there exists pure diffusion, the magnitude of general variable at west face ϕ_w would be influenced equally from west and center nodes and its value would be the average of ϕ_W and ϕ_P. On the contrary, with prevailing convection (increasing Pe), ϕ_w would converge to ϕ_W and there would be less contribution from the downstream cell, ϕ_P. So an ideal discretization scheme should take into account the flow direction to have a more realistic result.

3.2.2 Central Differencing Scheme

To estimate the cell face values of property ϕ, the first thing coming to mind would be the linear interpolation of the node values. For a uniform grid, the cell face values

could be approximated as the average of node values as

$$\phi_e = (\phi_P + \phi_E)/2 \tag{3.22a}$$

$$\phi_w = (\phi_W + \phi_P)/2 \tag{3.22b}$$

Substituting the cell face values to the discretized transport equation (3.17) gives

$$\frac{F_e}{2}(\phi_P + \phi_E) - \frac{F_w}{2}(\phi_W + \phi_P) = D_e(\phi_E - \phi_P) - D_e(\phi_P - \phi_W) \tag{3.23}$$

Rearranging equation 3.23 to collect all coefficients of node values gives

$$\begin{aligned}\left[\left(D_w + \frac{F_w}{2}\right) + \left(D_e - \frac{F_e}{2}\right) + (F_e - F_w)\right]\phi_P = \\ \left(D_w + \frac{F_w}{2}\right)\phi_W + \left(D_w - \frac{F_w}{2}\right)\phi_E\end{aligned} \tag{3.24}$$

Denoting the coefficients of node values with new symbol, a, will give the general form for discretization equation 3.24 as

$$a_P\phi_P = a_W\phi_W + a_E\phi_E \tag{3.25}$$

where center coefficient is given by

$$a_P = a_W + a_E + (F_e - F_w) \tag{3.26}$$

and neighbor coefficients are given by

$$\begin{aligned}a_E &= \left(D_e - \frac{F_e}{2}\right) \\ a_W &= \left(D_w + \frac{F_w}{2}\right)\end{aligned} \tag{3.27}$$

Before going further, central differencing scheme should be evaluated in terms of the properties of a successful discretization scheme. The central differencing scheme uses

consistent formulations for convective and diffusive flux calculations, thus scheme possesses conservativeness. In terms of boundedness, one-dimensional continuity equation (3.18) dictates $a_P = a_W + a_E$, which proves that central differencing scheme also satisfies the Scarborough criteria. Moreover, for boundedness, the scheme should also meet another requirement that is having all coefficients with the same sign, usually positive. By definition, the diffusive conductance, D, is positive all the time, but in case of one-dimensional unidirectional flow from west to east, a_E may be negative for values of $F_e > 2D_e$ which will give the following requirement for boundedness of central differencing scheme:

$$Pe = F/D < 2 \tag{3.28}$$

For central differencing schemes, $Pe < 2$ is the condition to have all positive coefficients. If there are cells with $Pe > 2$ in the flow-field, solution will not be bounded. There will be extremities in the flow-field those seen as wiggles at those cells.

In central differencing scheme, faces are affected from the convective and diffusive flux of neighboring cells equally. The flow direction is not recognized in central differencing scheme which emphasizes that the scheme does not possess transportiveness property. This would be specially problematic at high Reynolds number flows in which convection dominates and limits the use of central differencing scheme for low Reynolds number flows.

3.2.3 Upwind Differencing Scheme

The lack of transportiveness property of central differencing scheme limits the use for low Re flows. The most basic method for taking the flow direction into account would be approximating the value of ϕ on the face to be equal to the value of the ϕ on upstream node. On the same, one-directional flow from west to east, the value of ϕ at the west face would be equal to the value of ϕ at west cell ($\phi_w = \phi_W$). Similarly, the value of ϕ at the east face of the center node would be equal to the value of ϕ at

center node ($\phi_e = \phi_P$). Then the discretized transport equation (3.17) becomes

$$F_e\phi_P - F_w\phi_W = D_e(\phi_E - \phi_P) - D_w(\phi_P - \phi_W) \tag{3.29}$$

Collecting the coefficients of ϕ values together gives

$$(D_w + D_e + F_e)\phi_P = (D_w + F_w)\phi_W + D_e\phi_E \tag{3.30}$$

which could be rearranged as

$$[(D_w + F_w) + D_e + (F_e - F_w)]\phi_P = (D_w + F_w)\phi_W + D_e\phi_E \tag{3.31}$$

Defining the coefficients of ϕ_P, ϕ_W and ϕ_E as a_P, a_W and a_E, respectively, lets us to write equation 3.31 in the following general form

$$a_P\phi_P = a_W\phi_W + a_E\phi_E \tag{3.32}$$

where the center coefficient, similar with central differencing, is

$$a_P = a_W + a_E + (F_e - F_w) \tag{3.33}$$

but neighbor coefficients are becoming

$$\begin{aligned} a_E &= D_e \\ a_W &= D_w + F_w \end{aligned} \tag{3.34}$$

Unlike the central differencing scheme, in upwind differencing scheme flow direction alters the neighbor coefficient definitions. In the same way as positive direction, one may show that the coefficients for east-to-west flows, $u_e < 0$, $u_w < 0$ ($F_w < 0$,

$F_e < 0$) are

$$\begin{aligned} a_E &= D_e - F_e \\ a_W &= D_w \end{aligned} \tag{3.35}$$

A general form for neighbor coefficients of upwind differencing scheme for one-dimensional problem could be achieved by combining equations 3.34 and 3.35 as

$$\begin{aligned} a_E &= D_e + \max(0, -F_e) \\ a_W &= D_w + \max(F_w, 0) \end{aligned} \tag{3.36}$$

The upwind differencing scheme for the one-dimensional convection-diffusion problem is given by equation 3.32 in general form, the central coefficient (a_P) is given by equation 3.33, where the neighbor coefficients (a_W and a_E) are given by equation 3.36.

The upwind differencing scheme implements upstream node values, so the terms for face flux calculations possess consistent operations which emphasizes the transportiveness of the scheme. The coefficients are always positive which proves that the scheme is unconditionally bounded. Moreover, the method is based on taking the flow direction into account so it inherently has transportiveness.

3.2.4 Hybrid Differencing Scheme

Hybrid differencing scheme of Spalding [63] gets the best of both upwind and central differencing schemes. The central differencing scheme has second order accuracy but lacks of transportiveness for $Pe > 2$ and upwind differencing scheme possesses unconditionally transportiveness but it is limited to be first order accurate. Thus, for $Pe < 2$ range the method employs central differencing scheme and when convection starts to dominate ($Pe > 2$) the method ignores the diffusion contribution and switches to upwind differencing scheme.

For the one-dimensional convection-diffusion problem, the discretized equation (3.25) and center coefficient definitions (3.26) are same with central and upwind differenc-

ing schemes. The only different parameters are the neighbor coefficients which are given by

$$
\begin{aligned}
a_E &= \max\left[-F_e, \left(D_e - \frac{F_e}{2}\right), 0\right] \\
a_W &= \max\left[F_w, \left(D_w + \frac{F_w}{2}\right), 0\right]
\end{aligned}
\tag{3.37}
$$

The hybrid differencing scheme has all the properties of central differencing scheme as conservativeness, boundedness and transportiveness at the range of $Pe < 2$. For dominating convection, Pe exceeds 2 and central differencing scheme lacks transportiveness. In this case, the scheme switches to upwind differencing scheme and still employs transportiveness for the higher values of Pe.

3.2.5 Power-law Scheme

The deviation of hybrid scheme from one-dimensional exact solution just after $Pe > 2$ is modified by power-law scheme via fifth order polynomial, if $Pe > 10$ [50]. Keeping the discretized equation (3.25) and center coefficient definitions (3.26) same with aforementioned schemes; the neighbor coefficients for power-law scheme of one-dimensional convection-diffusion problem given as follows:

$$
\begin{aligned}
a_E &= D_e \max\left[0, (1 - 0.1|Pe_e|)^5\right] + \max\left[F_e, 0\right] \\
a_W &= D_w \max\left[0, (1 - 0.1|Pe_w|)^5\right] + \max\left[F_w, 0\right]
\end{aligned}
\tag{3.38}
$$

3.2.6 Exponential Scheme

The one-dimensional convection-diffusion problem given by equation 3.10 could be solved exactly for the domain $0 \leq x \leq L$ by assuming constant Γ. Recalling that ρu is constant from the continuity equation (3.11) with given boundary conditions

$$
\begin{aligned}
\phi &= \phi_{\mathrm{o}} \qquad \text{for} \qquad x = 0 \\
\phi &= \phi_L \qquad \text{for} \qquad x = L
\end{aligned}
\tag{3.39}
$$

the solution of equation 3.10 is

$$\frac{\phi - \phi_{\mathrm{o}}}{\phi_L - \phi_{\mathrm{o}}} = \frac{\exp\left(Pe\, x/L\right) - 1}{\exp\left(Pe\right) - 1} \tag{3.40}$$

The exact solution is plotted for different values of Peclet number in Figure 3.2. It is seen that in the zero limit of Pe, only diffusion exists and the ϕ vs. x variation should follow a linear trend. In positive flow direction (flow from $x = 0$ to $x = L$), increasing Pe points out the dominance of convection and as a result of this along most of the domain ϕ gets close to the upstream value of ϕ_{o}. In case of negative flow direction (flow from $x = L$ to $x = 0$), ϕ_L would be the upstream value and stronger convection results as covering most of the domain with ϕ_L.

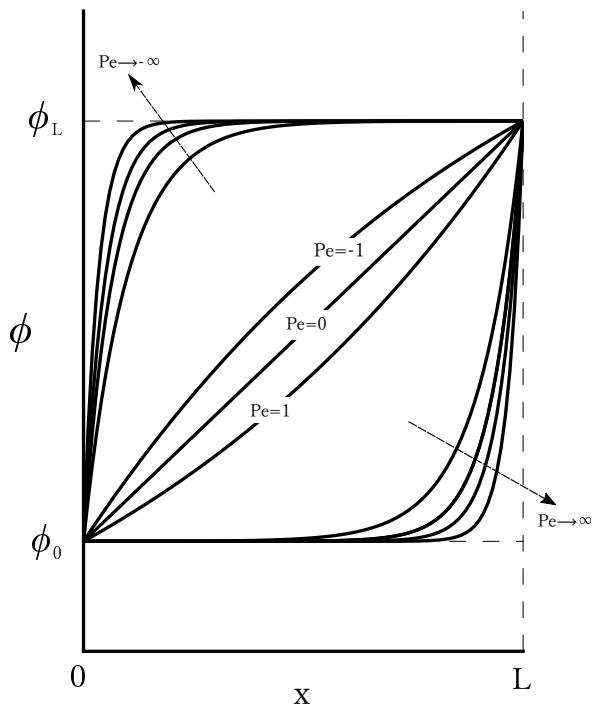

Figure 3.2: Exact solution of one-dimensional convection-diffusion problem for different Pe

Arranging the exact solution to be a suitable scheme for the one-dimensional convection-diffusion problem gives the exponential scheme The discretized equation (3.25) and center coefficient definitions (3.26) of exponential scheme are same with aforemen-

tioned schemes. The neighbor coefficients for exponential scheme are given by

$$
\begin{aligned}
a_E &= \frac{F_e}{\exp\left(F_e/D_e\right) - 1} \\
a_W &= \frac{F_w \exp\left(F_w/D_w\right)}{\exp\left(F_w/D_w\right) - 1}
\end{aligned}
\tag{3.41}
$$

This scheme gives exact solution for steady one-dimensional convection-diffusion problems for all Peclet numbers. On the other hand, the exponential scheme is not exact for two- or three-dimensional problems and involves exponentials which are computationally expensive. So, it is not commonly preferred for numerical studies.

3.2.7 Quadratic Upstream Interpolation for Convective Kinetics (QUICK) Scheme

The upwind, hybrid and power-law schemes has first order accuracy, but unlike the second order accurate central differencing scheme, they possess transportiveness and are stable at all ranges. The best choice is to have a stable scheme which has also higher accuracy. These favorable characteristics of upwind scheme leads to develop higher-order upwind schemes for stability and sensitivity to the flow direction by overcoming the low accuracy deficit. First of that kind of attempts is achieved by Leonard [64] with quadratic upstream interpolation for convective kinetics (QUICK) scheme.

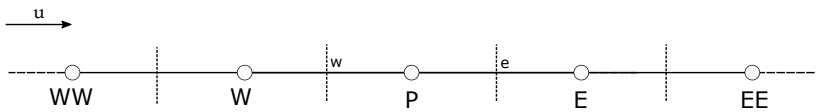

Figure 3.3: Grid points for calculation of QUICK scheme coefficients for one-dimensional flow

The QUICK scheme uses three-point upstream-weighted quadratic interpolation for calculation of the cell face values. On any face, the neighboring two node values and an extra upstream value is used for interpolation. The face value of ϕ, that is located

between nodes i and $i-1$, on a uniform grid is given as

$$\phi_{face} = \frac{6}{8}\phi_{i-1} + \frac{3}{8}\phi_i - \frac{1}{8}\phi_{i-2} \tag{3.42}$$

The one-dimensional convection-diffusion problem could be redrawn as in Figure 3.3 for the QUICK scheme by taking into account the further upstream nodes for positive and negative flow directions as WW and EE. For positive flow direction, ($F_w > 0$ and $F_e > 0$), variables at the face are given as

$$\begin{aligned} \phi_w =& \frac{6}{8}\phi_W + \frac{3}{8}\phi_P - \frac{1}{8}\phi_{WW} \\ \phi_e =& \frac{6}{8}\phi_P + \frac{3}{8}\phi_E - \frac{1}{8}\phi_W \end{aligned} \tag{3.43}$$

Plugging the above values to the one-dimensional convection-diffusion equation gives

$$\begin{aligned} \left[F_e\left(\frac{6}{8}\phi_P + \frac{3}{8}\phi_E - \frac{1}{8}\phi_W\right) - F_w\left(\frac{6}{8}\phi_W + \frac{3}{8}\phi_P - \frac{1}{8}\phi_{WW}\right)\right] = \\ D_e\left(\phi_E - \phi_P\right) + D_w\left(\phi_P - \phi_W\right) \end{aligned} \tag{3.44}$$

Collecting all the variables of node values gives

$$\begin{aligned} \left[D_w - \frac{3}{8}F_w + D_e + \frac{6}{8}F_e\right]\phi_P = \left[D_w + \frac{6}{8}F_w + \frac{1}{8}F_e\right]\phi_W \\ + \left[D_e - \frac{3}{8}F_e\right]\phi_E + \frac{1}{8}F_w\phi_{WW} \end{aligned} \tag{3.45}$$

Equation 3.45 could be written in the general form as

$$a_P\phi_P = a_W\phi_W + a_E\phi_E + a_{WW}\phi_{WW} \tag{3.46}$$

where the coefficients are

$$
\begin{aligned}
a_W &= D_w + \frac{6}{8}F_w + \frac{1}{8}F_e \\
a_E &= D_e - \frac{3}{8}F_e \\
a_{WW} &= \frac{1}{8}F_w \\
a_P &= a_W + a_E + a_{WW} + (F_e - F_w)
\end{aligned}
\tag{3.47}
$$

For flow in negative direction ($F_w < 0$ and $F_e < 0$), the face values can be written as

$$
\begin{aligned}
\phi_w =& \frac{6}{8}\phi_P + \frac{3}{8}\phi_W - \frac{1}{8}\phi_E \\
\phi_e =& \frac{6}{8}\phi_E + \frac{3}{8}\phi_P - \frac{1}{8}\phi_{EE}
\end{aligned}
\tag{3.48}
$$

The general form of discretized equation for negative flow direction would be

$$
a_P\phi_P = a_W\phi_W + a_E\phi_E + a_{EE}\phi_{EE} \tag{3.49}
$$

where the coefficients are

$$
\begin{aligned}
a_W &= D_w + \frac{3}{8}F_w \\
a_E &= D_e - \frac{6}{8}F_e - \frac{1}{8}F_w \\
a_{EE} &= \frac{1}{8}F_e \\
a_P &= a_W + a_E + a_{EE} + (F_e - F_w)
\end{aligned}
\tag{3.50}
$$

As done in other schemes, one can combine the discretized equations (3.46 and 3.50) for both flow directions in the following general form

$$
a_P\phi_P = a_W\phi_W + a_E\phi_E + a_{EE}\phi_{EE} + a_{WW}\phi_{WW} \tag{3.51}
$$

with central coefficient being

$$a_P = a_W + a_E + a_{WW} + a_{EE} + (F_e - F_w) \tag{3.52}$$

and neighbor coefficients are

$$\begin{aligned}
a_W &= D_w + \frac{6}{8}\max(F_w, 0) + \frac{1}{8}\max(F_e, 0) - \frac{3}{8}\max(-F_w, 0) \\
a_E &= D_e - \frac{3}{8}\max(F_e, 0) + \frac{6}{8}\max(-F_e, 0) + \frac{1}{8}\max(-F_w, 0) \\
a_{WW} &= -\frac{1}{8}\max(F_w, 0) \\
a_{EE} &= -\frac{1}{8}\max(-F_e, 0)
\end{aligned} \tag{3.53}$$

The QUICK scheme uses the given quadratic expressions for face values, thus the scheme is conservative. Use of two upstream and one downstream node for face value calculations leads the scheme to possess the transportiveness property inherently.

Any scheme should satisfy two requirements to give a bounded result. First requirement is to have central coefficient larger or equal to the sum of all neighboring node coefficients and this is achieved when flow satisfies continuity. The second requirement, which is the main handicap of QUICK scheme, states that all coefficients of the discretized equation should be with the same sign -positive for present notation. For positive flow direction, the east coefficient that is defined by equation 3.47 could be negative for ordinary Peclet numbers ($Pe_e = F_e/D_e > 8/3$). Same issue is seen on west coefficient, if the flow is in negative direction. Thus, the original QUICK scheme is conditionally stable and needs treatments/improvements.

After the introducing of the QUICK scheme, several studies proposed improvements on the lack of general boundedness and on the accuracy [13, 65–68]. The final well-accepted form of QUICK scheme is offered by Hayase *et al.* [69] in which the negative coefficients are incorporated into the source terms to achieve a stable scheme. In this method, the face values for positive flow direction, which is given by equation

3.43 originally, is rearranged in the following form

$$\begin{aligned} \phi_w = &\quad \phi_W + \frac{1}{8}\left(3\phi_P - 2\phi_W - \phi_{WW}\right) \qquad \text{for} \quad F_w > 0 \\ \phi_e = &\quad \phi_P + \frac{1}{8}\left(3\phi_E - 2\phi_P - \phi_W\right) \qquad \text{for} \quad F_e > 0 \end{aligned} \tag{3.54}$$

For negative flow direction, the face values given by equation 3.48 are rearranged as

$$\begin{aligned} \phi_w = &\quad \phi_W + \frac{1}{8}\left(3\phi_W - 2\phi_P - \phi_E\right) \qquad \text{for} \quad F_w < 0 \\ \phi_e = &\quad \phi_P + \frac{1}{8}\left(3\phi_P - 2\phi_E - \phi_{EE}\right) \qquad \text{for} \quad F_e < 0 \end{aligned} \tag{3.55}$$

The reason of rearranging the face value definitions is to put the terms which may lead to negative coefficients into the deferred correction source (DCS) term to have all-time positive coefficients. Then, the general discretization equation for one-dimensional steady state problem becomes

$$a_P\phi_P = a_W\phi_W + a_E\phi_E + S^{DC} \tag{3.56}$$

where the corresponding coefficients are

$$\begin{aligned} a_W &= D_w + \max\left(F_w, 0\right) \\ a_E &= D_e + \max\left(0, -F_e\right) \\ a_P &= a_W + a_E + \left(F_e - F_w\right) \end{aligned} \tag{3.57}$$

and the DCS term is

$$
\begin{aligned}
S^{DC} = & \frac{1}{8}\left(3\phi_P - 2\phi_W - \phi_{WW}\right)\max\left(F_w, 0\right) + \\
& \frac{1}{8}\left(\phi_W + 2\phi_P - 3\phi_E\right)\max\left(F_e, 0\right) - \\
& \frac{1}{8}\left(3\phi_W - 2\phi_P - \phi_E\right)\max\left(-F_w, 0\right) - \\
& \frac{1}{8}\left(2\phi_E + \phi_{EE} - 3\phi_P\right)\max\left(-F_e, 0\right)
\end{aligned}
\tag{3.58}
$$

Finally, with this form of QUICK scheme, the main coefficients (a_W and a_E) are always positive regardless of the Peclet number. All terms with the possibility of generating negative coefficients are included in the deferred correction source term. Thus, the scheme possesses conservativeness, boundedness and transportiveness unconditionally. The DCS term is calculated by the node values in the previous iteration, so correction is deferred by one iteration. Even the QUICK scheme is stable, highly accurate method; it may show some over-shoots and under-shoots at steep gradients [51].

3.2.8 Total Variation Diminishing Schemes

As seen on Table 3.1, the upwind scheme is the most stable and consistent formulation but lacks of numerical diffusion due to the lower accuracy. All other schemes have certain pitfalls from different aspects. The most suitable scheme stands as QUICK scheme, if the oscillatory behavior at steep gradients is somehow removed. Due to this, several attempts are tried at 70s and 80s for developing a consistent non-oscillatory, shock capturing scheme. Even the studies are originally focusing on developing a successful scheme for handling unsteady gas dynamics problems, today they could also be used for solving incompressible problems as well. The special family of schemes available for this purpose is called as Total Variation Diminishing (TVD) schemes.

The general idea on TVD schemes is to add an artificial diffusion or a weighting regarding to the upstream contribution. Previously discussed schemes could be rewrit-

Table 3.1: Comparison of discretization schemes

	Boundedness	Transportiveness	Conservativeness	Accuracy
Upwind Diff.[a]	Yes	Yes	Yes	First
Central Diff.	for $Pe < 2$	No	Yes	Second
Hybrid Diff.	Yes	Yes	Yes	Second[b]
Exponential[c]	Yes	Yes	Yes	First
Power-law	Yes	Yes	Yes	First
QUICK[d] [64]	for $Pe < 8/3$	Yes	Yes	Third[e]
QUICK+[d] [69]	Yes	Yes	Yes	Third[e]

[a] highly stable but may produce false numerical diffusion if flow is not aligned with grid lines
[b] scheme is first order for $Pe > 2$
[c] exact for one-dimensional flows but not for two- and three-dimensions
[d] scheme may generate wiggles at abrupt variations/steep gradients
[e] third order accurate on a uniform grid, second order on non-uniform grid

ten around the face of a one-dimensional node in a certain form which will encourage one to generalize the schemes by means of a weighting parameter. The definition of the weighting parameter will be given after rearranging the aforementioned schemes in a general form.

If one assumes to have a flow in positive direction, then the standard upwind differencing around the face is given by

$$\phi_f = \phi_U \tag{3.59}$$

where subscript f denotes the face and U denotes the upwind node value. In further formulations, D refers to downstream and UU to upstream of U.

The accuracy of original upwind differencing scheme could be improved by implementing one extra upstream node into discretization (UU). This scheme is generally referred as *linear upwind differencing scheme* or as *second order upwind differencing*

scheme (LUD). The face value for the linear upwind differencing scheme is given as

$$\begin{aligned}\phi_f &= \phi_U + \frac{(\phi_U - \phi_{UU})}{\delta x}\frac{\delta x}{2} \\ &= \phi_U + \frac{1}{2}(\phi_U - \phi_{UU})\end{aligned} \tag{3.60}$$

and could be arranged in the following form for generalization

$$\phi_f = \phi_U + \frac{1}{2}\left(\frac{\phi_U - \phi_{UU}}{\phi_D - \phi_U}\right)(\phi_D - \phi_U) \tag{3.61}$$

The central differencing scheme around the face is given as

$$\phi_f = \phi_U + \frac{1}{2}(\phi_D - \phi_U) \tag{3.62}$$

The QUICK scheme for the same face is given by equation 3.43 and could be rearranged in the following form

$$\phi_f = \phi_U + \frac{1}{2}\left[\frac{1}{4}\left(3 + \frac{\phi_U - \phi_{UU}}{\phi_D - \phi_U}\right)\right](\phi_D - \phi_U) \tag{3.63}$$

The equations 3.59, 3.61, 3.62 and 3.63 are all in a general form given as

$$\phi_f = \phi_U + \frac{1}{2}\varphi(\phi_D - \phi_U) \tag{3.64}$$

where φ is defined to be the weighting factor by Sweby [70] which is the basis of TVD schemes. It could be seen that all above equations have the following expression is common

$$r = \frac{\phi_U - \phi_{UU}}{\phi_D - \phi_U} \tag{3.65}$$

which is the ratio of upstream gradient to the downstream gradient. The weighting parameters would be defined by the use of independent variable r and tabulated in

Table 3.2 for four schemes discussed.

Table 3.2: Weighting factors for UD, LUD, CD and QUICK schemes

	$\varphi(r)$
UD	0
CD	1
LUD	r
QUICK	$(3+r)/4$

Harten [71] introduced the total variation concept for a discrete case as

$$TV = \sum_j \mid \phi_{j+1} - \phi_j \mid \tag{3.66}$$

If the total variation of the scheme is diminishing with progressing time-steps, then the scheme is *total variation diminishing* which is given as

$$TV(\phi^{n+1}) \leq TV(\phi^n) \tag{3.67}$$

The total variation concept is originally studied in gas dynamics to capture shocks without any oscillations for time-dependent flows, but it could also be used accurately for steady cases if one considers the time as progressing iteration number. Harten [71] stated that any TVD scheme is monotonicity-preserving and has following properties

i. no new local extrema is created
ii. the value of an existing local minima is non-decreasing and a local maximum is non-increasing

Godunov's theorem [72] proves that only first order linear schemes preserve monotonicity. Higher order linear schemes are not TVD and may introduce unphysical oscillations, such as negative turbulent kinetic energy, pressure, density or temperature. Thus, to achieve high resolution TVD schemes non-linearity should be addressed.

The upcoming sections will summarize a short version of the efforts put in to obtain high-resolution, non-linear TVD schemes through flux limiters.

Sweby [70] stated that any scheme should satisfy the following conditions on flux limiters to be TVD,

i. $\varphi(r) \leq 2r$ for $0 < r < 1$
ii. $\varphi(r) \leq 2$ for $r \geq 1$

For any scheme to be TVD, the limiter function must lie in the shaded region of Figure 3.4. It could stated that except the UD scheme, none of the aforementioned schemes are unconditionally TVD - for all values of r.

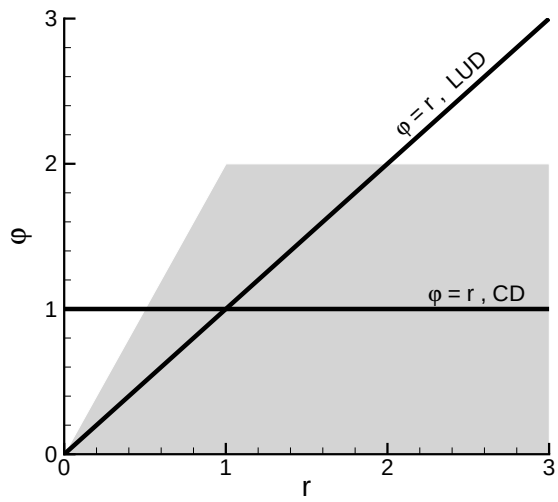

Figure 3.4: TVD region for discretization schemes

Linear upwind differencing and central differencing schemes are introduced by Warming and Beam [73] and Lax-Wendroff [74], respectively. Sweby [70] stated that any second order TVD scheme should pass through the point $\varphi(1) = 1$ and be a combination of Warming and Beam upwind scheme (LUD) and Lax-Wendroff scheme (CD). Defining $\theta(r)$ to be any function bounded in [0,1] range, Sweby's statement could be formulated as

$$\varphi(r) = (1 - \theta(r))\varphi^{CD}(r) + \theta(r)\varphi^{LUD}(r) \tag{3.68}$$

Recalling $\varphi^{CD}(r) = 1$ and $\varphi^{LUD}(r) = r$ reduces equation 3.68 to

$$\varphi(r) = 1 + \theta(r)(r - 1) \tag{3.69}$$

which satisfies the $\varphi(1) = 1$ constraint automatically and gives the second-order TVD region as shown in Fig. 3.5.

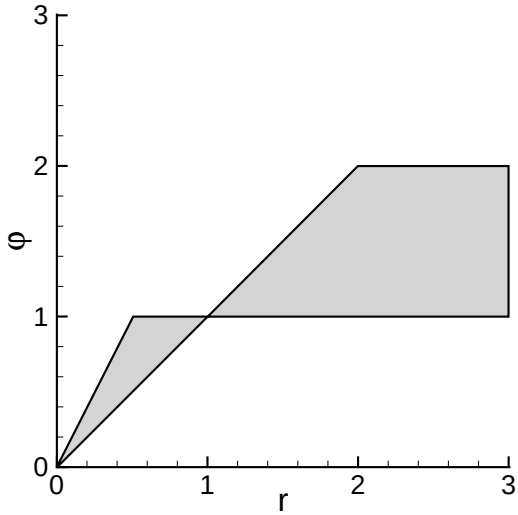

Figure 3.5: Second order TVD region

For any scheme to be second-order accurate TVD scheme, its corresponding limiter function should lie in the given shaded area.

Sweby [70] also states that all limiter functions discussed here are monotone increasing functions and have a symmetry of

$$\frac{\varphi(r)}{r} = \varphi(1/r) \tag{3.70}$$

which ensures that backward and forward facing gradients are treated similarly. A few of those symmetric, second-order TVD schemes from available literature are given in Table 3.3 and plotted on the second-order TVD region in Figure 3.6.

After defining the flux limiters, we may exemplify the implementation of TVD schemes on the aforementioned one-dimensional convection-diffusion problem. Recalling the

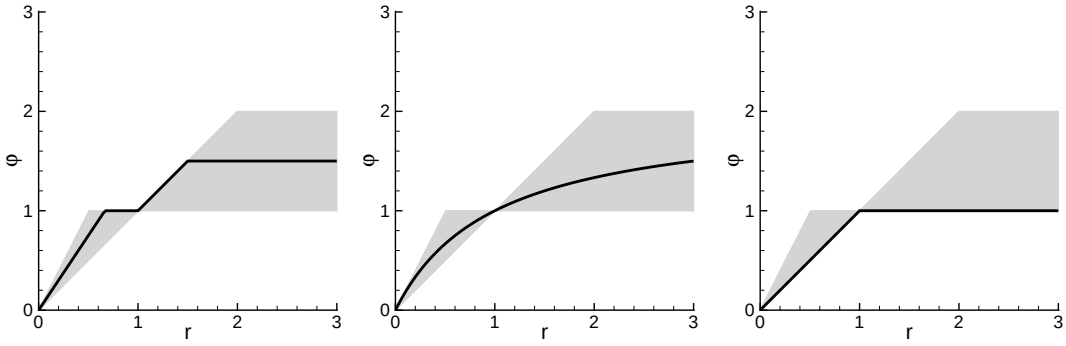

(a) Sweby ($\beta = 1.5$)

(b) van Leer

(c) Min-mod

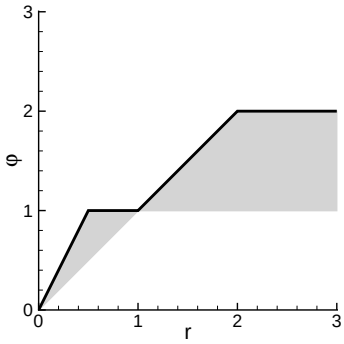

(d) SUPERBEE

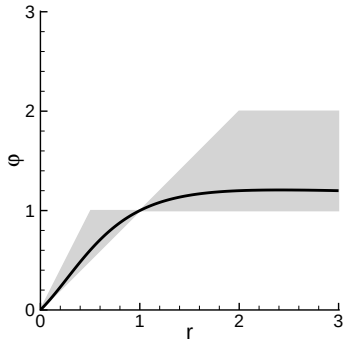

(e) van Albada

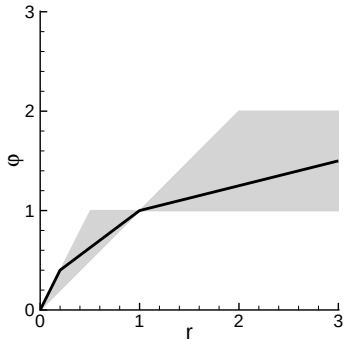

(f) UMIST

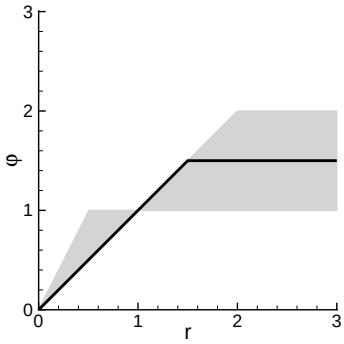

(g) Osher ($\beta = 1.5$)

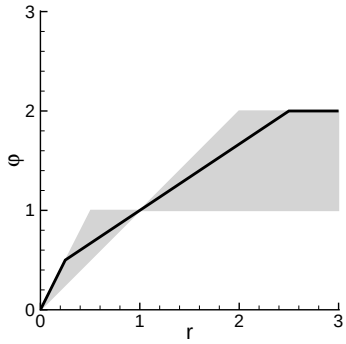

(h) Koren

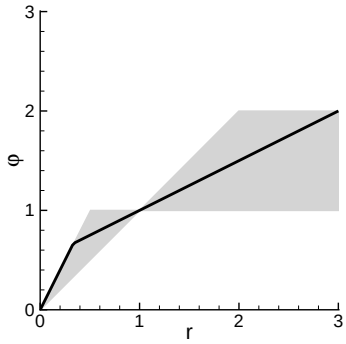

(i) Monotonized Central

Figure 3.6: Selected limiter functions for symmetric, second-order TVD schemes

Table 3.3: Selected flux limiters for symmetric, second-order TVD schemes

	$\varphi(r)$	$\lim_{r\to\infty} \varphi(r)$	Ref.
Sweby	$\max[0, \min(\beta r, 1), \min(r, \beta)]^*$	β	[70]
van Leer	$\dfrac{r + \lvert r \rvert}{1 + r}$	2	[75]
Min-Mod	$\max[0, \min(r, 1)]$	1	[76]
SUPERBEE	$\max[0, \min(2r, 1), \min(r, 2)]$	2	[76]
van Albada	$\dfrac{r + r^2}{1 + r^2}$	1	[77]
UMIST	$\max[0, \min(2r, (3r + 1)/4, (r + 3)/4, 2)]$	2	[78]
Osher	$\max[0, \min(r, \beta)]^*$	β	[79]
Koren	$\max[0, \min(2r, (2r + 1)/3, 2]$	2	[80]
Monotonized Central	$\max[0, \min(2r, (2r + 1)/2, 2]$	2	[81]

$^*1 \leq \beta \leq 2$

discretized form of one-dimensional convection-diffusion problem (Eq. 3.17) reads

$$F_e\phi_e - F_w\phi_w = D_e(\phi_E - \phi_P) - D_w(\phi_P - \phi_W) \tag{3.71}$$

Generalized form of face values is given by equation. 3.64 and the parameter r is defined by equation. 3.65. Plugging the appropriate values for positive x-direction flow gives east and west face values as

$$\begin{aligned} \phi_e &= \phi_P + \frac{1}{2}\varphi(r_e)\left(\phi_E - \phi_P\right) \\ \phi_w &= \phi_W + \frac{1}{2}\varphi(r_w)\left(\phi_P - \phi_W\right) \end{aligned} \tag{3.72}$$

$$r_e = \frac{\phi_P - \phi_W}{\phi_E - \phi_P} \qquad r_w = \frac{\phi_W - \phi_{WW}}{\phi_P - \phi_W} \tag{3.73}$$

where r_e and r_w are the ratios of upstream gradient to downstream gradient at east and west faces. Substituting equation 3.72 into equation 3.71 and rearranging gives

$$\begin{aligned}(D_e + F_e + D_w)\phi_P = &\ (D_w + F_w)\phi_W + D_e\phi_E \\ &- F_e\left[\frac{1}{2}\varphi(r_e)(\phi_E - \phi_P)\right] + F_e\left[\frac{1}{2}\varphi(r_e)(\phi_E - \phi_P)\right]\end{aligned} \tag{3.74}$$

Finally, it could be written in general form as

$$a_P\phi_P = a_W\phi_W + a_E\phi_E + S^{DC} \tag{3.75}$$

where the corresponding coefficients are

$$a_W = D_w + F_w \tag{3.76a}$$

$$a_E = D_e \tag{3.76b}$$

$$a_P = a_W + a_E + (F_e - F_w) \tag{3.76c}$$

and the DC source term is

$$S^{DC} = -F_e\left[\frac{1}{2}\varphi(r_e)(\phi_E - \phi_P)\right] + F_w\left[\frac{1}{2}\varphi(r_w)(\phi_P - \phi_W)\right] \tag{3.77}$$

Same practice could be followed for negative x-direction flow. However, since the downstream and upstream directions are reverse, face values and r definitions would be different as follows:

$$\begin{aligned}\phi_e &= \phi_P + \frac{1}{2}\varphi(r_e^-)\,(\phi_P - \phi_E) \\ \phi_w &= \phi_W + \frac{1}{2}\varphi(r_w^-)\,(\phi_W - \phi_P)\end{aligned} \tag{3.78}$$

$$r_e^- = \frac{\phi_{EE} - \phi_E}{\phi_E - \phi_P} \qquad r_w^- = \frac{\phi_E - \phi_P}{\phi_P - \phi_W} \tag{3.79}$$

To distinguish the different r definitions with varying flow-direction, the superscripts of $+$ and $-$ would be implemented for positive and negative flow directions, respectively. For negative x-direction flow, the general form of the one-dimensional convection-diffusion problem is same with equation 3.75. However, coefficients and deferred correction source term differ as noted below:

$$a_W = D_w \tag{3.80a}$$

$$a_E = D_e - F_e \tag{3.80b}$$

$$a_P = a_W + a_E + (F_e - F_w) \tag{3.80c}$$

and

$$S^{DC} = F_e \left[\frac{1}{2}\varphi(r_e^-)(\phi_E - \phi_P)\right] - F_w \left[\frac{1}{2}\varphi(r_w^-)(\phi_P - \phi_W)\right] \tag{3.81}$$

The flow direction may alter in the flow-field so one needs to combine the above expressions in one final form given as

$$a_P\phi_P = a_W\phi_W + a_E\phi_E + S^{DC} \tag{3.82}$$

where the corresponding coefficients are

$$a_W = D_w + \max(F_w, 0) \tag{3.83a}$$

$$a_E = D_e + \max(-F_e, 0) \tag{3.83b}$$

$$a_P = a_W + a_E + (F_e - F_w) \tag{3.83c}$$

and the deferred correction source term is

$$\begin{aligned} S^{DC} = & \frac{1}{2}\left[\max(-F_e, 0)\varphi(r_e^-) + \max(F_e, 0)\varphi(r_e^+)\right](\phi_P - \phi_E) \\ & \frac{1}{2}\left[\max(-F_w, 0)\varphi(r_w^+) + \max(F_w, 0)\varphi(r_w^-)\right](\phi_P - \phi_W) \end{aligned} \tag{3.84}$$

As it is discussed in QUICK scheme, neighbor and central coefficients of TVD schemes are same with UD scheme (Eqns. 3.33 and 3.34) with the addition of deferred correction source term for stability and non-oscillatory solution concerns.

3.3 Extension of Numerical Schemes to Two-dimensions

The steady, one-dimensional convection-diffusion problem is already given by equation 3.10 and the same steady problem could be extended to two-dimensions as follows:

$$\frac{\partial}{\partial x}(\rho u \phi) + \frac{\partial}{\partial y}(\rho v \phi) = \frac{\partial}{\partial x}\left(\Gamma \frac{\partial \phi}{\partial x}\right) + \frac{\partial}{\partial y}\left(\Gamma \frac{\partial \phi}{\partial y}\right) \tag{3.85}$$

where two coupled conservation equations, for $\phi = u$ and $\phi = v$, need to be solved.

The two-dimensional discretized form of the aforementioned two-dimensional convection-diffusion problem, applicable for CD, UD, HD, exponential and power-law schemes, could be written as

$$a_P \phi_P = a_E \phi_E + a_W \phi_W + a_N \phi_N + a_S \phi_S \tag{3.86}$$

where the central coefficient is given by

$$a_P = a_E + a_W + a_N + a_S + (F_e - F_w) + (F_n - F_s) \tag{3.87}$$

For two dimensional flows, values of mass flow rate through the face (F) and diffusion

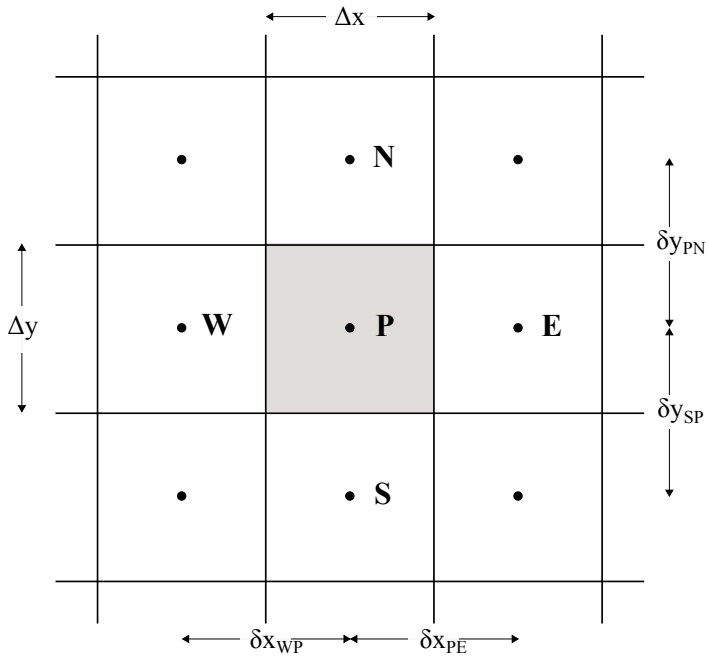

Figure 3.7: Two dimensional computational cell

conductance (D) are given as

$$F_e = (\rho u)_e A_e \qquad D_e = \frac{\Gamma_e}{\delta x_{EP}} A_e \tag{3.88a}$$

$$F_w = (\rho u)_w A_w \qquad D_w = \frac{\Gamma_w}{\delta x_{PW}} A_w \tag{3.88b}$$

$$F_n = (\rho v)_n A_n \qquad D_n = \frac{\Gamma_n}{\delta y_{NP}} A_n \tag{3.88c}$$

$$F_s = (\rho v)_s A_s \qquad D_s = \frac{\Gamma_s}{\delta y_{PS}} A_s \tag{3.88d}$$

where δy_{NP} defines the distance between centers of N and P cells in $y-$direction. A_e, A_w A_n, and A_s are the areas of the east, west, north and south faces of the central node, respectively. For two-dimensional grids, areas of the faces are $A_e = A_w = \Delta y \times 1$ and $A_n = A_s = \Delta x \times 1$. Since the interrogation windows of PIV measurements are squares with same size in the complete flow-field, all δy, δx, Δy and Δx values are equal to each other which brings an additional ease for the application of

present methodology.

Tables 3.4 and 3.5 list the neighbor coefficients for all previously discussed schemes.

Table 3.4: Neighbor coefficients for central, upwind and hybrid differencing schemes

	CD	UD	Hybrid Diff.
a_E	$D_e - F_e/2$	$D_e + \max(-F_e, 0)$	$\max[-F_e, (D_e - F_e/2), 0]$
a_W	$D_w + F_w/2$	$D_w + \max(F_w, 0)$	$\max[F_w, (D_w + F_w/2), 0]$
a_N	$D_n - F_n/2$	$D_n + \max(-F_n, 0)$	$\max[-F_n, (D_n - F_n/2), 0]$
a_S	$D_s + F_s/2$	$D_s + \max(F_s, 0)$	$\max[F_s, (D_s + F_s/2), 0]$

Table 3.5: Neighbor coefficients for power-law and exponential schemes

	Power-law	Exponential
a_E	$D_e \max[0, (1 - 0.1\|Pe_e\|)^5] + \max[-F_e, 0]$	$F_e \Big/ \big[\exp(Pe_e) - 1\big]$
a_W	$D_w \max[0, (1 - 0.1\|Pe_w\|)^5] + \max[F_w, 0]$	$F_w \exp(Pe_w) \Big/ \big[\exp(Pe_w) - 1\big]$
a_N	$D_n \max[0, (1 - 0.1\|Pe_n\|)^5] + \max[-F_n, 0]$	$F_n \Big/ \big[\exp(Pe_n) - 1\big]$
a_S	$D_s \max[0, (1 - 0.1\|Pe_s\|)^5] + \max[F_s, 0]$	$F_s \exp(Pe_s) \Big/ \big[\exp(Pe_s) - 1\big]$

For TVD schemes, including QUICK scheme, two-dimensional discretization equation is same with other schemes with the addition of DCS term

$$a_P\phi_P = a_E\phi_E + a_W\phi_W + a_N\phi_N + a_S\phi_S + S^{DC} \tag{3.89}$$

The central coefficient is also given by equation 3.87 and the neighbor coefficients are

same with UD as in Table 3.4. Moreover, the two-dimensional DCS term is written as

$$
\begin{aligned}
S^{DC} = \; & \frac{1}{2}\Big[\max(-F_e,0)\varphi(r_e^-) + \max(F_e,0)\varphi(r_e^+)\Big](\phi_P - \phi_E) + \\
& \frac{1}{2}\Big[\max(-F_w,0)\varphi(r_w^+) + \max(F_w,0)\varphi(r_w^-)\Big](\phi_P - \phi_W) + \\
& \frac{1}{2}\Big[\max(-F_n,0)\varphi(r_n^-) + \max(F_n,0)\varphi(r_n^+)\Big](\phi_P - \phi_N) + \\
& \frac{1}{2}\Big[\max(-F_s,0)\varphi(r_s^+) + \max(F_s,0)\varphi(r_s^-)\Big](\phi_P - \phi_S)
\end{aligned}
\tag{3.90}
$$

The gradient ratios, r, in the above equation could be written for a two-dimensional grid points as follows:

$$r_e^+ = \frac{\phi_P - \phi_W}{\phi_E - \phi_P} \qquad r_e^- = \frac{\phi_{EE} - \phi_E}{\phi_E - \phi_P} \tag{3.91a}$$

$$r_w^+ = \frac{\phi_W - \phi_{WW}}{\phi_P - \phi_W} \qquad r_w^- = \frac{\phi_E - \phi_P}{\phi_P - \phi_W} \tag{3.91b}$$

$$r_n^+ = \frac{\phi_P - \phi_S}{\phi_N - \phi_P} \qquad r_n^- = \frac{\phi_{NN} - \phi_N}{\phi_N - \phi_P} \tag{3.91c}$$

$$r_s^+ = \frac{\phi_S - \phi_{SS}}{\phi_P - \phi_S} \qquad r_s^- = \frac{\phi_N - \phi_P}{\phi_P - \phi_S} \tag{3.91d}$$

where the numerator is the upstream gradient and the denominator is the downstream gradient.

The same practice could be easily followed in three dimensions for tomographic PIV [82, 83], but here our focus of interest is on planar PIV measurements, so this extension is kept as a future work.

3.4 Projection of PIV Data on Computational Grid

In planar PIV applications both u and v components of the velocity are measured at the center of the measurement window. Figure 3.8 shows an example PIV measurement grid with 4×4 cells. The grid in which all variables are stored at the same location as in Figure 3.8 is known as collocated grid.

One other form of arrangement for the flow variables is proposed by Harlow and Welch [84] known as staggered grid arrangement. In staggered grids, the scalar variables such as pressure, temperature, density, etc., are stored at the center of cell volumes; whereas the velocity components are stored at the center of cell faces. This formation is originally used for avoiding the checkerboard distribution [50,51]. Moreover, staggered grid arrangement leads to have velocities at the exact location where they are needed, i.e. inlet and outlet of the control volume. Thus, no interpolation is needed for calculation of face values. The solution algorithm used in the thesis relies on the SIMPLER algorithm of Patankar [24] which is originally derived for staggered grids. In CFD calculations, use of staggered grid for SIMPLER algorithm is not mandatory, but for PIV pressure estimations that will cease the need for boundary condition implementations. Thus, the measured velocity values would behave as boundary conditions to the pressure estimation procedure.

The staggered grid that could be derived from the measured 4×4 flow-field is given in Figure 3.9. The measured velocities are linearly interpolated to acquire cell face velocities. The velocity vector between two cell centers are interpolated as

$$\begin{aligned} u_{i,j} &= (u_{i,j}^{PIV} + u_{i+1,j}^{PIV})/2 \\ v_{i,j} &= (v_{i,j}^{PIV} + v_{i,j+1}^{PIV})/2 \end{aligned} \tag{3.92}$$

The measured velocities, u^{PIV} and v^{PIV}, have dimensions of $[4, 4]$; but due to the interpolation, the interpolated $u-$velocity has dimensions of $[3, 4]$ and $v-$velocity has dimensions of $[4, 3]$. In general, as a result of interpolation, the extracted velocities for the computational study are reduced by one dimension in corresponding flow direction of the measured velocities. In general, a $m \times n$ experimental flow-field will result as a $u-$velocity field with $m - 1 \times n$ elements and a $v-$velocity field with

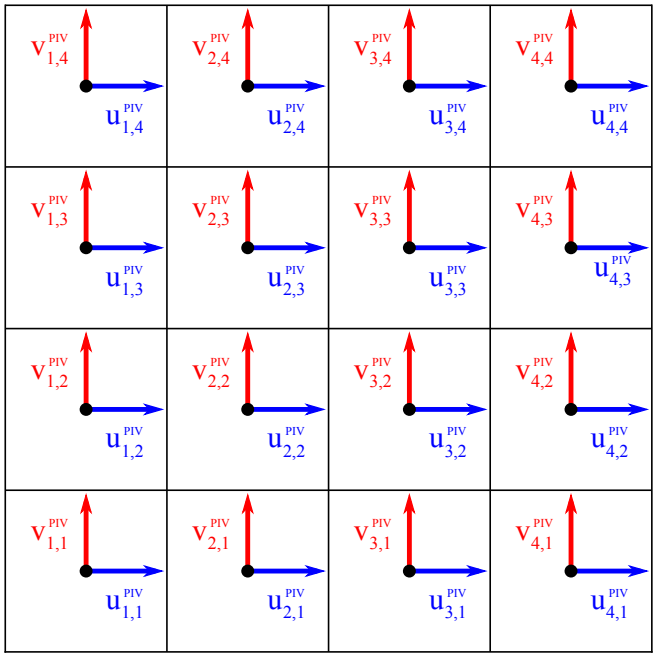

Figure 3.8: A 4×4 PIV measurement grid

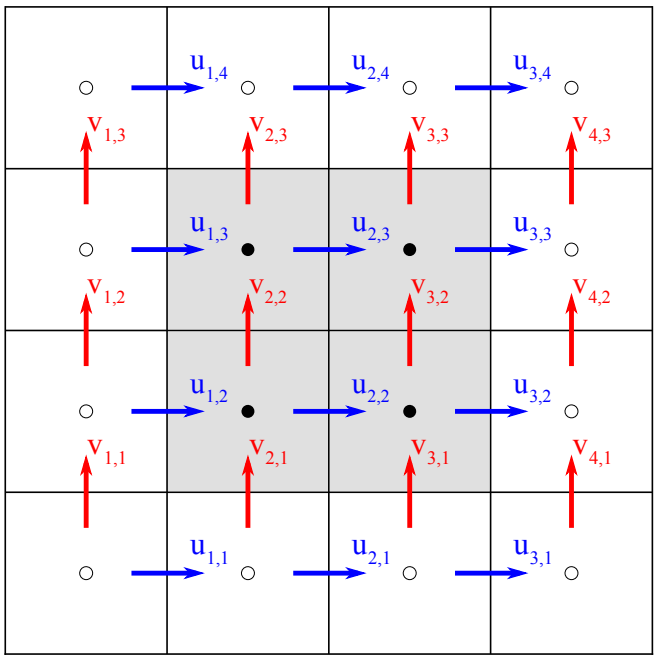

Figure 3.9: Computational grid derived from 4×4 PIV measurement grid

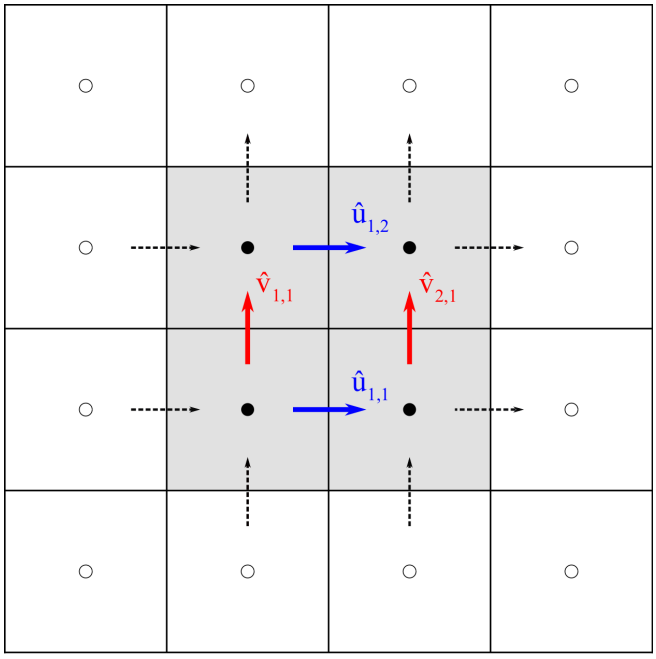

Figure 3.10: Pseudo-velocities on computational grid derived from 4×4 PIV measurement grid

$m \times n - 1$ elements.

To be able to calculate the net momentum flux through a cell, all velocities at the center of each surrounding faces are needed. As seen in Figure 3.9, the outermost cells of 4×4 volume lack at least one velocity - corner cells lack two velocities - at their faces. Only the inner shaded cells have velocities defined around all of their four faces. So, the 4×4 measurement volume loses the surrounding cells and reduces to the shaded 2×2 volume for pressure estimations. In general, during the projection, a $m \times n$ experimental collocated grid becomes a $m-2 \times n-2$ computational staggered grid, which is shown in Figure 3.10.

Pressure estimation will be held for the shaded cells of Figure 3.10. Here the dashed lines denotes the velocities which will behave as boundary condition for present methodology. These velocities will be not be altered throughout the iterations, but the hatted velocities, which are known as pseudo-velocities of the algorithm, will be corrected during iterations.

The procedure that is discussed up to now for velocity interpolation from PIV data

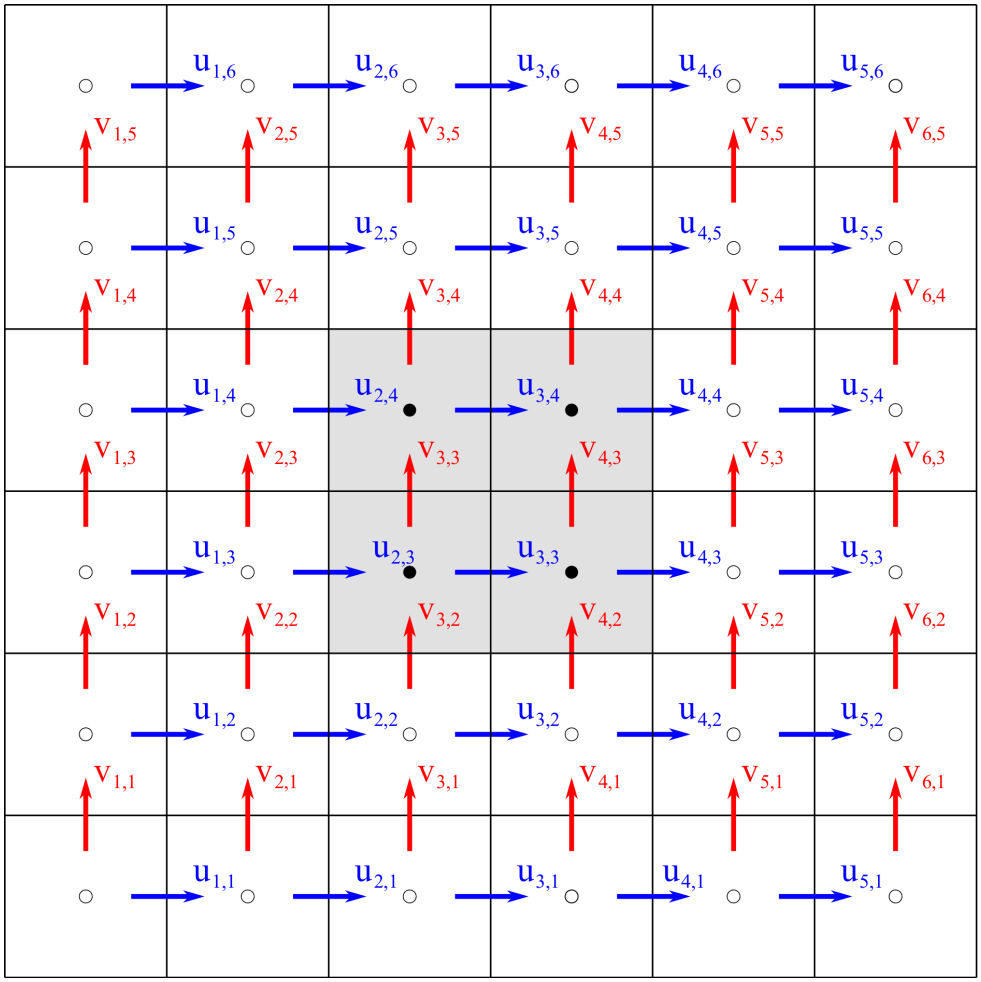

Figure 3.11: A 6×6 PIV measurement grid for TVD schemes. Shaded area denotes the cells for which pressure would be estimated.

is valid for non-TVD (UD, CD, HD, LUD, etc.) schemes. For TVD schemes as previously discussed, we need two downstream and upstream values for calculation of r parameters in the Deferred Correction Source term, S^{DC}. To achieve this, two cells will be left at the boundaries of the computational area for which pressure will be estimated. To have the same 2-by-2 computational grid, for TVD schemes we need to start with a 6-by-6 measurement grid. Figure 3.11 shows the measurement grid to acquire the same 2-by-2 computational grid of non-TVD schemes (Fig. 3.9). The pseudo-velocities of that grid would be exactly same with Figure 3.10, but this time one more boundary value for velocities would be used. Rather than this projection procedure, all steps of the algorithm are same for TVD and non-TVD schemes.

3.5 SIMPLE Family Algorithms

The focus of interest for the thesis is planar PIV measurements. Thus, rather than initializing u and v components of velocity as in CFD calculations, here the procedure will be initialized with already available velocity data. Up to now, in all above practice, schemes for the general variable ϕ is studied. At this section, the diffusion coefficient, Γ, will be replaced with dynamic viscosity μ and the general variable ϕ will be replaced with u and v to obtain $x-$ and $y-$momentum equations. Doing this will give the governing equations for steady, incompressible, two-dimensional flows as

continuity equation,

$$\frac{\partial}{\partial x}(\rho u) + \frac{\partial}{\partial y}(\rho v) = 0 \tag{3.93}$$

x-momentum equation,

$$\frac{\partial}{\partial x}(\rho u u) + \frac{\partial}{\partial y}(\rho v u) = -\frac{\partial p}{\partial x} + \frac{\partial}{\partial x}\left(\mu \frac{\partial u}{\partial x}\right) + \frac{\partial}{\partial y}\left(\mu \frac{\partial u}{\partial y}\right) + S_u \tag{3.94}$$

y-momentum equation,

$$\frac{\partial}{\partial x}(\rho u v) + \frac{\partial}{\partial y}(\rho v v) = -\frac{\partial p}{\partial y} + \frac{\partial}{\partial x}\left(\mu \frac{\partial v}{\partial x}\right) + \frac{\partial}{\partial y}\left(\mu \frac{\partial v}{\partial y}\right) + S_v \tag{3.95}$$

where μ is dynamic viscosity and S is the source term per unit volume.

The above momentum conservation equations are derived from equation 3.85 - that defines the convection-diffusion problem- by replacing general variable ϕ with u and v velocities and the diffusion conductance with dynamic viscosity, μ. The source terms which is absent in equation 3.85 may introduce the effect of any momentum source into the conservation equations. Furthermore, the pressure gradient could also be included in the general source term; but in fluid flows pressure gradient has a significant role in terms of momentum change, so it is explicitly defined as another term.

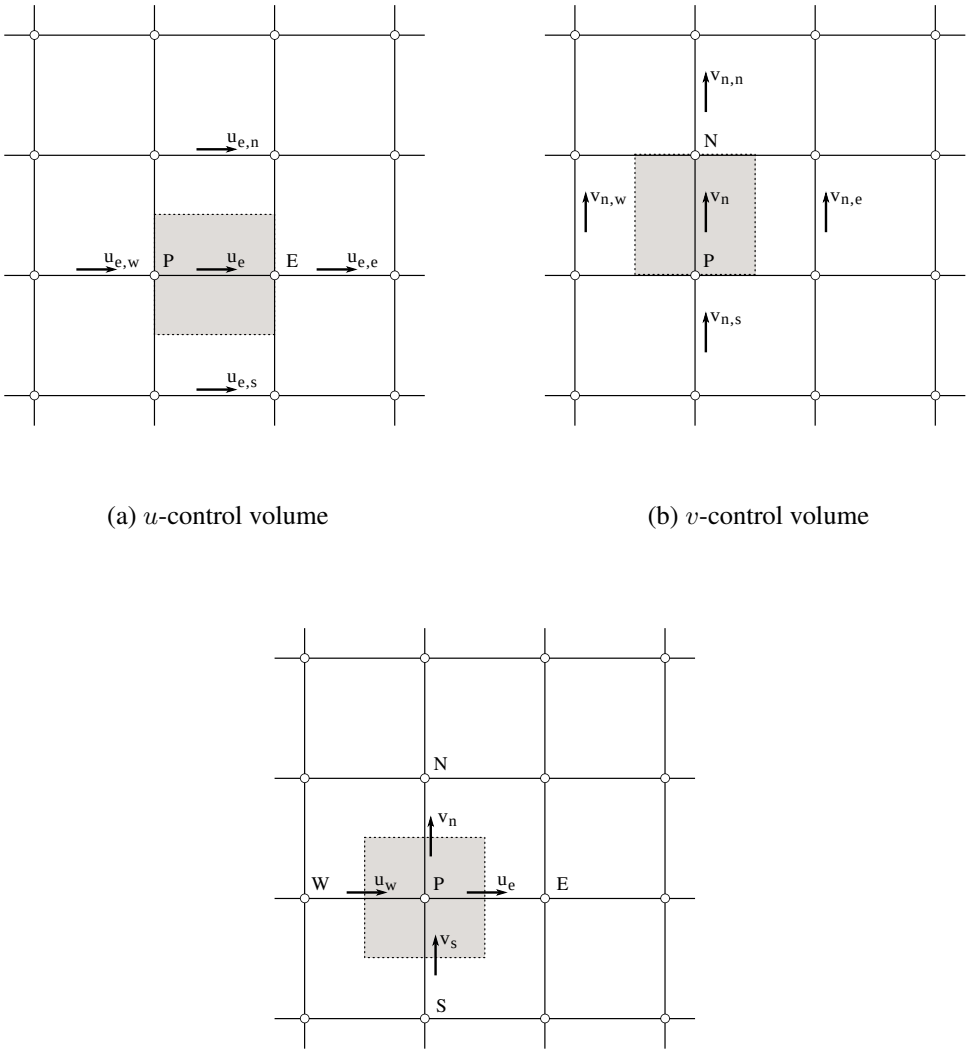

(a) u-control volume

(b) v-control volume

(c) pressure control volume

Figure 3.12: Staggered control volumes for calculation

The procedure on pressure estimation will be explained on steady flows first, then the extension to unsteady flows will be explained in a separate section. The conservation equations would be applied on the computational grid for which the projection from measurement grid is described in Section 3.4. Figure 3.12 shows the control volumes for conservation of $x-$momentum, conservation of $y-$momentum and continuity equation for a sample cell. As shown in Fig. 3.9, the circles are defining the locations at where pressure is estimated and the velocities are defined at the faces

between neighboring pressure points.

The four cardinal directions are used for indexing the elements, with the central node of interest being called P. The shaded area in Figure 3.12c gives the pressure control volume around point P for continuity equation. Then the neighboring pressure cells are named according to their position with respect to the reference point P. The velocities entering and leaving the control volume are also named according to their position with respect to the pressure point P, but this time with a subscript. In the upcoming methodology, the neighboring velocities of any velocity component should also be included into momentum conservation calculations around that central velocity component. Thus, another indexing system is needed for the velocities defined in Fig. 3.12c. Here, we used a second subscript to denote the position of the neighboring velocities with respect to central velocity. Figure 3.12a shows the neighboring velocities $u_{e,n}$, $u_{e,s}$, $u_{e,e}$ and $u_{e,w}$ for central velocity u_e. Similarly, the neighboring velocities $v_{n,n}$, $v_{n,s}$, $v_{n,e}$ and $v_{n,w}$ of central velocity v_n are given in Figure 3.12b.

3.5.1 Momentum Equations

A staggered control volume for $x-$momentum equation around u_e is given in Fig. 3.12a. The discretized form of the $x-$momentum equation will be constructed by implementing the discretized pressure gradient and source term to equation 3.86. Volume integration of the pressure term on the $x-$momentum control volume gives

$$\begin{aligned}\int_{CV} -\frac{\partial p}{\partial x} d\mathcal{V}_u &= -\frac{p_E - p_P}{\delta x_{EP}} \Delta\mathcal{V} \\ &= -\frac{p_E - p_P}{\delta x_{EP}} \delta x \delta y \\ &= (p_P - p_E)\delta y\end{aligned} \tag{3.96}$$

and the integrated source term may be denoted as

$$\int_{CV} S_u d\mathcal{V} = b_u \tag{3.97}$$

Finally, the discretized $x-$momentum equation becomes

$$a_e u_e = a_{e,e} u_{e,e} + a_{e,w} u_{e,w} + a_{e,n} u_{e,n} + a_{e,s} u_{e,s} + (p_P - p_E) A_e + b_u \tag{3.98}$$

where b_u is the $x-$momentum source term, $(p_P - p_E)A_e$ is the driving pressure force acting on the computational cell and A_e is the cell face of the control volume where the pressure difference acts. For two-dimensional case, the cell face area is $\delta y \times 1$; whereas for three-dimensional case it will be $\delta y \times \delta z$. The above equation may be reassigned in a more compact form given as

$$a_e u_e = \sum a_{nb} u_{nb} + (p_P - p_E) A_e + b_u \tag{3.99}$$

where the central coefficient is

$$a_e = a_{e,e} + a_{e,w} + a_{e,n} + a_{e,s} + (F_e - F_w) + (F_n - F_s) \tag{3.100}$$

The summation $\sum a_{nb} u_{nb}$ includes the effect of all four neighbors as shown in Figure 3.12a. Calculation of the neighboring coefficients are already described in section 3.2 in details.

The $y-$momentum equation could be gathered through the same practice to achieve the following final discretized equation

$$a_n v_n = \sum a_{nb} v_{nb} + (p_P - p_N) A_n + b_v \tag{3.101}$$

and the central coefficient for $v-$momentum equation is given as

$$a_n = a_{n,e} + a_{n,w} + a_{n,n} + a_{n,s} + (F_e - F_w) + (F_n - F_s) \tag{3.102}$$

The F values will be calculated at the faces of the control volume. Since there is no exact velocity at the faces of the velocity control volumes, two velocity values in the neighborhood of the face are interpolated. For $x-$momentum equation, F_e and

F_w will be calculated by taking the average of central velocity and velocity of the related face, i.e. $u_{e,e}$ and $u_{e,w}$. F_n and F_s will be calculated by taking the average of two v velocities at the two corners of the related face. Similarly, for $y-$momentum equation, F_e and F_w will be calculated by taking average of two u velocities at the two corners of the related face. This time, F_n and F_s will be calculated by taking the average of central velocity and velocity of the related face, i.e. $v_{n,n}$ and $v_{n,s}$.

Calculation of convective fluxes could be exemplified on the computational grid shown in Figure 3.9 around $u_{2,3}$ and $u_{3,3}$. The F values for the control volume around $u_{2,3}$ are given as

$$\begin{aligned} F_e &= \frac{1}{2}\rho(u_{2,3} + u_{3,3})A_e & F_w &= \frac{1}{2}\rho(u_{1,3} + u_{2,3})A_w \\ F_n &= \frac{1}{2}\rho(v_{2,3} + v_{3,3})A_n & F_s &= \frac{1}{2}\rho(v_{2,2} + v_{3,2})A_s \end{aligned} \tag{3.103}$$

Similarly, the F values for the control volume around $v_{3,2}$ are

$$\begin{aligned} F_e &= \frac{1}{2}\rho(u_{3,2} + u_{3,3})A_e & F_w &= \frac{1}{2}\rho(u_{2,2} + u_{2,3})A_w \\ F_n &= \frac{1}{2}\rho(v_{3,2} + v_{3,3})A_n & F_s &= \frac{1}{2}\rho(v_{3,1} + v_{3,2})A_s \end{aligned} \tag{3.104}$$

The diffusion coefficient, Γ, is replaced with dynamic viscosity, μ, for momentum equations. Then, the diffusion conductance values for the control volumes around $u_{2,3}$ and $v_{3,2}$ become equal and given by

$$\begin{aligned} D_e &= \frac{\mu}{\delta x}A_e & D_w &= \frac{\mu}{\delta x}A_w \\ D_n &= \frac{\mu}{\delta y}A_n & D_s &= \frac{\mu}{\delta y}A_s \end{aligned} \tag{3.105}$$

As previously discussed in Section 3.3, for two-dimensional grids, areas of the faces are $A_e = A_w = \Delta y \times 1$ and $A_n = A_s = \Delta x \times 1$. Since the interrogation windows for PIV data are mostly squares with same size in the whole flow-field; all δy, δx, Δy and Δx values are equal to each other and all diffusion conductance values are equal to the dynamic viscosity, μ.

3.5.2 Velocity Correction Equations

The momentum equations for two-dimensional flows are given by equations 3.99 and 3.101 and will give the correct velocities if one supplies the correct pressure field. Since the correct values satisfying the conservation equation will be achieved after the convergence of the iterative process, one could call the intermediate values of velocity and pressure as guessed velocities and pressures. Here, these guessed values will be denoted by a superscript of *. The momentum equations with guessed-starred-velocity and pressure fields are given as follows:

$$a_e u_e^* = \sum a_{nb} u_{nb}^* + (p_P^* - p_E^*) A_e + b_u \tag{3.106}$$

$$a_n v_n^* = \sum a_{nb} v_{nb}^* + (p_P^* - p_N^*) A_n + b_v \tag{3.107}$$

At this point, one may define the correct pressure and velocity values as follows:

$$p = p^* + p' \tag{3.108}$$

$$u = u^* + u' \tag{3.109}$$

$$v = v^* + v' \tag{3.110}$$

where p' is defined as *pressure correction* which is the difference between the correct pressure value and the guessed pressure value at the moment of the iteration. Similarly, the u' and v' terms are being the u and v velocity corrections denoting the difference between the correct and guessed velocity values.

Subtracting Eqs. 3.106 and 3.107 from Eqs. 3.99 and 3.101 gives

$$a_e(u_e - u_e^*) = \sum a_{nb}(u_{nb} - u_{nb}^*) + [(p_P - p_P^*) - (p_E - p_E^*)] A_e \tag{3.111}$$

$$a_n(v_n - v_n^*) = \sum a_{nb}(v_{nb} - v_{nb}^*) + [(p_P - p_P^*) - (p_N - p_N^*)] A_n \tag{3.112}$$

Plugging the previously defined pressure and velocity correction definitions to Eqs. 3.111 and 3.112 gives:

$$a_e u'_e = \sum a_{nb} u'_{nb} + (p'_P - p'_E) A_e \tag{3.113}$$

$$a_n v'_n = \sum a_{nb} v'_{nb} + (p'_P - p'_N) A_n \tag{3.114}$$

Eqs. 3.113 and 3.114 are known as velocity correction equations which are totally same with source-free momentum conservation equations (Eqs. 3.99 and 3.101) but this time defined for velocity corrections. At this point Patankar [24] recommends to drop the terms $\sum a_{nb} u'_{nb}$ and $\sum a_{nb} v'_{nb}$. The motivation for dropping terms would be explained in the next section after deriving the pressure correction equation. Now, dropping the terms gives Eqs. 3.113 and 3.114 as

$$a_e u'_e = (p'_P - p'_E) A_e \tag{3.115}$$

$$a_n v'_n = (p'_P - p'_N) A_n \tag{3.116}$$

or

$$u'_e = d_e (p'_P - p'_E) \tag{3.117}$$

$$v'_n = d_n (p'_P - p'_N) \tag{3.118}$$

where

$$d_e \equiv \frac{A_e}{a_e} \qquad\qquad d_n \equiv \frac{A_n}{a_n} \tag{3.119}$$

Plugging the new values of velocity corrections to Eqs. 3.109 and 3.110 gives

$$u_e = u^*_e + d_e (p'_P - p'_E) \tag{3.120}$$

$$v_n = v^*_n + d_n (p'_P - p'_N) \tag{3.121}$$

This shows us how the guessed velocities are corrected at each iteration. As velocity and pressure corrections tend to go zero, the solution will converge to the correct values.

3.5.3 Pressure Correction Equation

Pressure, one of the most important parameters for transport of momentum, appears in momentum conservation equations (Eqs. 3.99 and 3.101); but still there is no dedicated equation for itself. At this point, Patankar [24] recommends to use the continuity equation for coupling velocity to the pressure which is the basis of Semi-Implicit Method for Pressure-Linked Equations (SIMPLE) algorithm family. To achieve this, the continuity equation (3.93) will be integrated for the two-dimensional control volume, shown in Fig. 3.12c, which gives

$$\rho u_e A_e - \rho u_w A_y + \rho u_n A_n - \rho u_s A_s = 0 \tag{3.122}$$

Plugging the previously defined velocity correction formulas (3.120 and 3.121) into integrated form of continuity equation gives

$$\begin{aligned} &\rho A_e(u_e^* + d_e(p'_P - p'_E)) - \rho A_w(u_w^* + d_w(p'_W - p'_P)) + \\ &\rho A_n(v_n^* + d_n(p'_P - p'_N)) - \rho A_s(v_s^* + d_s(p'_S - p'_P)) \qquad = 0 \end{aligned} \tag{3.123}$$

Collecting the pressure terms together gives

$$\begin{aligned} &\rho(A_e d_e + A_w d_w + A_n d_n + A_s d_s)p'_P = \\ &\rho(A_e d_e p'_E + A_w d_w p'_W + A_n d_n p'_N + A_s d_s p'_S) + \\ &\rho(A_w u_w^* - A_e u_e^* + A_s v_s^* - A_n v_n^*) \end{aligned} \tag{3.124}$$

Rearranging gives

$$a_P p'_P = a_E p'_E + a_W p'_W + a_N p'_N + a_S p'_S + b'_P \tag{3.125}$$

where

$$
\begin{aligned}
a_E &= \rho A_e d_e \\
a_W &= \rho A_w d_w \\
a_N &= \rho A_n d_n \\
a_S &= \rho A_s d_s \\
b'_P &= \rho A_w u^*_w - \rho A_e u^*_e + \rho A_s v^*_s - \rho A_n v^*_n
\end{aligned}
\tag{3.126}
$$

Equation 3.125 is the pressure correction equation derived from discrete continuity equation (3.122). It is significant to note that the right hand side term b'_P is the negative of the continuity equation and arises due to the incorrect guess velocities, u^* and v^*. Thus, this term behaves as a source term indicating the mass imbalance at the current iteration. Solution of equation 3.125 gives the pressure correction field which aims to diminish the mass imbalance.

Previously, in section 3.5.2 Patankar's recommendation of dropping the $\sum a_{nb} u'_{nb}$ and $\sum a_{nb} v'_{nb}$ terms were mentioned. Deriving the pressure correction equation lets us a better background for explanation of this approximation, thus we will explain the motivation here. If we did not omit $\sum a_{nb} u'_{nb}$ and $\sum a_{nb} v'_{nb}$ terms, then they should be defined in terms of velocity and pressure corrections at their neighbors. Subsequently, these neighbors will also include their neighbors and at the end we need to solve the continuity and momentum equations for all grid points. Moreover, omission of $\sum a_{nb} u'_{nb}$ and $\sum a_{nb} v'_{nb}$ terms will not pose any errors for the converged solution, since the values of corrections will be within the allowed tolerance for the converged solution. The aim here is to get an intermediate step for deriving the pressure correction equation.

3.6 SIMPLER Algorithm

The algorithm used in the thesis is a variant of the original SIMPLE algorithm known as SIMPLER (Simple-Revised) [25]. The main motivation of SIMPLER algorithm is to improve the rate of convergence of the SIMPLE algorithm by using p' to correct only velocity fields. One other benefit of the algorithm for pressure estimation from

PIV data relies on the fact that if one gives the correct velocity field in the first iteration, the algorithm will give the correct pressure field directly without any further computation.

In previous chapters, all needed equations are derived for SIMPLE algorithm, but SIMPLER algorithm demands to define one more parameter known as pseudo-velocities. To achieve this, the discretized momentum equations given in Eqs. 3.99 and 3.101 could be written as

$$u_e = \frac{\sum a_{nb} u_{nb} + b_u}{a_e} + d_e(p_P - p_E) \tag{3.127}$$

$$v_e = \frac{\sum a_{nb} v_{nb} + b_v}{a_n} + d_n(p_P - p_N) \tag{3.128}$$

Here, we define pseudo-velocities as

$$\widehat{u}_e \equiv \frac{\sum a_{nb} u_{nb} + b_u}{a_e} \tag{3.129}$$

$$\widehat{v}_n \equiv \frac{\sum a_{nb} v_{nb} + b_v}{a_n} \tag{3.130}$$

which contains the neighbor velocities in it without any pressure information. From here, the momentum equation could be rewritten as

$$u_e = \widehat{u}_e + d_e(p_P - p_E) \tag{3.131}$$

$$v_e = \widehat{v}_n + d_n(p_P - p_N) \tag{3.132}$$

It is seen that the above equations are similar with velocity correction equations (3.120 and 3.121) except that p takes place of p' and $\widehat{u}$ takes place of u^*. Substituting the new form of velocities given above to the integrated continuity equation (3.122) and following the same practice in Section 3.5.3 gives the pressure equation as

$$a_P p_P = a_E p_E + a_W p_W + a_N p_N + a_S p_S + b_P \tag{3.133}$$

where

$$
\begin{aligned}
a_E &= \rho A_e d_e \\
a_W &= \rho A_w d_w \\
a_N &= \rho A_n d_n \\
a_S &= \rho A_s d_s \\
b_P &= \rho A_w \widehat{u}_w - \rho A_e \widehat{u}_e + \rho A_s \widehat{v}_s - \rho A_n \widehat{v}_n
\end{aligned}
\tag{3.134}
$$

The acquired pressure equation is similar with the pressure correction equation (3.125) with the replacement of b'_P with b_P and the use of pseudo-velocities instead of starred velocities in mass imbalance definitions. One significant difference of pressure equation with the pressure correction equation is that, here, no approximations of dropping the $a_{nb}u'_{nb}$ and $\sum a_{nb}v'_{nb}$ terms are applied. This will result as having the correct pressure field in the first iteration, if correct velocities are supplied for pseudo-velocity calculations. Since the measured velocity fields are close to the real flow velocities within the tolerance of the experimental system, pressure estimation methodology will converge in a few iterations. So, the present procedure will not be computationally expensive.

The sequence of the SIMPLER algorithm is given as follows:

1. Start with the interpolated velocity field from PIV data.
2. Calculate the momentum equation coefficients (a_e, a_n, etc.) for related scheme. Then, calculate the pseudo-velocities from Eqs. 3.129 and 3.130.
3. Calculate the pressure equation coefficients (a_E, a_N, etc.) from equation 3.134. Then solve pressure equation (3.133) to yield p^*.
4. Using calculated pressure field, p^*, solve momentum equations (3.106 and 3.107) to obtain u^* and v^*.
5. Solve pressure correction equation (3.125) to obtain p' field.
6. Correct the velocity fields through velocity correction equations (3.111 and 3.112) with the calculated p' field.

7. If solution is converged, stop; otherwise, go to second step.

In SIMPLER algorithm, one simply obtains a pressure field from the given initial velocity field and progressively corrects the velocity field to diminish the mass imbalance in pressure correction equation. For CFD solutions this step starts with an educated guess of the initial flow-field for the related problem, but here for PIV pressure estimations one already has a measured velocity field. Thus, in a few iterations the solution will converge and give the continuity-satisfying pressure field. One may also conclude that there will be some minor modifications in the initial measured PIV velocity field to satisfy the governing equations. The level of modification on the velocity field in each iteration could be controlled by the user through relaxation factors which would be described in the next section. Even if it seems that the pressure field should be strictly two-dimensional for current procedure, Murai *et al.* [85] showed that in plane divergence is negligible for two-dimensional PIV experiments.

3.7 Solution Procedure

In previous chapters, the numerical procedure for discretization of the governing equations to form a set of linear algebraic equations are discussed. The next step would be the definition of a consistent matrix solver algorithm for the solution of this set of algebraic equations. One reliable method for this purpose is given by Thomas [86], known as Tri-diagonal Matrix Algorithm (TDMA) or Thomas Algorithm. The method is a simplified form of Gaussian elimination on tri-diagonal system of equations through forward elimination and a subsequent back-substitution. TDMA is a direct solver for one-dimensional problems; but here, for two-dimensional case, we use it in a line-by-line sweep fashion to solve the set of equations iteratively. As an example, the two-dimensional momentum equation (3.89) could be rearranged in the following form to get a tri-diagonal matrix for the terms on a certain $N - S$ line

$$-a_S\phi_S + a_P\phi_P - a_N\phi_N = a_E\phi_E + a_W\phi_W + S^{DC} \tag{3.135}$$

The existing iteration will start at furthermost $N - S$ line and the line will be swept to the other direction, i.e. East-to-West or West-to-East. The iteration will be ended when the last $N - S$ line in the opposite direction is reached. The velocities at the boundaries are behaving as boundary conditions for the present procedure. So, changing sweep direction with progressive iterations may help to distribute the boundary information equally.

During the iteration process, one may encounter with very high corrections which can diverge the general solution. Since the aim here is to acquire pressure from already tuned velocity field, some under-relaxation to the velocities will be introduced for avoiding abrupt changes. Starting from $x-$momentum equation (3.99)

$$a_e u_e = \sum a_{nb} u_{nb} + (p_P - p_E) A_e + b_u \tag{3.136}$$

we may rewrite u_e as

$$u_e = \frac{\sum a_{nb} u_{nb} + (p_P - p_E) A_e + b_u}{a_e} \tag{3.137}$$

recalling that u_e^* is the value of u_e in previous iteration and subtracting it from both sides and rearranging gives

$$u_e = u_e^* + \left(\frac{\sum a_{nb} u_{nb} + (p_P - p_E) A_e + b_u}{a_e} - u_e^* \right) \tag{3.138}$$

Here the terms in parentheses are the change in u_e at current iteration. At this point, one may take only a certain portion of the current change into account and may introduce a relaxation factor α into the equation to get

$$u_e = u_e^* + \alpha_u \left(\frac{\sum a_{nb} u_{nb} + (p_P - p_E) A_e + b_u}{a_e} - u_e^* \right) \tag{3.139}$$

Rearranging gives the under-relaxed form of $x-$momentum equation as

$$\frac{a_e}{\alpha_u}u_e = \sum a_{nb}u_{nb} + (p_P - p_E)A_e + b + \left[(1-\alpha_u)\frac{a_e}{\alpha_u}\right]u_e^* \tag{3.140}$$

Similarly, the $y-$momentum equation with under-relaxation reads

$$\frac{a_n}{\alpha_v}v_n = \sum a_{nb}v_{nb} + (p_P - p_N)A_n + b + \left[(1-\alpha_v)\frac{a_n}{\alpha_v}\right]v_n^* \tag{3.141}$$

If we revisit equation 3.139, it is in the form of velocity corrections given by equation 3.109. Here the velocity correction part is under-relaxed for avoiding abrupt changes those may lead divergence. The velocity corrections are also used in pressure correction equation in the form of equation 3.120. So, the under-relaxations will also update the $d-$terms in the pressure correction equation as

$$d_e = \frac{A_e\alpha_u}{a_e} \qquad\qquad d_n = \frac{A_n\alpha_v}{a_n} \tag{3.142}$$

The under-relaxation factor has a great importance due to convergence issues and should be experimented for each case.

3.8 Unsteady Flows

The present methodology could also be applied on transient data through fully implicit temporal discretization. Integrating $x-$momentum equation (3.2) over a control volume and then over the time difference between two PIV vector fields of Δt and applying divergence theorem to convert volume integrals into surface integrals gives

$$\int_{CV}\int_{t}^{t+\Delta t}\frac{\partial(\rho u)}{\partial t}dtd\mathcal{V} + \int_{t}^{t+\Delta t}\int_{A}\vec{n}\cdot(\rho\vec{V}u)dAdt = \int_{t}^{t+\Delta t}\int_{CV}-\vec{i}\cdot\nabla pd\mathcal{V}dt + \int_{t}^{t+\Delta t}\int_{A}\vec{n}\cdot(\mu\nabla u)dAdt + \int_{t}^{t+\Delta t}\int_{CV}S_u d\mathcal{V}dt \tag{3.143}$$

All terms are same with the steady case except the transient term for unsteady cases. To handle time-dependent flows, the transient term should be discretized. Here, we will use first-order backward differencing scheme which gives the discretized form of the transient term as

$$\int_{CV} \int_{t}^{t+\Delta t} \frac{\partial(\rho u)}{\partial t} dt d\mathcal{V} = \rho \frac{u - u^0}{\Delta t} \Delta \mathcal{V} \tag{3.144}$$

where the superscript '^{0}' denotes the values of variables at time t. In fully implicit scheme, the values of all variables are taken at $t + \Delta t$, so for clarity no superscripts will be used for variables at time $t + \Delta t$. Then, the discretized form of $x-$momentum equation would be

$$\left(a_e + \frac{\rho \Delta \mathcal{V}}{\Delta t}\right) u_e = \sum a_{nb} u_{nb} + (p_P - p_E) A_e + b_u + \frac{\rho \Delta \mathcal{V}}{\Delta t} u_e^0 \tag{3.145}$$

$$\left(a_n + \frac{\rho \Delta \mathcal{V}}{\Delta t}\right) v_n = \sum a_{nb} v_{nb} + (p_P - p_N) A_n + b_v + \frac{\rho \Delta \mathcal{V}}{\Delta t} v_n^0 \tag{3.146}$$

where $\Delta \mathcal{V} = \delta x \delta y$ and Δt is the time difference between two PIV vector fields.

The same practice on transient continuity equation gives the discretized form as

$$\left(\frac{\rho_P - \rho_P^0}{\Delta t}\right) + \rho u_e A_e - \rho u_w A_y + \rho u_n A_n - \rho u_s A_s = 0 \tag{3.147}$$

Equation 3.147 shows that for incompressible flows, the algorithm will not introduce any new terms to pressure and pressure correction equations. Finally, by introducing the new terms in the momentum equations, pressure field for unsteady flows could also be estimated. In PIV pressure estimations, rather than having data only at backwards in time, we will also have the velocities at forward in time $t + \Delta t, +2\Delta t, +3\Delta t, ...$ This may help us for introducing different procedures for handling the time derivative, but at this point we will stick on backward differencing for simplicity.

CHAPTER 4

VALIDATION

This chapter is devoted to the validation of pressure estimation procedure described in Chapter 3. The procedure is implemented to a Fortran program that can handle laminar, steady and unsteady flows with first (hybrid, power-law, central) and higher order schemes. To mimic real viscous PIV data, simulated velocity field obtained from ANSYS Fluent [87] is imported to the program. Pressure is estimated for steady and unsteady flows. The following form of Frobenius norm of error matrix is used for assessing the accuracy:

$$\|\varepsilon_p\|_F = \sqrt{\frac{\sum_{i=1}^{N_x}\sum_{j=1}^{N_y}\left(p - p_{\text{ref}}\right)^2}{N_x N_y}} \tag{4.1}$$

where p_{c} is the correct pressure from numerical simulations, p is the estimated pressure, N_x and N_y are the number of grid elements in the flow-field. The solution of laminar Navier-Stokes equations could also be called as Direct Numerical Simulation (DNS) in the available literature due to not including any modeling in the solution. Even if the simulation results include numerical and truncation errors, to emphasize that this set of data is used as reference for comparison; we call simulation results as correct pressures. To achieve relative error, the absolute error definition is normalized with the Frobenius norm of the correct pressure matrix, $\|p_{\text{c}}\|_F$. As previously discussed, if correct velocity field is implemented to the program, the pressure is estimated in the first iteration without a modification on the velocity field. For complex flow-fields with random errors, further iterations may be needed. The convergence criteria for the procedure is to reduce the mass imbalance to allowable limits, i.e. b'_P term in equation 3.126. In the upcoming section, steady and unsteady validation cases will be discussed alongside with the error and sensitivity analyses.

4.1 Steady Flow

The first case used for steady flow comparison is a rigid-body vortex that is commonly used as a validation case for pressure estimation and error propagation studies [11, 21, 88]. This canonical flow stays as a good candidate for assessing the performance of current methodology. The pressure field, velocity fields and streamlines of the rigid body vortex flow are given in Figure 4.1. The fluid is chosen to be air with density of $\rho = 1.225\ \mathrm{kg/m^3}$ and dynamic viscosity of $\mu = 1.7894 \times 10^{-5}\ \mathrm{Pa \cdot s}$. The rotational speed is $\omega = 2000\ \mathrm{rad/s}$ with the length of the field of interest as $L = 0.0042\ \mathrm{m}$. Pressure is theoretically given by $\frac{1}{2}\rho\omega^2 r^2$ where r is the vortex radius. For the given values, the minimum pressure in the flow-field is $-86.436\ \mathrm{Pa}$ with setting the highest pressure in the given flow-field to $0.0\ \mathrm{Pa}$. In the proposed methodology, we are dealing with pressure gradient rather than absolute pressure. Thus, acquired pressure values will be the differential pressure rather than absolute pressure.

The velocity data is imported to the code and pressure estimated with central, hybrid, power-law and TVD schemes on a 250×250 grid with all square elements. Solution is converged at the first iteration for all cases with the relative error lower than 3×10^{-5}. The algorithm does not correct the velocities those already satisfy the momentum equations. Estimated and correct pressure fields are compared in Figure 4.2 where the correct pressure is given with continuous line and the estimated pressure with symbols only. All the schemes showed similar convergence characteristics for the given flow.

4.2 Error Sensitivity

This section is devoted to the evaluation of solver performance with respect to the random errors in the input data. To achieve this, noise with Gaussian distribution is introduced to input velocity data. Furthermore, to preserve the randomness of procedure, noise contribution is chosen to be totally independent from the local value of the velocity. Probability density function of a random variable x with normal

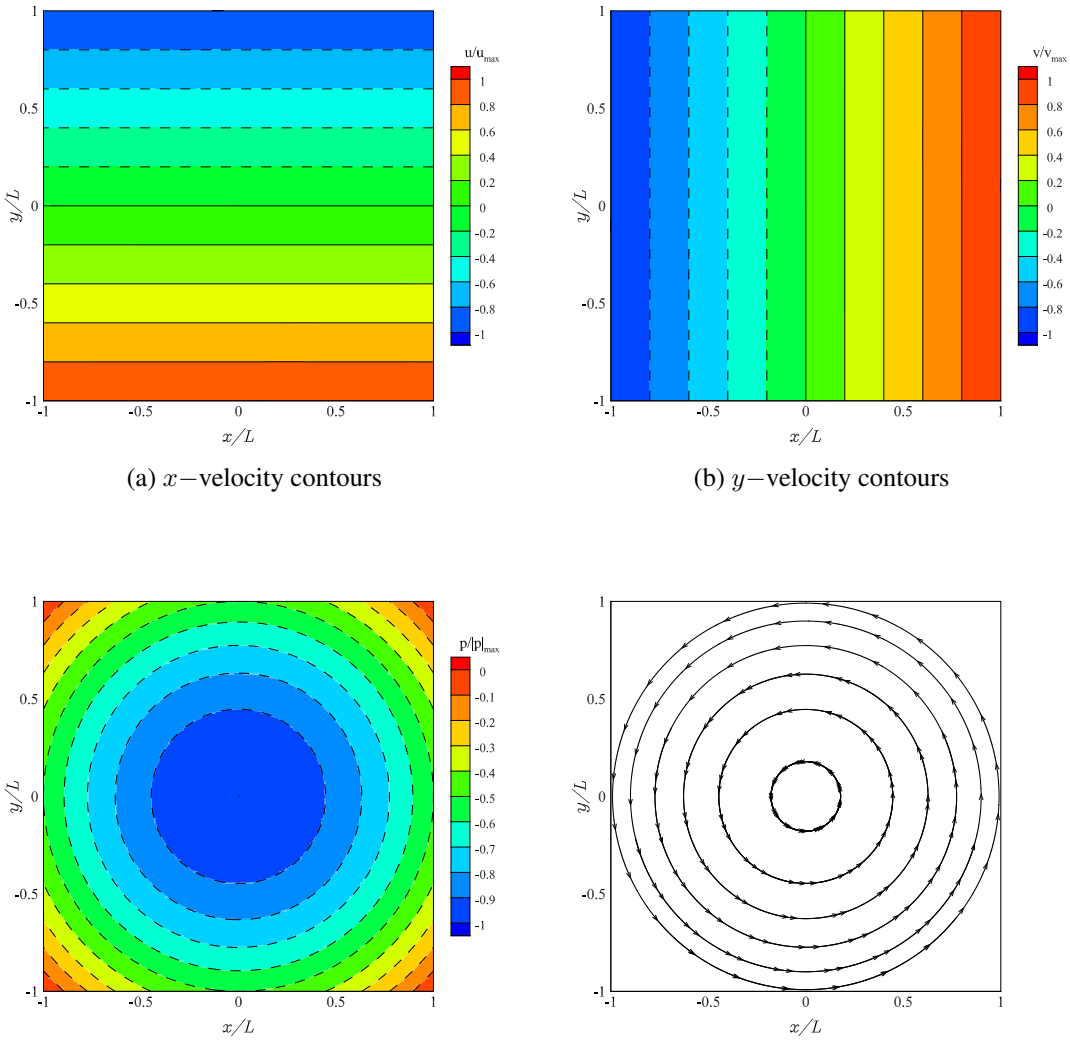

(a) $x-$velocity contours

(b) $y-$velocity contours

(c) Pressure contours

(d) Streamlines

Figure 4.1: Rigid body vortex flow. All contours are normalized with the corresponding maximum value. Negative values are shown with dashed lines.

(Gaussian) distribution is given by

$$P(x) = \frac{1}{\sigma\sqrt{2\pi}} e^{-\frac{(x-\mu)^2}{2\sigma^2}} \tag{4.2}$$

where μ is the mean and σ^2 is the variance of the distributed elements [89]. Thus, the standard deviation would be σ. Figure 4.3 shows a characteristic Gaussian distribution of the random variable for zero mean, $\mu = 0$.

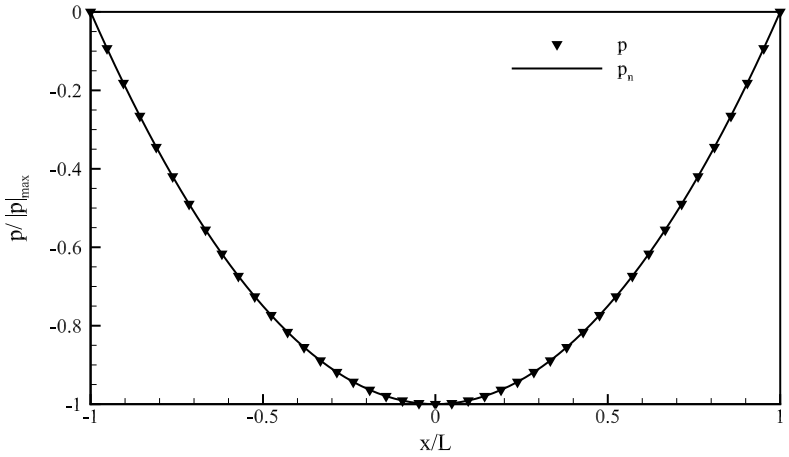

Figure 4.2: The predicted (*symbols*) and exact pressure fields (*line*) on the diagonal.

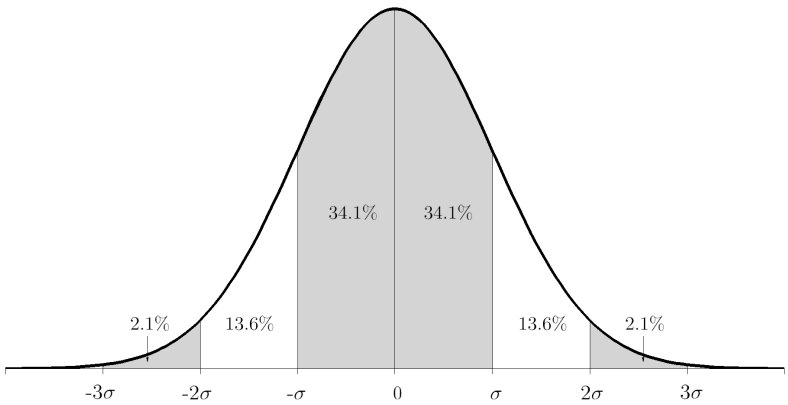

Figure 4.3: Probability density function of Gaussian distribution for zero-mean.

The Gaussian error for both velocity components, ε_u and ε_v, will be introduced to the input velocity data. Mean of the errors are selected as zero to not lead any systematic error. By doing so, the errors are distributed in positive and negative directions equally. The error magnitudes are expressed in non-dimensional form to not reach case-specific conclusions. To non-dimensionalize the error, one may use either root-mean-square or the maximum value of the related parameter. The use of maximum value may lead to non-physical results in case of any outliers in the initial data. On the contrary, use of root-mean-square value will damp the effect of any possible outliers in the initial data. Thus, for non-dimensionalizing the introduced errors, root-mean-square values of the initial velocity components are used. For the $u-$velocity, the

following relationship for root-mean-square value could be written

$$u_{\text{RMS}} = \sqrt{\overline{u}^2 + \sigma_u^2} = \sqrt{\overline{u^2}} = \sqrt{\frac{\sum_{i=1}^{N_x} \sum_{j=1}^{N_y} u^2}{N_x N_y}} \tag{4.3}$$

The magnitude of the introduced velocity errors are given by the percentage of the root-mean-square of the initial velocity data. The normal distribution covers the 99.74% of the samples in $\pm 3\sigma$ range. Thus, this range will be used for defining the error introduced to the initial data, i.e., 5% error in $u-$velocity will be expressed as $3\sigma_{\varepsilon_u} = 0.05\ u_{\text{RMS}}$. In all error analyses in the thesis, errors are introduced for both $u-$ and $v-$velocities. First, it is desired to check if the method is consistent for different sets of random noise. To achieve this, five noise forms in both $u-$ and $v-$velocities are introduced to the rigid-body vortex flow on a 100×100 grid and solved. Distribution of the noise contributions are shown in Figure 4.6 with bars and normal distribution fit on them. The resulting velocity magnitude contours are also shown in the same figure on the far right column. Relative error values of the pressure estimation with different schemes are given in Table 4.1

Table 4.1: Percentage relative error, $\|\varepsilon_p\|_F / \|p_c\|_F$, in the pressure estimation for $3\sigma_{\varepsilon_u} = 0.20\ u_{\text{RMS}}$ and $3\sigma_{\varepsilon_v} = 0.20\ v_{\text{RMS}}$ noise on a 100×100 grid with different schemes

	Case 1	Case 2	Case 3	Case 4	Case 5
Upwind	1.30	1.66	1.32	1.60	1.48
Hybrid	1.38	1.90	1.31	1.80	1.48
Power-law	1.36	1.87	1.30	1.75	1.47
van Leer	1.47	1.65	1.42	1.65	1.54
van Albada	1.50	1.65	1.42	1.66	1.55
Min-Mod	1.46	1.60	1.42	1.63	1.55
SUPERBEE	1.48	1.69	1.44	1.68	1.56
Sweby	1.49	1.69	1.43	1.66	1.55
QUICK	1.47	1.68	1.43	1.65	1.54
UMIST	1.46	1.65	1.41	1.63	1.54

The most significant conclusion that could deduced from Table 4.1 is that all schemes

captures close values as the final pressure estimation. Even if the error introduced is high, the final error is around 2% thanks to the correction process of current methodology. Remaining errors are due to the noise stuck at the outermost cells those behave as boundary conditions of the problem. The reason of having slight deviations in final relative error for different cases is related with distribution of velocity errors at the boundaries. It is seen that in all cases the greatest errors occur for cases 2 and 4, which manifests that the weight of distributed errors on the boundaries are highest for these cases. Moreover, it is seen that the limiter functions of the TVD schemes do not alter the final results significantly as reported in available literature [51].

The estimated and correct pressures are compared in Figure 4.4 for the hybrid scheme solution of case 2 which has the greatest relative error. On the right of the same figure, resulting and correct velocity magnitudes are also compared. The deviations at the boundaries of the estimation zone could be observed. The methodology estimates pressure field accurately in the first iterations; but due to the errors introduced from the boundaries, methodology forces the velocity values to obey governing equations in progressing iterations. Figure 4.5 shows the remaining pressure and velocity error at the end of the iterations. It could be observed that the main source of the remaining errors are due to the noise stuck at the boundaries. Even if 20% error is exaggerated for practical PIV experiments, these figures prove that current methodology is superior for pressure estimation in erroneous velocity data. In case of using Poisson solver for pressure estimation, the velocity errors will not be corrected and an error level at one order of magnitude greater will be observed. Moreover, when the boundary cells are replaced with original smooth velocities, one order of magnitude improvement is observed in the pressure estimation. Thus, one may conclude that the boundary information plays a significant role in the pressure estimation. So, further effort could be paid on enhancing the outermost velocity values such as filtering or starting the estimation with a larger window and reducing it progressively.

The last practice on the error analysis is to investigate the response of current methodology to different magnitudes of noise. To achieve this, noisy velocity fields are employed to the solver with different schemes on a 100×100 grid. Since estimated pressure fields do not differ significantly with different limiter functions, further study is performed only with QUICK scheme of TVD family. The errors are, again, em-

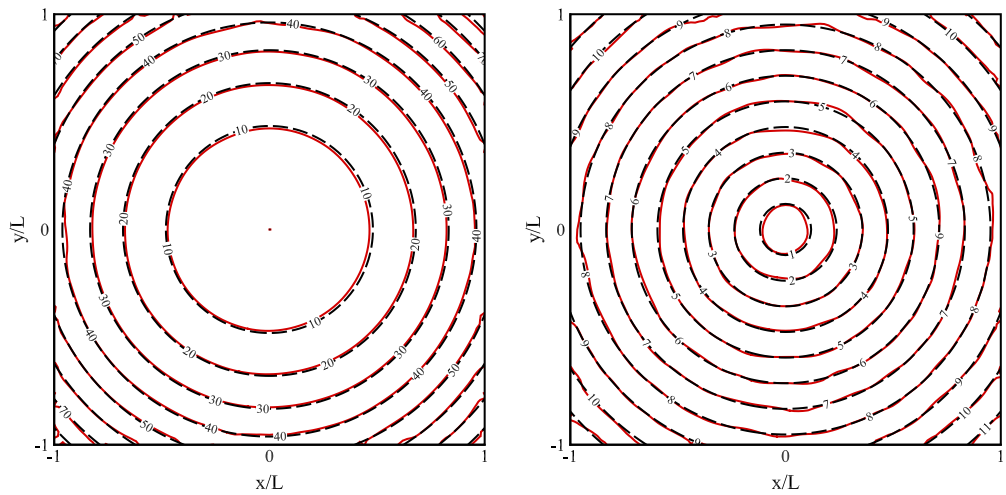

Figure 4.4: Comparison of estimated pressure (*left*) and related velocity magnitude (*right*) with correct values (*dashed lines*) for Case 2 with hybrid scheme.

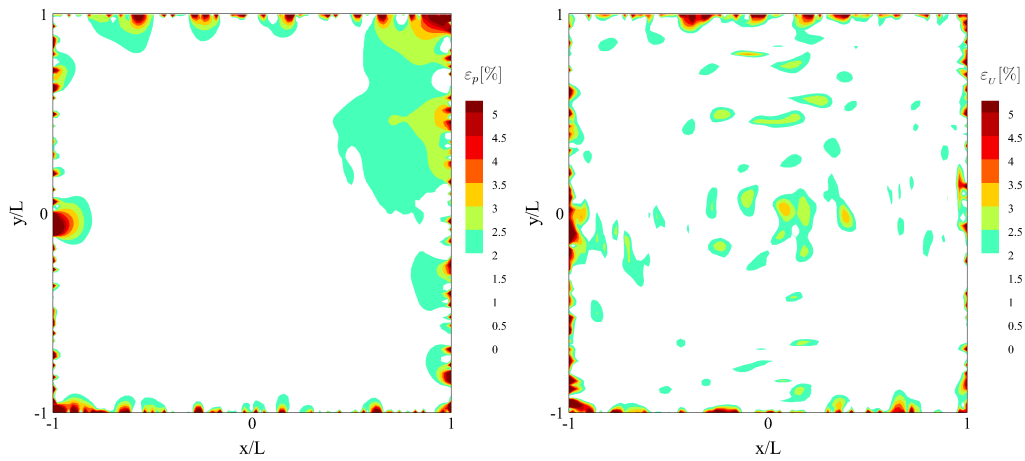

Figure 4.5: Percentage pressure error (*left*) and velocity magnitude error (*right*) contours for Case 2 with hybrid scheme.

ployed on both $u-$ and $v-$velocities where their magnitudes are given as $3\sigma_{\varepsilon_u}/\ u_{\text{RMS}}$ and $3\sigma_{\varepsilon_v}/\ v_{\text{RMS}}$. The relative errors of the pressure estimations with different noise magnitudes are reported in Table 4.2. The same noise distribution is used for all schemes. As expressed in the previous table, there is no significant difference in the final results with different schemes. The maximum error is found to be around 5% even for such high noise in the initial velocities. The errors in final pressure estimation is again related with the noise in outermost cells. Solver estimates correct pressure fields in first iterations and then the velocity field is manipulated to reduce

Table 4.2: Percentage relative error, $\|\varepsilon_p\|_F / \|p_c\|_F$, in pressure estimation for different noise magnitudes on a 100×100 grid.

Noise	Upwind	Hybrid	Power-law	QUICK
2%	0.14	0.15	0.15	0.15
5%	0.38	0.43	0.42	0.40
10%	0.71	0.74	0.73	0.78
15%	0.93	0.96	0.93	1.01
20%	1.22	1.24	1.23	1.34
25%	1.68	1.69	1.68	1.87
30%	2.05	2.03	2.03	2.19
35%	2.38	2.35	2.35	2.53
40%	2.72	2.71	2.70	2.87
45%	2.94	2.88	2.89	3.02
50%	4.50	5.02	4.97	4.61

the imbalance. One obvious trend from the tabulated results is the increase of error in estimated pressure with increasing noise magnitude, as expected. If we consider the normal range of the experimental errors which will not exceed 10%, the error in final pressure estimation is expected to be less than 1% which is fairly acceptable. The procedure is also repeated with a higher number of cells to mimic the window size of the PIV measurements and not a significant change in the final results is observed with number of cells.

Pressure estimation methods based on PPE and spatial integration do not force the input velocity data to obey governing equation through a correction process. Thus, any error in the input velocities will remain there and corrupt final pressure estimation values. Essentially, PPE is an elliptic equation, thus any error in the solution domain will propagate in all directions. This behavior leads to an inevitable progressive rise of total error with iterations in pressure estimation process. Similarly, for the spatial integration process, due to the high number of integrations, the errors will be accumulated. Thanks to the correction capability of current methodology, the pressure estimation errors will be much lower than PPE and spatial integration.

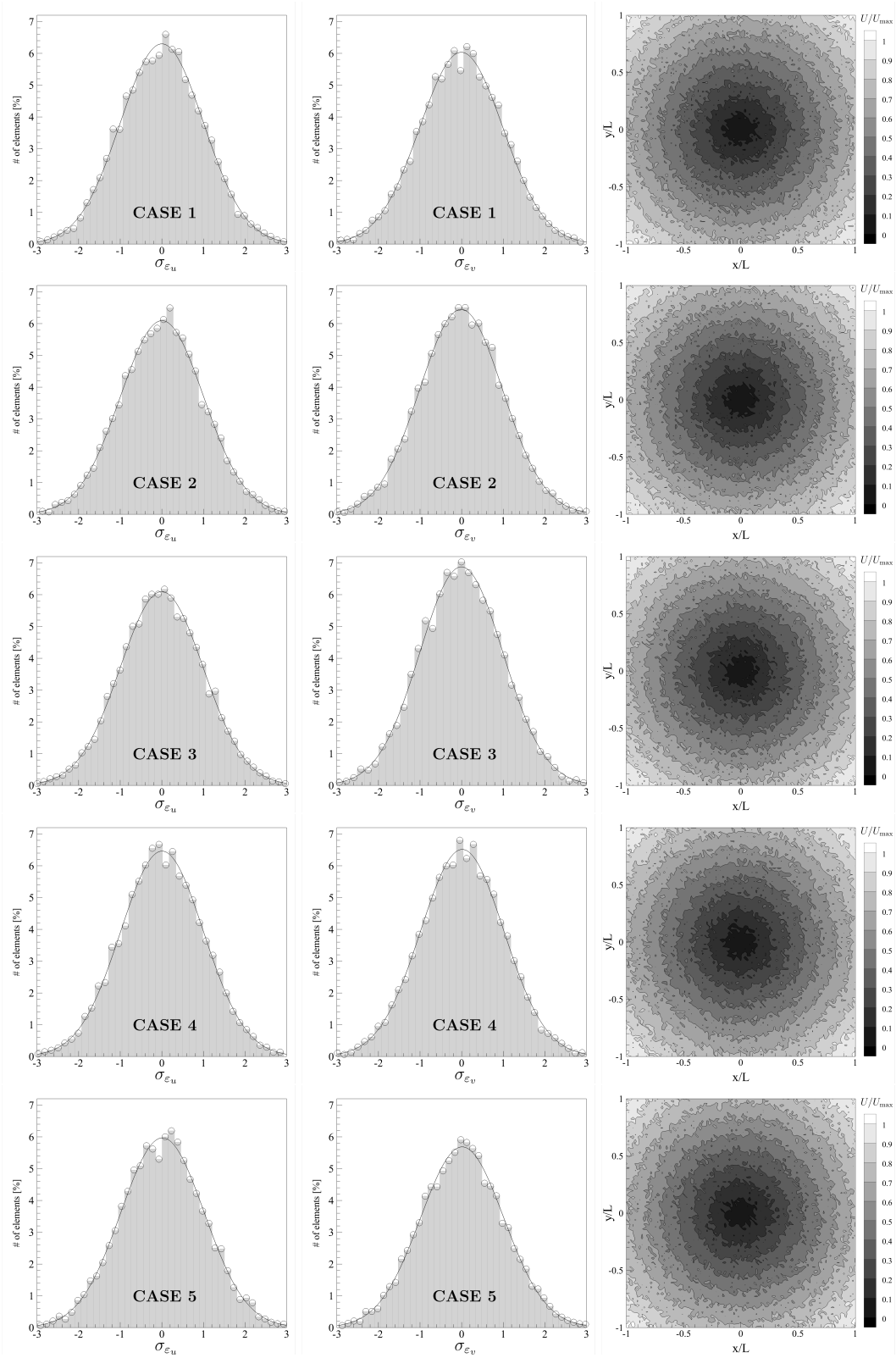

Figure 4.6: Distribution of the Gaussian error on $u-$velocity (*left*) and $v-$velocity (*middle*) components and the resulting velocity contours normalized with maximum value (*right*) for five different cases studied.

4.3 Unsteady Flow

The procedure is also validated for unsteady flows with the available results in the literature. To achieve this, unsteady wake simulation of Kurtuluş [90] for NACA 0012 airfoil at an angle of attack of $30°$ and $Re = 1000$ is used. Figure 4.7 shows the pressure contours of the selected instant and $0.3\ \mathrm{m}\times0.15\ \mathrm{m}$ rectangular region of interest for pressure estimation test. The chord of the airfoil is $c = 0.1\ \mathrm{m}$ and the free-stream velocity is $U_\infty = 0.1461\ \mathrm{m/s}$. The dynamic viscosity and density of working fluid air are $\mu = 1.7894\ \mathrm{Pa\cdot s}$ and $\rho = 1.225\ \mathrm{kg/m^3}$. The vortex shedding frequency is also reported as $0.5\ \mathrm{Hz}$ resulting Strouhal number of $St = 0.342$.

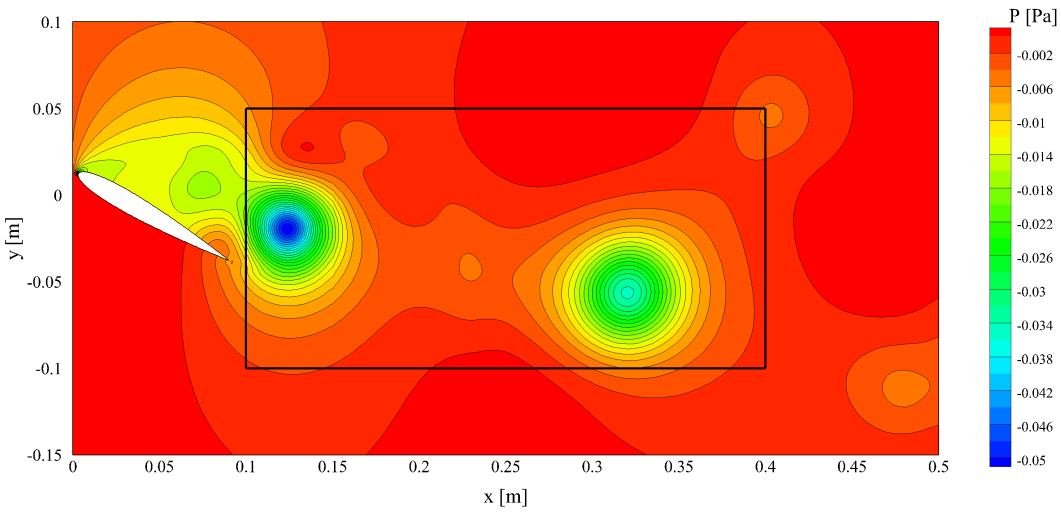

Figure 4.7: Pressure contours of NACA 0012 wake at $Re = 1000$ and AoA = $30°$. Black rectangle shows the region of interest for the unsteady pressure estimation test.

As mentioned in section 3.8, the unsteady pressure estimation procedure demands another velocity field to calculate the unsteady term. To achieve this, we supplement the previous velocity field with $\Delta t = 0.01\ \mathrm{s}$ to the solver with TVD scheme and Sweby limiter on a 300×150 grid that corresponds a vector spacing of $1\ \mathrm{mm}$. The relative error for this case is found to be around 2% in a few iterations. Figure 4.8 shows the comparison of correct and estimated pressures of the case. Greater accuracy is achieved in the regions with high pressure gradients such as the vortex centers. At those high gradient regions, contour lines are overlapping; but while getting away from those regions a slight deviation is observed. Pressure gradient is a strong source

Table 4.3: Percentage relative error, $\|\varepsilon_p\|_F / \|p_c\|_F$, in pressure estimation with different time-step size and grid spacing.

Δt [s]	Δx [mm]						
	1	*1.5*	*2*	*2.5*	*3*	*3.75*	*5*
0.01	2.0	2.3	2.6	3.9	4.0	6.3	8.1
0.02	2.0	2.3	2.7	3.7	4.5	6.9	10.1
0.03	4.0	4.1	4.2	5.7	6.5	8.7	13.0
0.04	7.1	7.0	6.9	8.4	9.4	11.4	16.8
0.05	10.9	10.8	10.8	11.9	13.3	15.2	21.4
0.06	15.3	15.3	15.0	16.2	18.0	19.5	26.7
0.07	20.3	20.4	20.4	21.1	23.4	24.4	32.7
0.08	25.7	26.0	25.5	26.5	29.3	29.7	39.2
0.09	31.5	32.1	31.5	32.3	35.7	35.4	46.1
0.10	37.6	38.2	37.8	38.4	42.3	41.5	53.3

term in the governing equations and when its value is high, it will surpass truncation and numerical errors of the operation. On the contrary, when its value smaller, the various error terms may prevail and show a slight deviation in the results. If needed, for further improvements, different estimations could be applied on separate smaller windows.

It should be also noted that since we are dealing with pressure gradient in governing equations rather than pressure itself, the result will be the differential pressure. To be able to calculate the absolute pressure, the value of absolute pressure at least one point in the flow-field should be known. This could be achieved via simultaneous static pressure measurements in the field of view of PIV measurements or by just having an educated guess of absolute pressure for any point in the field-of-interest. Even if the absolute pressure is not the main aim for most of the fluid mechanics problems, that should be still mentioned for certain studies those require absolute values.

The unsteady pressure estimation methodology is also tested with varying time-step

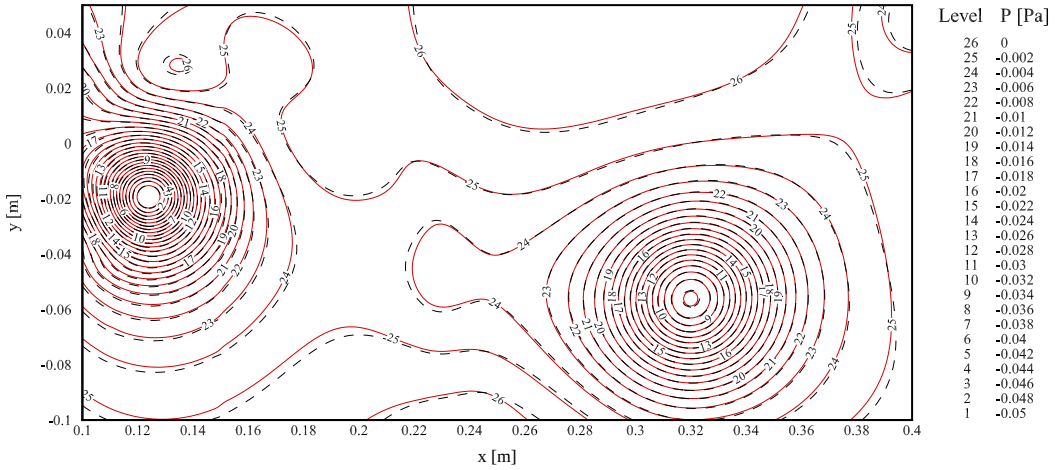

Figure 4.8: Comparison of estimated pressure with correct values (*dashed lines*) on a 300×150 grid with $\Delta t = 0.01$ s.

and grid sizes for the same instant given in Figure 4.7. The resulting percentage relative errors in pressure estimation are summarized in Table 4.3. As it mentioned earlier, the selected region is a 0.3 m$\times 0.15$ m rectangle. To mimic PIV experiments, we choose to have square grid cells. Grid spacings of 5 mm, 3.75 mm, 3 mm, 2.5 mm, 2 mm, 1.5 mm and 1 mm correspond to grids of 60×30, 80×40, 100×50, 150×75, 200×100, and 300×150 elements, respectively.

The procedure implements a fully implicit scheme for temporal discretization, so it is unconditionally stable with respect to time-step. Thus, there is no restriction on time-step. From the tabulated results, it is observed that decreasing time-step and cell size improves the pressure estimation. The error is slightly higher for the coarsest case of 5 mm and reducing the grid size to the next high value (3.75 mm) decreases the error drastically. On the other hand, reducing grid size further, after 2.5 mm, does not improve the solution significantly. From this test, we may conclude that there will be a limit grid spacing in which no further improvement in the final estimation is observed. Reducing the grid size after this limit grid spacing does not introduce any benefits errorwise, only increases the computing time. Similar tendency is also observed for the time-step. Percentage relative error remains nearly constant after $\Delta t = 0.02$ s.

The general conclusion from this section for unsteady flows is to test for the most

suitable grid size by considering the computing resources. In case of no restriction on computing resources, the smallest grid size will give the best estimation errorwise. The time-step is mostly dictated by the acquisition rate of the PIV system and use of the smallest suitable time-step is strongly recommended for any application. As mentioned in section 3.5.3, the convergence criteria of the estimation procedure is the mass imbalance term, given by b'_P in equation 3.126. From the analyses, root-mean-square of the imbalance term found to be most suitable form to monitor. The procedure usually converges in ten to twenty iterations. The relaxation factor defined in 3.7 is a strong tool for convergence of the solution.

CHAPTER 5

RESULTS

The numerical procedure for pressure estimation methodology and its validation are discussed in previous chapters. In this chapter, methodology will be compared with five hole probe results of the flow-field around a two-dimensional cylinder. Then, the procedure will be applied on water tunnel experiment of a flapping NACA 0012 wing from available literature.

5.1 PIV Setup

The experiments are performed in a low-speed open type wind tunnel with maximum flow velocity of $20\ \mathrm{m/s}$ with turbulent intensity around $Tu = 0.5\%$. The closed test section of the wind tunnel has a $0.34\ \mathrm{m}\times0.34\ \mathrm{m}^2$ cross-section with a length of $1\ \mathrm{m}$. The model is an end-to-end circular cylinder with a diameter of $0.0635\ \mathrm{mm}$. There is a static port on the cylinder model surface which is used as a reference point in the five hole probe measurements. The images are acquired with Phantom v640 camera with 4-megapixels resolution and flow is illuminated with New Wave Solo PIV 120 Nd:YAG laser with an output energy of 120 mJ. For seeding, TSI oil droplet generator model 9307-6 is used. The six jet Laskin nozzle pressurizes the olive oil and generates seed particles with the size of 1 $\mu\mathrm{m}$. The image pairs are acquired at $20\ \mathrm{Hz}$ and mean flow-fields are achieved by averaging 2000 vector fields. The acquired images are processed with Dantec DynamicStudio 5.1 software with adaptive cross-correlations starting from 64×64 pixel windows to 32×32 pixels with 50% overlapping. The field-of-view is 127×79 mm^2 (2.00D×1.24D) which results a vector spacing around 0.8 mm. The time between two laser pulses is selected as 20 $\mu\mathrm{s}$.

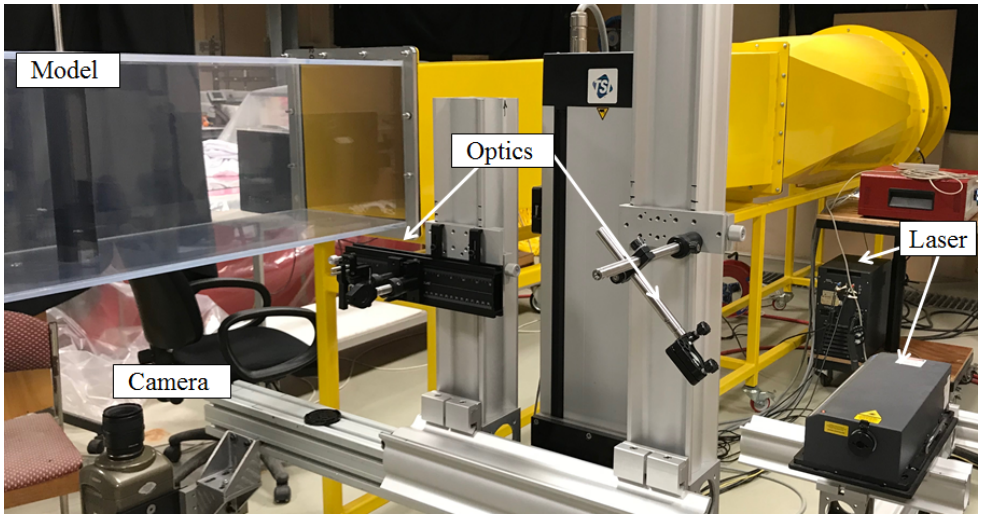

Figure 5.1: PIV setup with laser, optical arrangement, camera and the cylinder model in the test section.

5.2 Five Hole Probe Measurements

To experimentally validate the results, five hole probe measurements are conducted at the similar flow conditions at a different time than the PIV experiments. It is significant to note that with these sets of experiments, an intrusive measurement technique is being compared with a non-intrusive one. Even if the close conditions are seeked to be matched, these set of experiments are not conducted simultaneously, which may lead differences in the results. The schematic of the five hole probe is given in Figure 5.3. The five hole probe is a sub-miniature probe, with a head diameter of D_{FHP} =1.8 mm, designed for turbo-machinery flows. The operational velocities for turbo-machinery flows (30 m/s) are much higher than the maximum velocities of the current experimental campaign (10 m/s). The Reynolds numbers based on head diameter in these set of experiments found to be in the range of $Re_{D_{\text{FHP}}} = 1000$ which corresponds to highly viscous flow around the probe nose. Thus, a detailed calibration procedure is followed for the current five hole probe.

5.2.1 Calibration of Five Hole Probe

The calibration procedure of a five hole probe follows to calculate the calibration coefficients in a well characterized flow. To achieve this, an available calibration setup, shown in Figure 5.2, is used. In this setup, the flow is sustained by DANTEC 54H10 Hot-wire Calibrator which provides a jet with a low turbulence intensity around $Tu \sim 0.6\%$. Two rotary tables from Velmex Inc. with model B4800TS supports the rotation of the probe around pitch and yaw axes with a precision of $0.00653°$ per step.

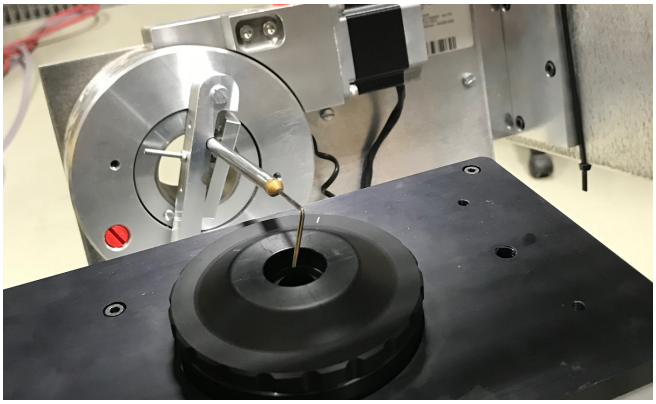

Figure 5.2: Close up view of the five hole probe in calibration jet.

The non-nulling calibration procedure of Treaster and Yocum [91] is used for different Reynolds numbers. The procedure follows to rotate the probe in a well-characterized flow to achieve the pressure coefficients in a certain pitch and yaw angle range. Then, these coefficients are gathered to create a carpet map for estimation of pitch and yaw angles for the use of five hole probe in an unknown flow. To record the pressure data 16-bit Scanivalve DSA 3217 differential pressure transducer with the range of 10 inches H_2O, which has a pressure increment around 0.145 Pa, is used. The schematic of the five hole probe is given in Figure 5.3. The positive pitch angle is defined for the flow coming from above to the probe, higher values at port 5 when probe is facing the incoming flow. The positive yaw angle is defined for the flow coming from left to the probe - higher pressure at port 2. This notation gives positive yaw and pitch coefficients for positive yaw and pitch angles. The coefficients of the calibration are given as

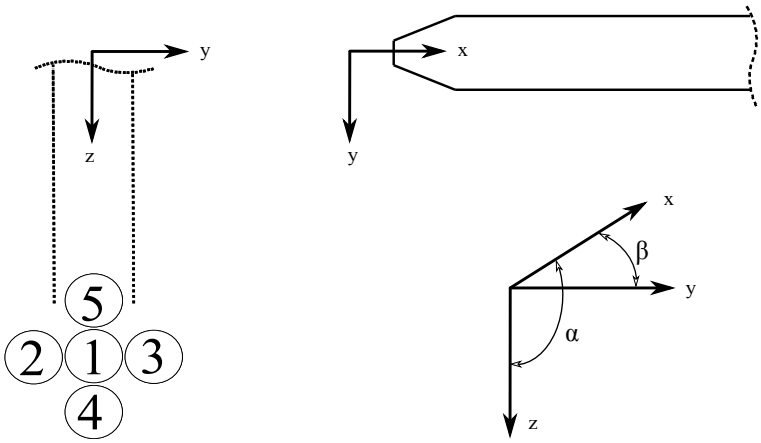

Figure 5.3: Schematic of the five hole probe and the related nomenclature. Front view (*left*) and the top view (*right*) of the five hole probe.

$$C_{P,pitch} = \frac{P_5 - P_4}{P_1 - \overline{P}} \tag{5.1a}$$

$$C_{P,yaw} = \frac{P_2 - P_3}{P_1 - \overline{P}} \tag{5.1b}$$

$$C_{P,static} = \frac{\overline{P} - P_{static}}{P_1 - \overline{P}} \tag{5.1c}$$

$$C_{P,total} = \frac{P_1 - P_{total}}{P_1 - \overline{P}} \tag{5.1d}$$

where the average pressure, $\overline{P}$, is

$$\overline{P} = \frac{P_2 + P_3 + P_4 + P_5}{4} \tag{5.2}$$

In addition to the pressure at five holes, during the calibration total and static pressures are also recorded simultaneously. The jet is open to the atmosphere, so the static pressure in equation 5.1c becomes atmospheric pressure. The denominator in the above pressure coefficient definitions mimics the dynamic pressure with available measured pressure values. To get the mean of each pressure measurement, 2000 samples are acquired with a frequency of 30 Hz. Through the measurement of mean pressure values, the calibration map is generated for pitch and yaw angles of $\pm 20°$

with increments of 4° resulting a 11×11 grid. The classical approach of Treaster and Yocum [91] follows calibrating at one Reynolds number and using it for experiments at different Reynolds numbers. Here, since the Reynolds number based on probe head diameter ($Re_{D_{FHP}}$) is small, we calibrated the probe at four different Reynolds numbers those are matching with the conditions of PIV measurements. Polynomials are fitted to the acquired calibration maps with relatively high adjusted R^2 values to process data digitally. R^2 is 0.985 for static pressure map and 0.999 for remaining parameters. One other benefit of creating a calibration map database could be interpolating the polynomial fits of pressure coefficients to the matching Reynolds number of the experiment [92]. Since the calibrations are conducted at the exact PIV experimental conditions, interpolation of calibration maps for matching Reynolds number is not required for this study.

The carpet plot of $10\ \mathrm{m/s}$ free-stream is given in Figure 5.4. After calculating the pressure coefficients given by equation 5.1, the corresponding pitch and yaw angles of the flow are estimated from Figure 5.4. Knowing these angles, the related total and static pressure coefficients will be estimated from Figures 5.5 and 5.6. Then the total pressure, static pressure and the velocity magnitude could be calculated from

$$P_T = P_1 - C_{P,total}(P_1 - \overline{P}) \tag{5.3a}$$

$$P_S = \overline{P} - C_{P,static}(P_1 - \overline{P}) \tag{5.3b}$$

$$V = \sqrt{\frac{2(P_T - P_S)}{\rho}} \tag{5.3c}$$

where the velocity components are given by

$$u = V \cos\alpha \cos\beta \tag{5.4a}$$

$$v = V \sin\beta \tag{5.4b}$$

$$w = V \sin\alpha \cos\beta \tag{5.4c}$$

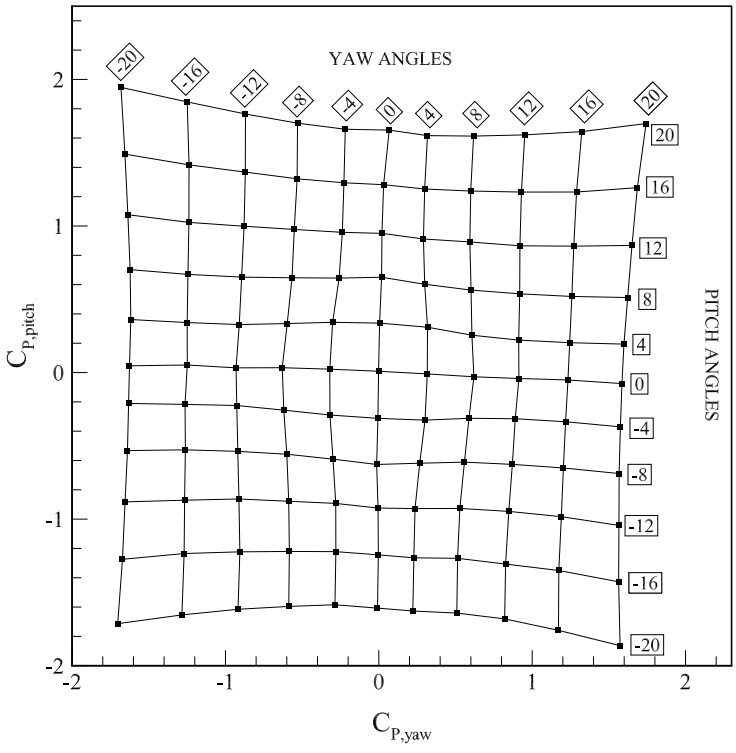

Figure 5.4: Variation of pitch and yaw coefficients at constant angles.

Lowest adjusted R^2 of the numerical fits are acquired for static pressure coefficient, which is still a high value by being 0.985. Comparison of the fitted and exact static pressure coefficients with pitch and yaw angles are given in Figures 5.6 and 5.7. As it could be seen from these figures, the polynomial fit smoothens the small discontinuities in the static pressure coefficient variation which may be due to small uncertainties in the calibration process. Polynomial fits for remaining parameters have R^2 values of 0.999. All fits for the variables are given in the following form of fifth order polynomial with 21 coefficients:

$$\begin{aligned} f(\alpha,\beta) = {} & p_{00} + p_{10}\alpha + p_{01}\beta + p_{20}\alpha^2 + p_{11}\alpha\beta + p_{02}\beta^2 + p_{30}\alpha^3 + p_{21}\alpha^2\beta + \\ & p_{12}\alpha\beta^2 + p_{03}\beta^3 + p_{40}\alpha^4 + p_{31}\alpha^3\beta + p_{22}\alpha^2\beta^2 + p_{13}\alpha\beta^3 + p_{04}y^4 + \\ & p_{50}\alpha^5 + p_{41}\alpha^4\beta + p_{32}\alpha^3\beta^2 + p_{23}\alpha^2\beta^3 + p_{14}\alpha\beta^4 + p_{05}\beta^5 \end{aligned} \tag{5.5}$$

The same calibration process is also followed for free-stream velocities of $4\ \mathrm{m/s}$,

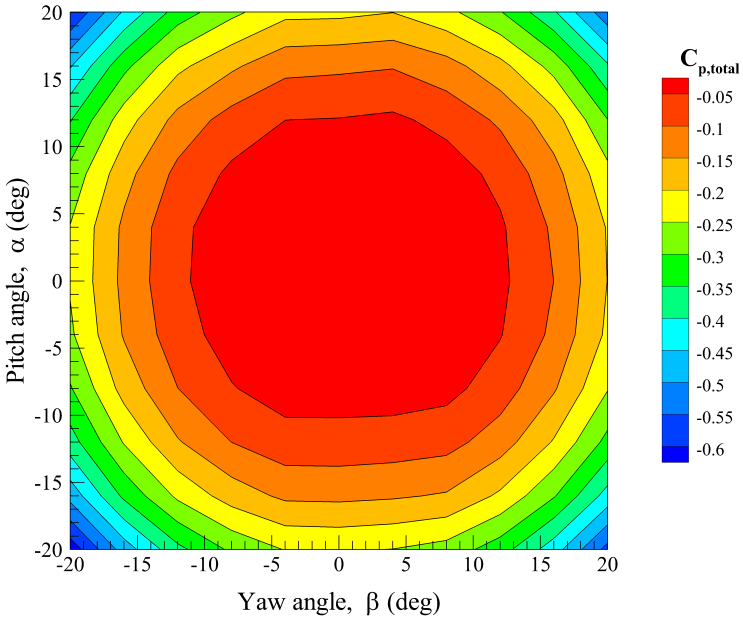

Figure 5.5: Variation of total pressure coefficient with pitch and yaw angles.

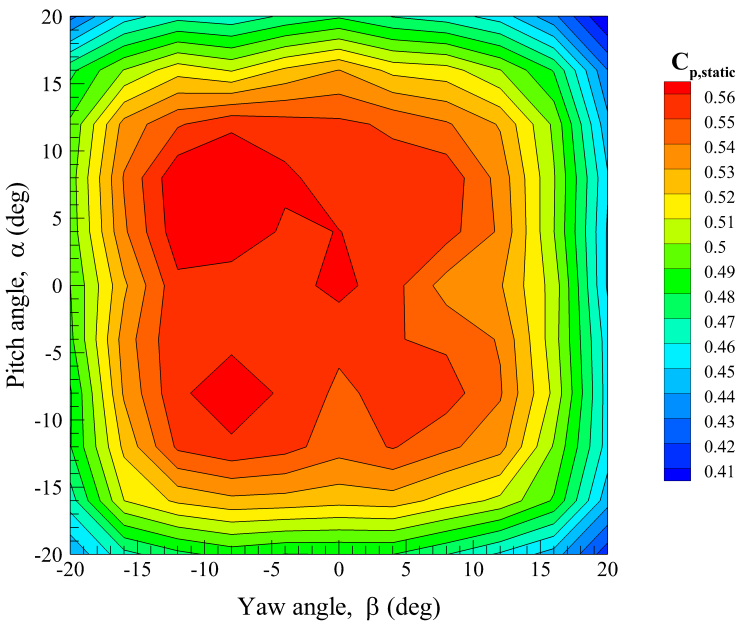

Figure 5.6: Variation of static pressure coefficient with pitch and yaw angles

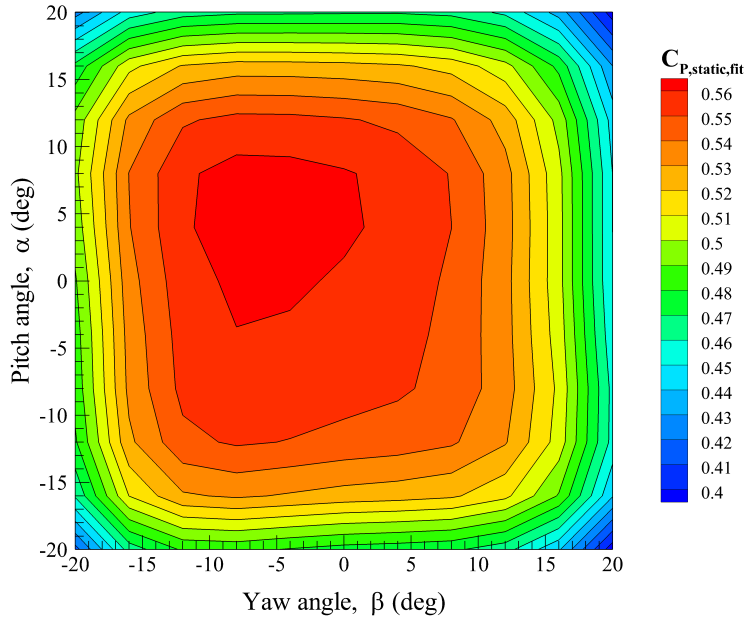

Figure 5.7: Variation of static pressure coefficient for the fitted model with pitch and yaw angles.

$6\ \mathrm{m/s}$, $8\ \mathrm{m/s}$ and $12\ \mathrm{m/s}$; but results are not repeated here for brevity.

5.2.2 Uncertainty Analysis

Uncertainties for total pressure, static pressure and velocity magnitude are also calculated. The total pressure is calculated form equation 5.3a, where the variables affecting the total pressure are all pressures from five ports and the calculated $C_{P,total}$. Then, the uncertainty of total pressure is defined as

$$\delta P_T = \left[\left(\delta P_1 \frac{\delta P_T}{\delta P_1}\right)^2 + \left(\delta P_2 \frac{\delta P_T}{\delta P_2}\right)^2 + \left(\delta P_3 \frac{\delta P_T}{\delta P_3}\right)^2 + \left(\delta P_4 \frac{\delta P_T}{\delta P_4}\right)^2 + \left(\delta P_5 \frac{\delta P_T}{\delta P_5}\right)^2 + \left(\delta C_{P,total} \frac{\delta P_T}{\delta C_{P,total}}\right)^2 \right]^{1/2} \tag{5.6}$$

The accuracy of pressure values measured from the transducer is given as $\pm 0.2\%$ of the full scale range of 10 inches of H_2O that corresponds to $\delta P = 5\ \mathrm{Pa}$. Consid-

ering the effect of measurement chain, uncertainty of the pressure measurements is estimated to be $\delta P = 6$ Pa for all ports. To estimate the uncertainty of total pressure coefficient, we used the standard deviation of the $C_{P,total}$ values shown in Figure 5.5. Then, uncertainty of total pressure measurements is given by Figure 5.8

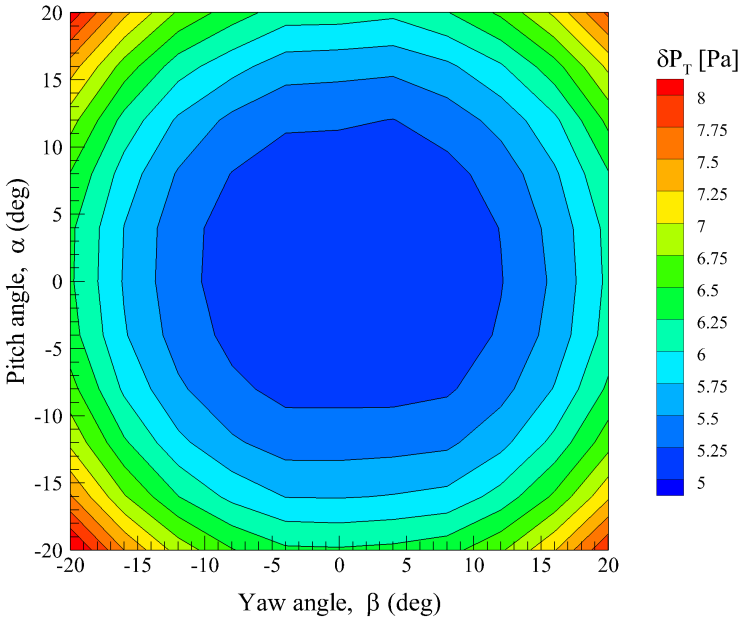

Figure 5.8: Variation of total pressure uncertainty at $10\ \mathrm{m/s}$.

Similarly, the uncertainty of static pressure measurements is calculated from,

$$\delta P_S = \left[\left(\delta P_1 \frac{\delta P_S}{\delta P_1} \right)^2 + \left(\delta P_2 \frac{\delta P_S}{\delta P_2} \right)^2 + \left(\delta P_3 \frac{\delta P_S}{\delta P_3} \right)^2 + \left(\delta P_4 \frac{\delta P_S}{\delta P_4} \right)^2 + \left(\delta P_5 \frac{\delta P_S}{\delta P_5} \right)^2 + \left(\delta C_{P,static} \frac{\delta P_S}{\delta C_{P,static}} \right)^2 \right]^{1/2} \tag{5.7}$$

and by following the same practice as total pressure, uncertainty of static pressure measurements are calculated as shown in Figure 5.9.

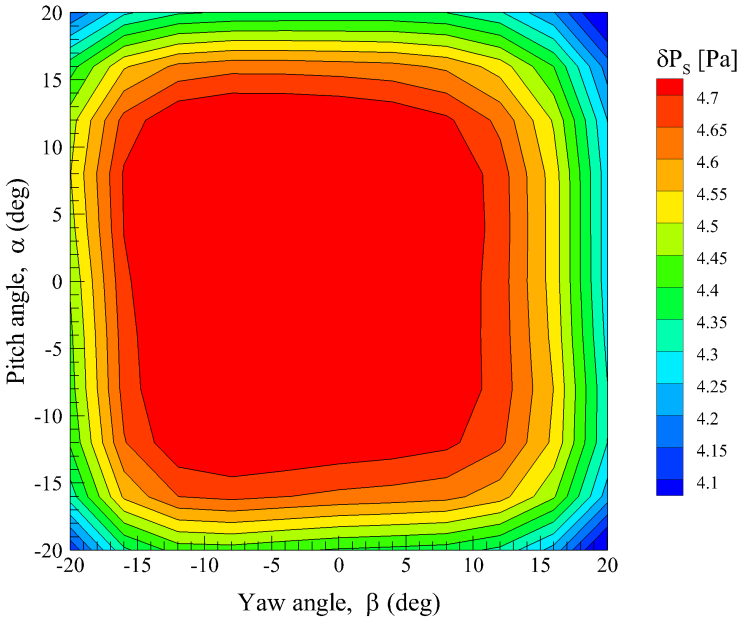

Figure 5.9: Variation of static pressure uncertainty at $10\ \mathrm{m/s}$.

The uncertainty of velocity magnitude is calculated from

$$\delta V = \left[\left(\delta P_T \frac{\delta V}{\delta P_T} \right)^2 + \left(\delta P_S \frac{\delta V}{\delta P_S} \right)^2 + \left(\delta \rho \frac{\delta V}{\delta \rho} \right)^2 \right]^{1/2} \tag{5.8}$$

The density is calculated from measured temperature, relative humidity and ambient pressure with one significant digit accuracy. Thus, uncertainty of density is estimated to be negligible. The uncertainties of total and static pressures, δP_T and δP_S, are already calculated with respect to pitch and yaw angles.

Even if the velocity measurement is not the main point of interest for this study, we still use these values to quantitatively compare the flow-fields of PIV experiments with FHP measurements. The variation of velocity magnitude uncertainties for flow at $10\ \mathrm{m/s}$ is shown in Figure 5.10. As it could be seen, the maximum error within the pitch and yaw angle range of $\pm 20°$ is estimated to be around 2%.

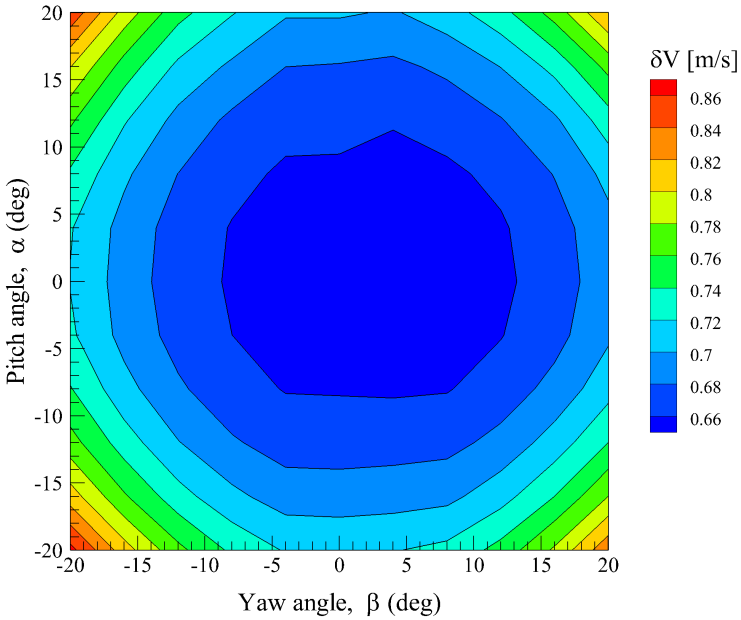

Figure 5.10: Variation of velocity uncertainty with pitch and yaw angles at $10\ \mathrm{m/s}$.

5.3 Comparison with Five Hole Probe Measurements

The purpose of this chapter is to compare the estimated pressure from PIV measurements with a conventional pressure measurement tool. The pressure estimation from PIV is a non-intrusive, omnidirectional measurement technique. The most suitable comparison could be achieved with omnidirectional pressure probes which generally have greater number of holes, 12-,17-,18-holes [93–95], than the conventional five- or seven-hole probes. Nonetheless, we used five hole probe measurements by considering the possible sources of errors. The PIV and five hole probe measurements are not conducted simultaneously, but special attention is paid to keep the similar conditions for both experimental campaigns. Despite all efforts, the experimental conditions may still vary slightly. The flow of interest for the comparison is the mean flow around an end-to-end two dimensional circular cylinder at $Re = 36000$. The flow-field achieved by averaging of 2000 instantaneous vector fields is shown in Figure 5.11 in terms of mean velocity field and streamlines. Low acquisition frequencies of PIV and FHP experiments, $20\ \mathrm{Hz}$ and $30\ \mathrm{Hz}$, limit further analysis on temporal statistics. So the main aim here would be evaluating the applicability of the current

pressure estimation methodology in terms of mean flow characteristics.

To compare the results of pressure estimation with five hole probe measurements, the region with dashed black lines shown in Figure 5.12 is chosen. The u and v components of the velocity acquired from PIV are employed to the solver with TVD schemes. It is observed that for this case, order of the discretization schemes are not differing in terms of final estimated pressure results. Five hole probe is a directional measurement tool which will limit us for measuring the pressure at the wake of the cylinder where reverse flow dominates. Thus, we find the most suitable location as the white lines shown in Figure 5.12 for which the vertical positions are given in Table 5.1. To traverse the probe inside the closed test section, a small channel on the upper surface of the test section is prepared. The channel is covered with a thin (2 mm) rectangular acrylic cover to avoid any suction from outside. The lightweight cover travels with the five hole probe without generating any significant vibration. Performance of the cover is checked through out-of-plane component of velocity. As is it shown in Figure 5.17, the out-of-plane component of velocity is found to be two order of magnitude lower than the free stream velocity, which also proves the two-dimensionality of the flow-field.

As seen in Figure 5.12, further downstream lines will experience a greater flow unsteadiness due to vortex shedding. Even the mean flow seems to be stay within the limits of calibration, the instantaneous velocity field exceeds these limits. Thus, the comparison will not be ideal further downstream due to the different flow measuring capabilities. It is also noteworthy that the aim here is not to validate the pressure estimation methodology. To validate the method, exact solutions of Navier-Stokes equations are already used in previous chapter. This part is devoted to evaluate the weaknesses and strengths of these two methodologies.

In pressure estimation from PIV, since one deals with pressure gradients, the result will be given as differential pressures, not as absolute pressures. Even though differential pressure is adequate for most of the fluid flow problems, one may supply the absolute pressure at a certain point in the flow-field to achieve absolute pressures at all points. During five hole probe measurement campaign, we used the pressure tapping on the cylinder to estimate the absolute pressure at one point on the flow-field.

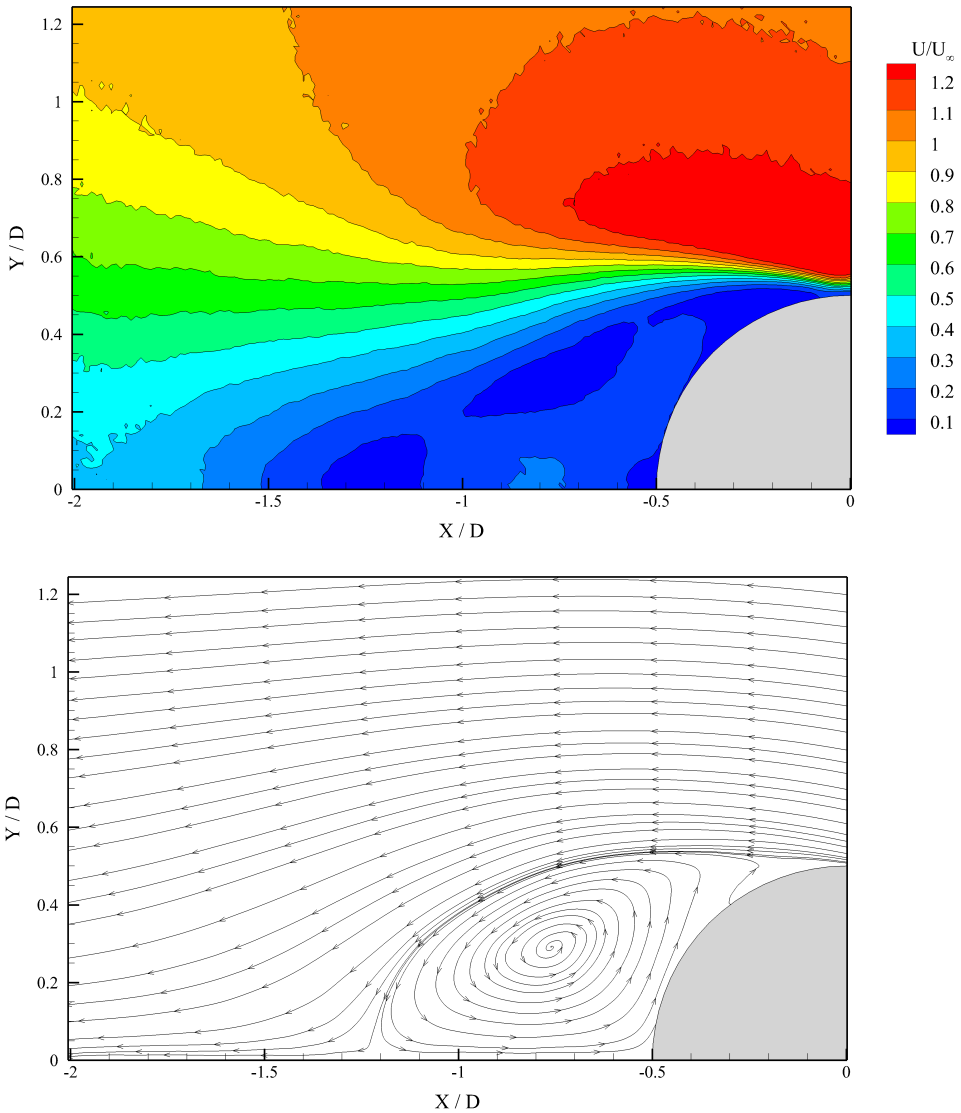

Figure 5.11: Velocity magnitude variation (*top*) and the streamlines (*bottom*) for the mean flow around the two-dimensional cylinder at Re= 36000 from planar PIV measurements.

The pressure tap is set to 90° of the cylinder, which corresponds to the point $(0, D/2)$ in Figure 5.12. This pressure value is set to the lower right corner of the region of interest for pressure estimation as seen in the same figure. Since there is a small gap between the pressure tapping and the corner of the pressure estimation zone, there may occur a slight shift of the estimated pressure values all together with the same magnitude.

Figure 5.13 shows the measured pressure from five hole probe with estimated pressure

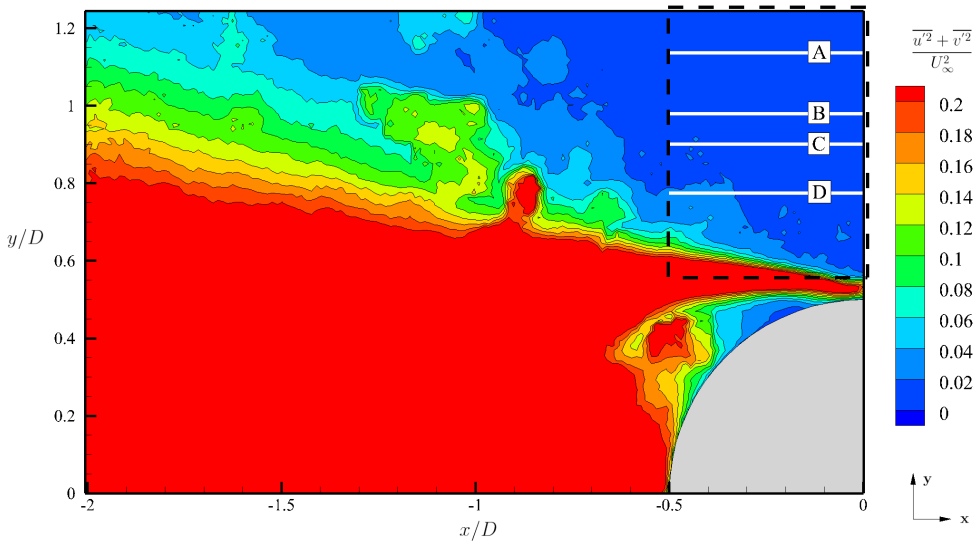

Figure 5.12: The region of interest for pressure estimation (*dashed black lines*) and the lines of five-hole probe measurements (*white lines*) on the RMS field contour of mean flow around the two-dimensional cylinder at Re= 36000 from planar PIV measurements.

Table 5.1: Vertical position of the five hole probe measurements

Line	y/D	y [mm]
A	1.14	73
B	0.98	63
C	0.90	58
D	0.77	50

values from PIV along prescribed lines. First, the methods that are being compared are different in terms of their nature as five hole probe being intrusive and altering the flow-field. As a result, we will not be comparing the same flow-fields. The most suitable comparison between these sets of experiments could be evaluating the trend of each method within itself. The pressure differences for both cases between the upper and lower lines is found to be around 15 Pa for both measurements. The location of the minimum pressure seems to be shifted in five hole probe measurements. Both of these pressure data could be seen together in Figure 5.15. The five hole probe data extends to the leading edge of the cylinder and this data is also included in this

figure. It is seen that while we are getting close to the cylinder with the probe, from line A to line D, difference in pressure values is increasing. This difference could be related with the greater interaction of five hole probe with the cylinder, thus a greater blockage effect. As one can observe, this difference is minimum at the furthest point from the cylinder (line A) and maximum at the closest point (line D). Furthermore, if the extended pressure data from FHP measurements are analyzed, even if no PIV data exists for the upstream, the general trend of convergence of the pressures from two sources could be observed. The reason of the overlapping is to have a less turbulent, more steady flow at the upstream which is more suitable for the main principle of five hole probe measurements. This figure could be also interpreted as the comparison of an intrusive method with a non-intrusive one.

The streamwise and lateral velocities of both measurements are shown in Figures 5.14 and 5.16. Both velocities are found to be close to each other but velocities are slightly larger in PIV experiments than five hole probe measurements.

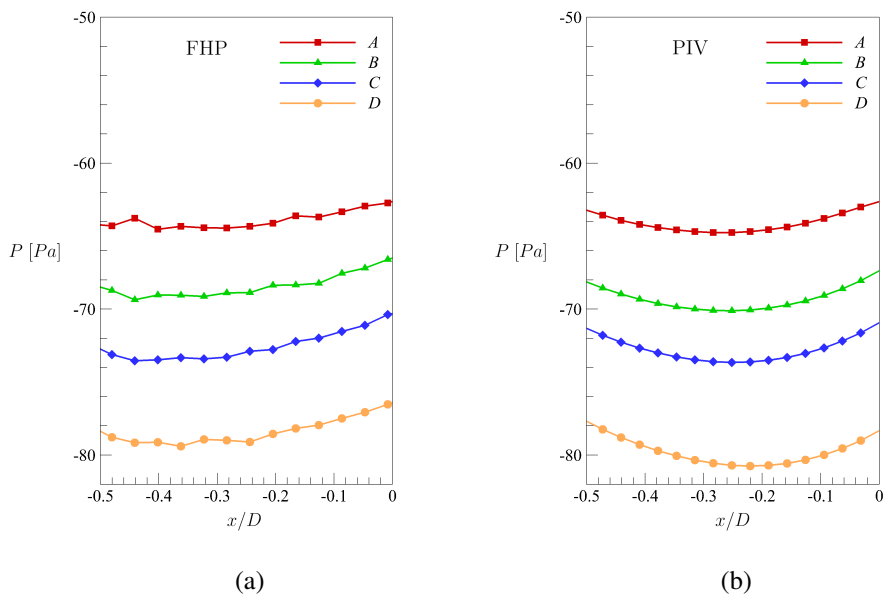

Figure 5.13: Pressure values (*a*) measured from five hole probe measurements and (*b*) estimated from PIV measurements along the prescribed lines at similar conditions.

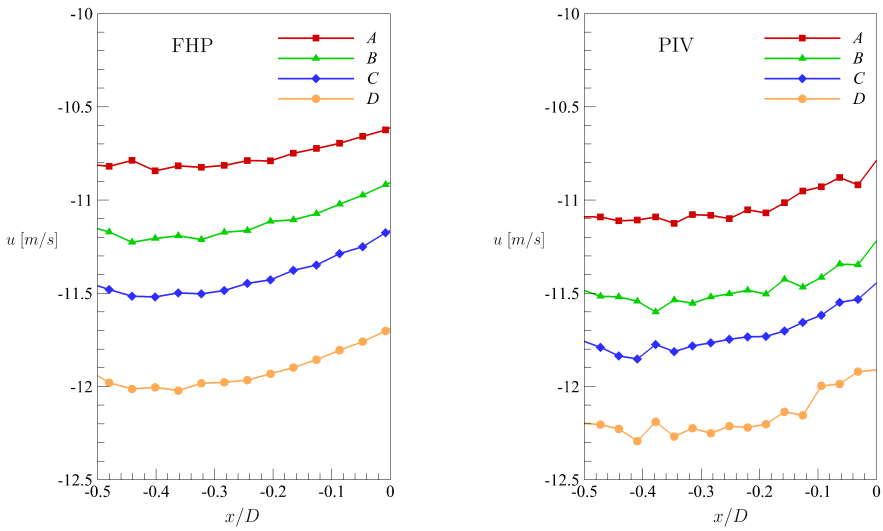

(a) (b)

Figure 5.14: Streamwise velocity component from (*a*) five hole probe measurements and from (*b*) PIV measurements along the prescribed lines at similar conditions.

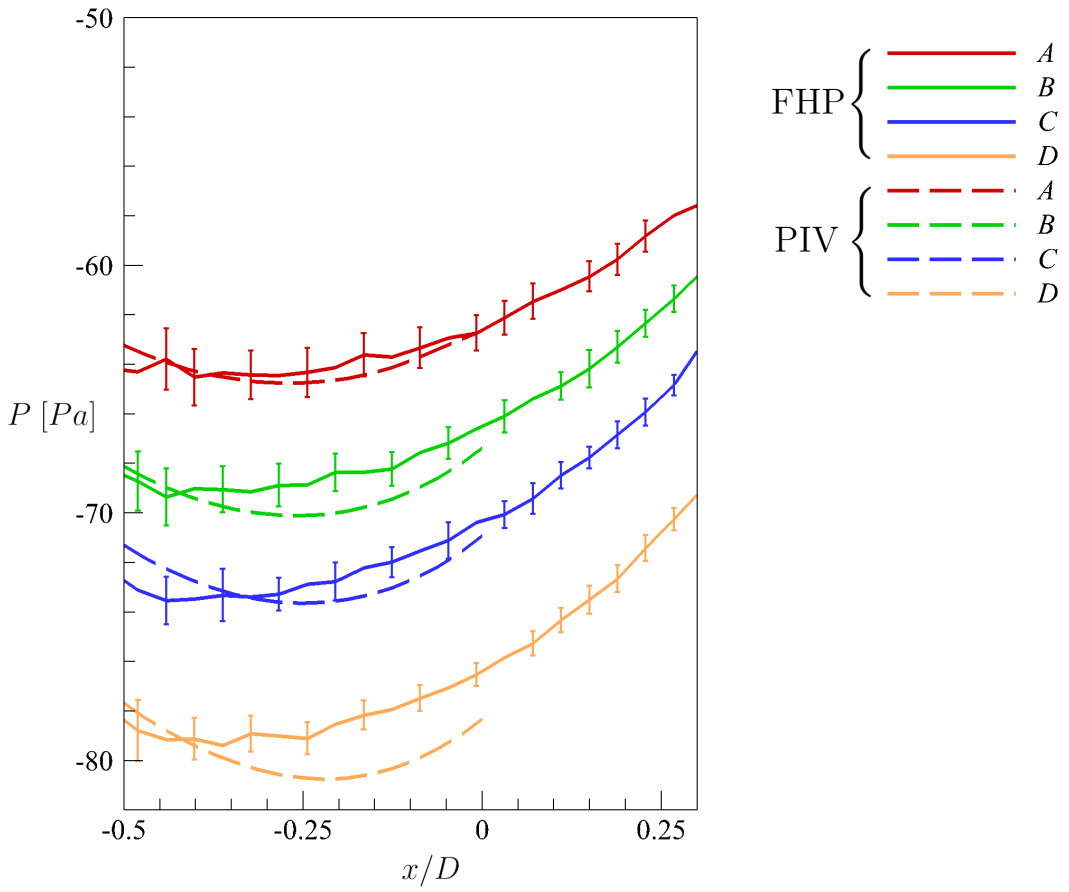

Figure 5.15: Extended data for pressure values measured from five hole probe and estimated from PIV measurements.

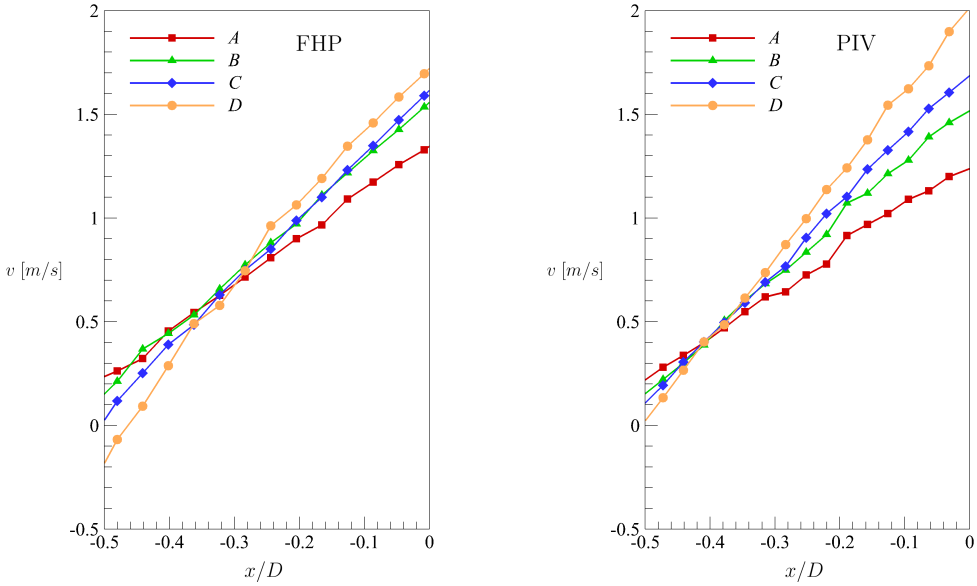

(a) (b)

Figure 5.16: Lateral velocity component for (*a*) five hole probe measurements and (*b*) PIV measurements along the prescribed lines at similar conditions.

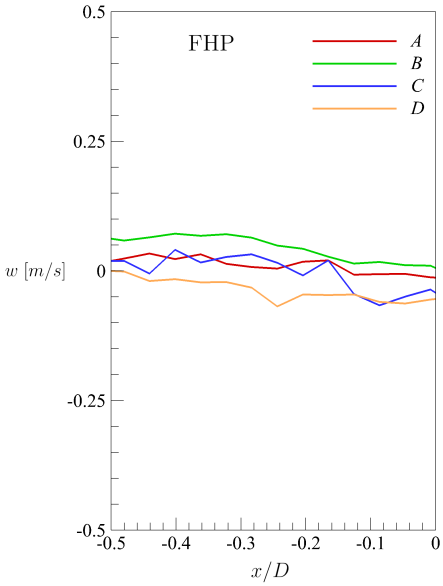

Figure 5.17: Out-of-plane component of the velocity measured by five hole probe along the prescribed lines.

5.4 Application on a Flapping NACA 0012 Airfoil

The methodology is applied on the PIV measurements of a flapping NACA 0012 airfoil by Kurtuluş [96]. Before discussing the results of pressure estimations on the flapping airfoil, the Q-criterion of Hunt *et al.* [97] that used for identification of the vortices will be explained. The Q-criterion primarily depends on the invariants of velocity gradient tensor. The velocity gradient tensor $u_{i,j}$ could be decomposed into a symmetrical rate-of-strain tensor, $S_{ij} = \frac{1}{2}\left(u_{i,j} + u_{j,i}\right)$, and skew-symmetric rotation tensor, $\Omega_{ij} = \frac{1}{2}\left(u_{i,j} - u_{j,i}\right)$, for incompressible flows where subscript comma denotes differentiation. Then the characteristic equation of velocity gradient tensor for the eigenvalues λ is given by

$$\lambda^3 + P\lambda^2 + Q\lambda + R = 0 \tag{5.9}$$

where P, Q and R are the first, second and third invariants of the velocity gradient tensor, respectively. The invariants of velocity gradient tensor are defined as

$$P = -\, u_{i,i} = 0 \tag{5.10a}$$

$$Q = \frac{1}{2}\left(u_{i,i}^2 - u_{i,j}u_{j,i}\right) = -\frac{1}{2}u_{i,j}u_{j,i} \tag{5.10b}$$

$$R = -\, det(u_{i,j}) \tag{5.10c}$$

Hunt *et al.* [97] propose to use the positive second invariant of the velocity gradient tensor, Q, to identify the vortices in incompressible flows. The second invariant could also be written as $\frac{1}{2}\left(\|\Omega_{ij}\|^2 - \|S_{ij}\|^2\right)$ which states that the regions where vorticity prevails the strain rate are vortex locations. One constraint for this methodology is to have lower pressure at the vortex core than the ambient which is not contradicting with the present methodology. The Q-criterion for two-dimensional flows could be written as

$$Q = -\frac{1}{2}\left[\left(\frac{\delta u}{\delta x}\right)^2 + \frac{\delta u}{\delta y}\frac{\delta v}{\delta x} + \left(\frac{\delta v}{\delta y}\right)^2\right] > 0 \tag{5.11}$$

5.4.1 Pressure Estimation on Flapping NACA 0012 Airfoil

The flapping airfoils are generating strong vortices in laminar range, thus stands as appropriate candidate for testing the present method. Pressure is estimated for planar PIV measurements of flapping NACA 0012 airfoil at $Re = 1000$ by Kurtuluş [96]. The working fluid is water with density of $1000\ \mathrm{kg/m^3}$ and dynamic viscosity of $0.001\ \mathrm{Pa \cdot s}$ where airfoil chord is $c = 0.06\ \mathrm{mm}$.

The airfoil undergoes combined translational and rotational motion along a $6c$ span. The motion is defined by the given angular position and translational velocity histories in Figure 5.18 for one period. The airfoil translates with constant velocity, $V_0 = 16.66\ \mathrm{mm/s}$, and angle of attack, $\alpha = 45°$, in the range of $[c, 5c]$. At other regions airfoil undergoes sinusoidal rotation and acceleration/deceleration. The details of the flapping motion and PIV experiments could be found in References [96] and [98].

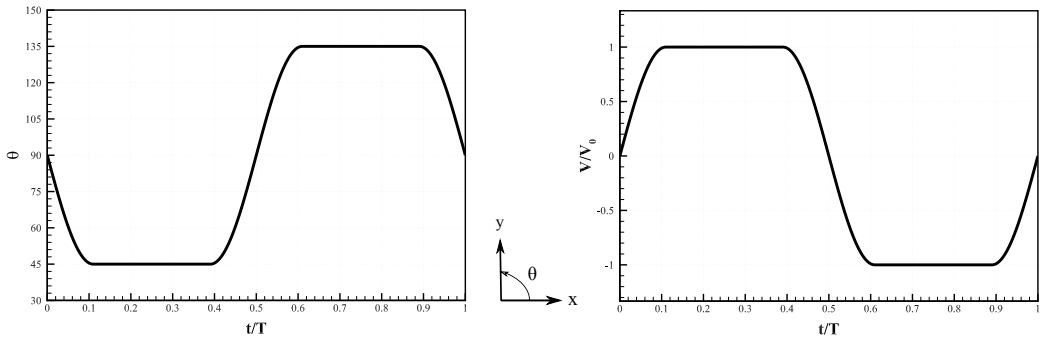

Figure 5.18: Angular position (*left*) and translational velocity (*right*) variations of the airfoil in a period.

Pressure is estimated on the flapping airfoil case at the beginning of stroke $t/T = 0.0132$ in which translational velocity is $V/V_0 = 0.1869$ and the angular position is $\theta = 79.35°$ with respect to the coordinate system shown in Figure 5.18. Figure 5.19 shows the non-dimensional vorticity distribution along on the total $6c$ span airfoil moves. The swirly region with thick borders is used for pressure estimation. The velocity fields at this region are inputs for the solver in addition to the density and viscosity of the working fluid water. In Chapter 4, it is concluded that smallest possible time-step and grid spacing should be used to get least erroneous pressure estimation. For current study, the time-step is already limited by the experimental arrangement to

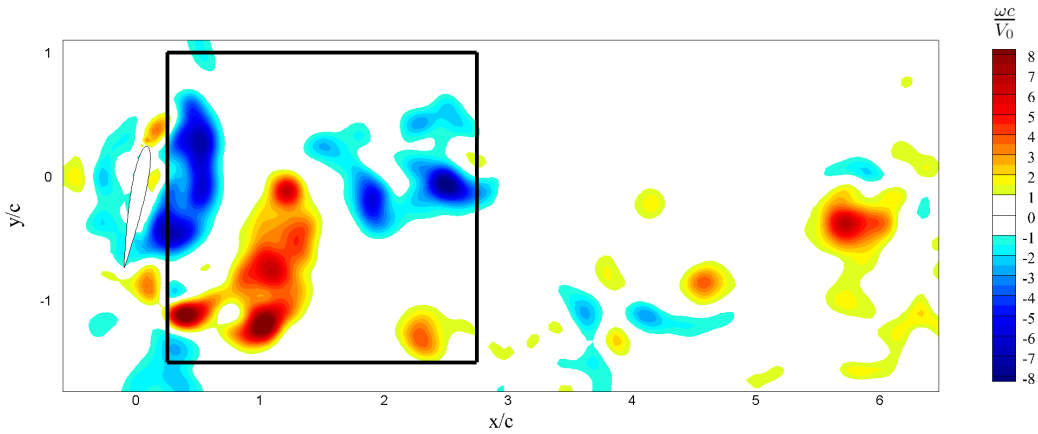

Figure 5.19: The region used to estimate the pressure on flapping airfoil at Re=1000 shown on non-dimensional out-of-plane vorticity contour, retrieved from [96].

$\Delta t = 0.625$ s. The region of interest is a square with an edge of 150 mm. The velocity data is interpolated on a 240×240 grid that results a grid spacing of 0.625 mm.

The estimated pressure contours with various spatial discretization schemes are compared in Figure 5.20. Upper two row shows TVD schemes with different limiters and central differencing scheme. The lowest row includes the results of first order hybrid differencing, power-law and upwind schemes. The highest pressure is chosen to be zero in the region of interest as previously mentioned, thus all remaining pressure values are assigned relative to this value.

The general topology and pressure magnitudes are captured similarly with all schemes experimented on 240×240 grid. On the other hand, slight deviations are observed in low pressure gradient regions which may be related with the relative dominance of the numerical errors against the change in pressure. Figure 5.21 shows the variation of pressure along the line passing through $x/c = 1.32$ in pressure contours given by Figure 5.20. A slight deviation is observed at locations greater than $y/c > 0.2$ where the pressure gradient is lower. With the given characteristic values, the dynamic pressure of the flow is calculated as $q_0 = \frac{1}{2}\rho V_0 = 0.1388$ Pa. Then, the pressure difference between the maximum and minimum values in the region of interest becomes $\Delta C_P \approx 4.7$ which is an expected value for similar cases.

The flux limiters do not show any difference in the final pressure estimation as previously noted. This could be also observed in Figure 5.22 where all TVD scheme

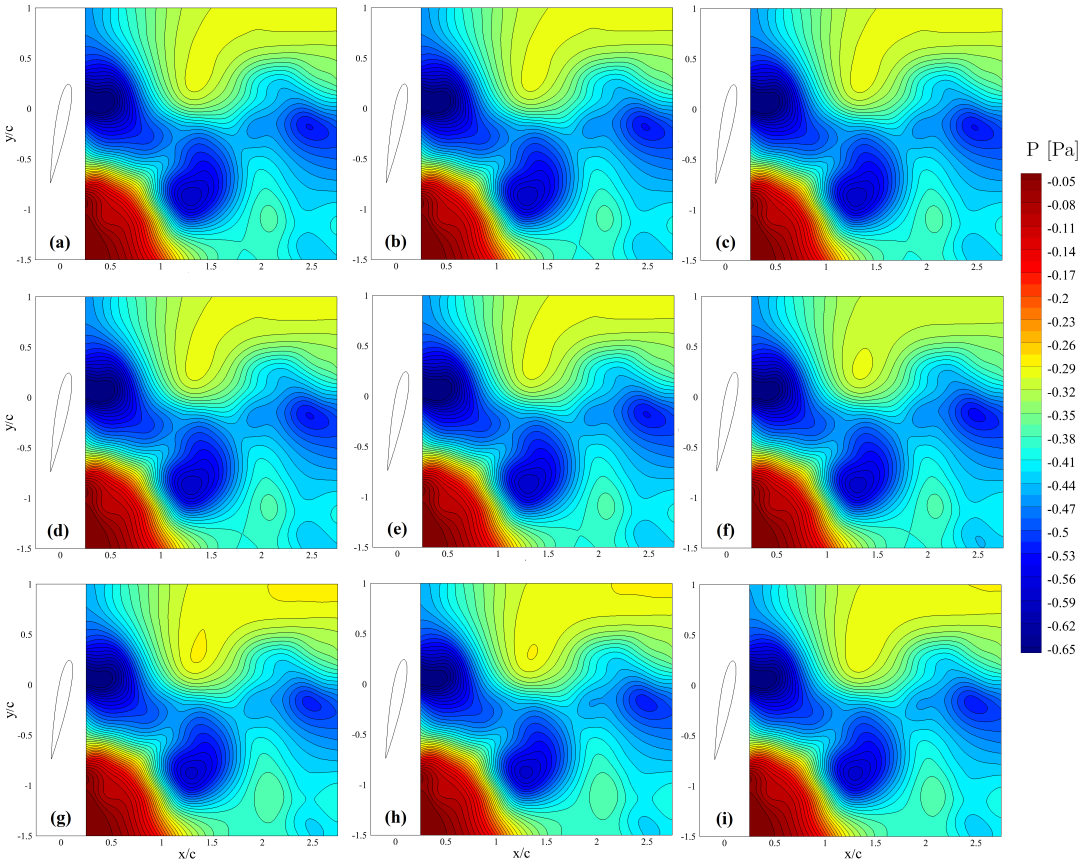

Figure 5.20: Contours of estimated pressure with (a) van Leer limiter, (b) SUPER-BEE, (c) Sweby limiter, (d) QUICK, (e) UMIST limiter, (f) central differencing, (g) hybrid differencing, (h) power-law and (i) upwind differencing schemes.

lines are overlapping. Thus, further studies are conducted with third-order QUICK scheme. Figure 5.22 compares the flow-field from PIV measurement with the resulting flow-field of current pressure estimation methodology. The upper two row of contours show the normalized $u-$ and $v-$velocity distributions, whereas the lower two rows show normalized Q and vorticity contours. The streamlines are also shown on the non-dimensional vorticity contours. At the first glance, both flow-fields seem to be similar qualitatively and quantitatively. A deeper look in Q-contours reveals that the flow-field from pressure estimation methodology is more diffusive than PIV flow-field. Vortex centers are found to be slightly stronger and more concentrated in the PIV results. The velocity contours do not show a systematic difference but in terms of streamwise velocity component the pressure estimation procedure flow-field is following a more continuous trend than the PIV flow-field. Rather than these

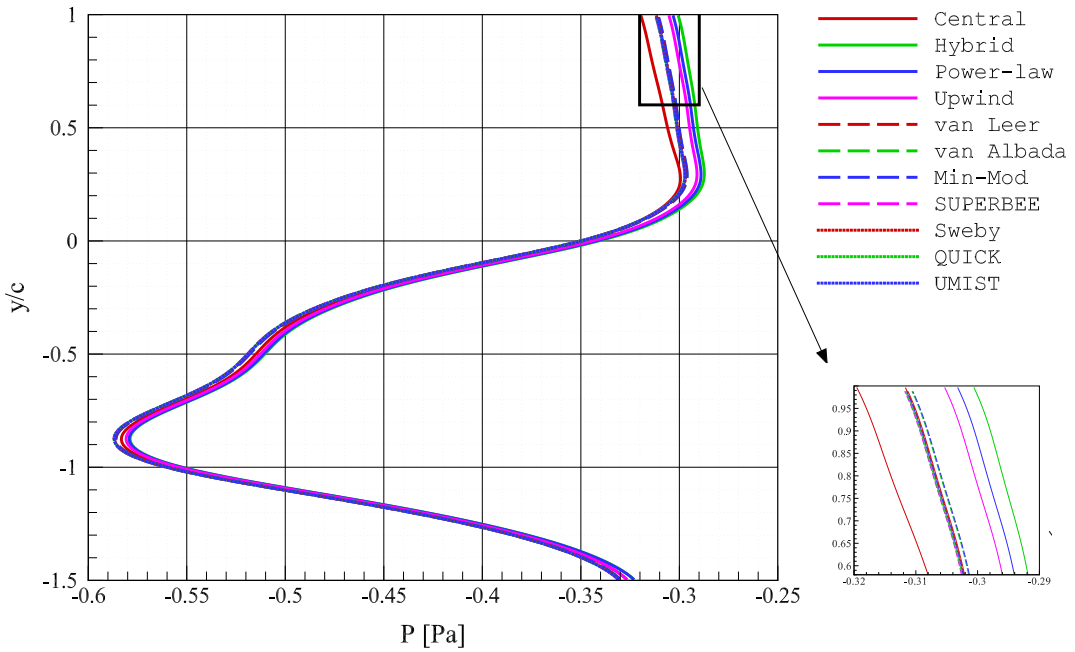

Figure 5.21: Estimated pressure values with different schemes along the line passing through $x/c = 1.32$.

minor differences, one can conclude that pressure estimation procedure does not alter the acquired flow-field but forces it to obey governing equations. With the help of this behavior, in further studies this methodology could also be used as a method for characterizing the uncertainty and accuracy of PIV experiments through use of well-known canonical flows.

Figure 5.24 shows the general three-dimensional critical point definitions. Keeping in mind these definitions, from the streamline comparison of Figure 5.22 one could see that the vortices of PIV flow-field are in focus form whereas for the pressure estimation methodology the vortices are forming centers. Even if the flow is two-dimensional in PIV experiments with end-plates, the vortices are formed as three-dimensional vortex sheet roll-ups. Thus, the streamlines of PIV experiments will be in focus form as a slice of the three-dimensional vortex sheet roll-up. On top of it, pressure estimation methodology captures a weak vortex on the top right where it is denoted as a repelling node in the PIV flow-field. The spatial resolution of the PIV system is not adequate to capture this vortex.

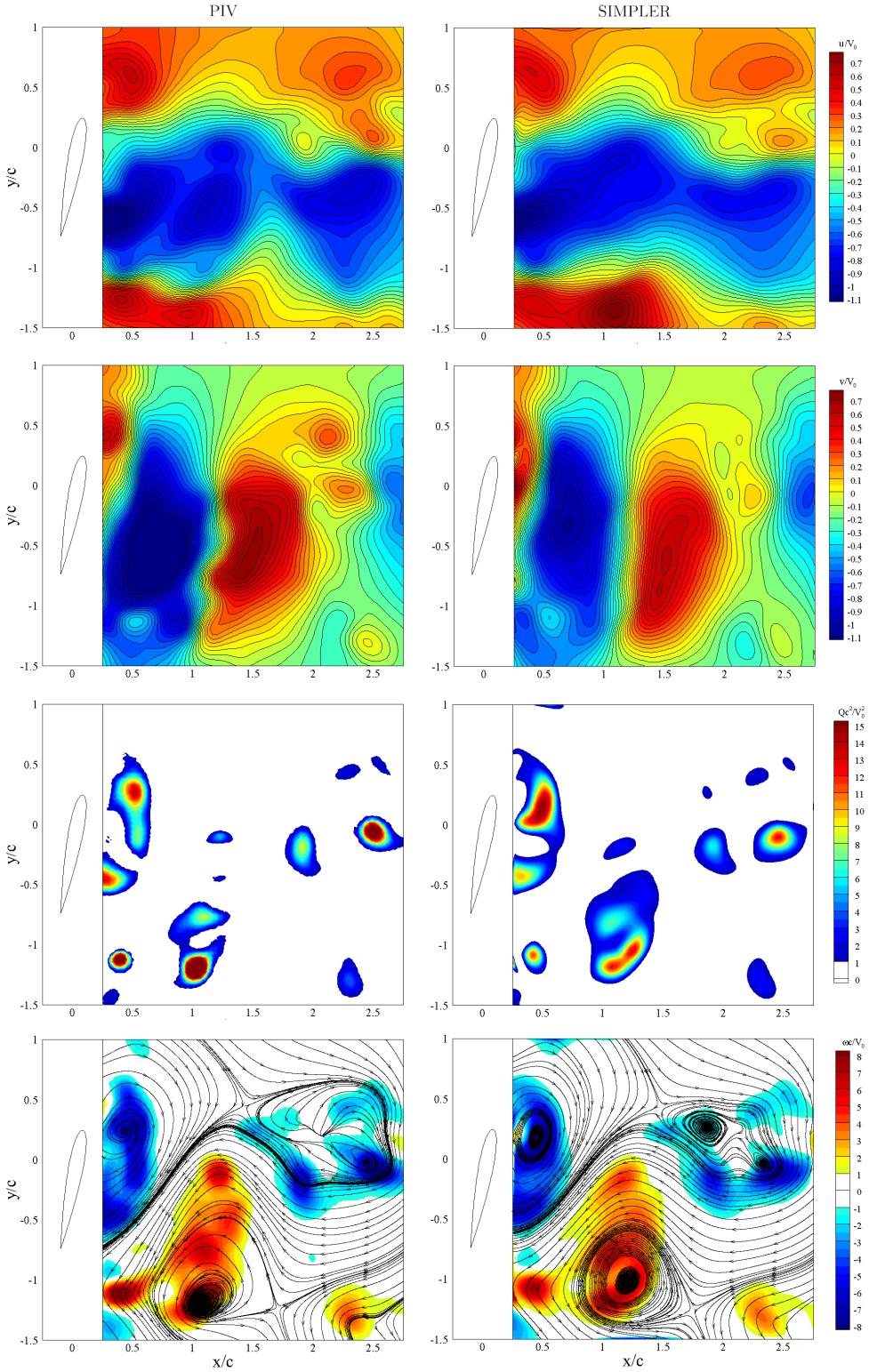

Figure 5.22: Non-dimensional u, v, Q and ω contours of PIV measurements (*left column*) and current methodology solutions (*right column*).

Figure 5.22 shows that flow-fields from PIV and SIMPLER are quantitatively and qualitatively close. The major distinction between these two flow-fields could be the stronger vortex structures in PIV flow-field. Comparison of Q contours can reveal the stronger and more concentrated vortex structures of PIV flow-field. To characterize the source of differences in velocity outputs, several combinations of velocity derivatives are studied. It should be noted that velocity components are the only outputs of PIV, thus further analyses on these variables will lead to additional conclusions. The difference in velocity magnitudes between two methods are calculated as

$$\Delta V = \sqrt{(u^{\text{PIV}} - u^{\text{SIMPLER}})^2 + (v^{\text{PIV}} - v^{\text{SIMPLER}})^2} \tag{5.12}$$

where the superscripts ^{PIV} and ^{SIMPLER} denote the velocity components measured in PIV experiments and computed from pressure estimation procedure based on SIMPLER algorithm.

The velocity magnitude difference, given by Eqn. 5.12, is plotted on the left of Figure 5.23. The right contour of the same figure shows the mass imbalance in PIV experiments which is given by $\frac{\partial u}{\partial x} + \frac{\partial v}{\partial y}$. The main aim of whole pressure estimation methodology is to zero out this mass imbalance term. This mass imbalance term in pressure estimation methodology is only composed of numerical errors and negligible with respect to its experimental counterpart.

The mass imbalance in the PIV experiments are mostly dominant in the regions of high velocity gradients. Practically, a PIV interrogation window should include 10 to 25 particles to calculate the velocity vector. All particles in the interrogation window are processed together to achieve one velocity vector located at the center of interrogation window. This process will give correct velocity vector, if all particles in same interrogation window move with same velocity. When high velocity gradients exist in an interrogation window, there will be an error in velocity measurement [99]. This is one of the most significant points to be considered while setting the experimental arrangement for PIV. The higher velocity gradients occur at the vortex regions which could be seen in Figure 5.22. Thus, mass imbalance will mostly occur at these high vorticity regions due to the nature of the experimental methodology. This behavior could also be observed in Figure 5.23 where the velocity gradients are smaller. At

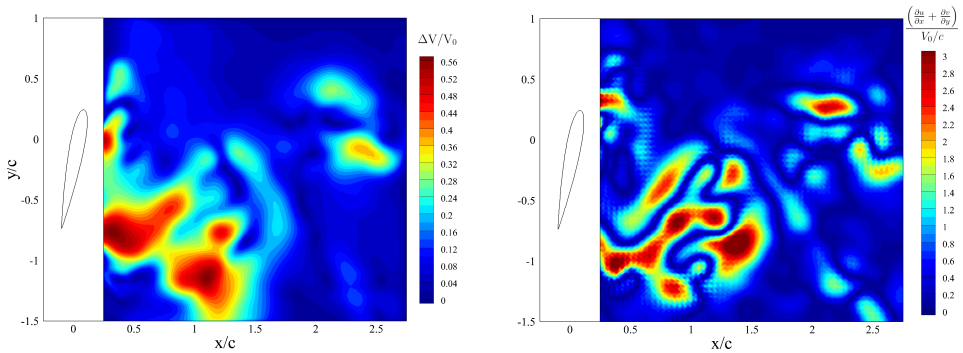

Figure 5.23: Normalized velocity difference between PIV measurement and pressure estimation procedure (*left*) and non-dimensional mass imbalance in PIV measurements (*right*).

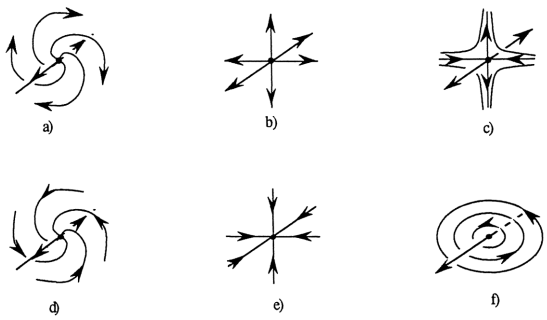

Figure 5.24: Three dimensional critical points, (a) repelling focus, (b) repelling node, (c) saddle, (d) attracting focus, (e) attracting node and (f) center, depicted from Ref. [100].

those regions, resolution of PIV is adequate to resolve the velocities accurately, so not a significant mass imbalance is observed.

PIV technique, by its nature, does not satisfy the continuity. Thus, current pressure estimation methodology not only provides an extra flow variable to PIV technique but also improves already measured ones. This study also shows that current methodology could also be used as a characterization tool for PIV systems in terms of uncertainty and accuracy. Similarly, current methodology could also be used to fill missing velocity vectors in PIV experiments by using available velocity information.

CHAPTER 6

CONCLUSIONS

The aim of the thesis is to develop a universal pressure estimation methodology that does not require extensive data manipulation in terms of boundary condition implementation and possesses error-correcting behavior. To achieve this, a methodology based on SIMPLER algorithm is employed on planar PIV experiments. Experimental velocity data is first interpolated on a staggered grid and used as an initial condition to the problem. Then, continuity equation, in the form of pressure equation for incompressible flows, is solved with this velocity field to have an initial pressure field. Momentum equations are solved with calculated pressure field and then pressure correction equation is solved for calculating the mass imbalance in continuity equation. Using this mass imbalance term, current velocity field is corrected. Repeating this procedure until convergence provides not only pressure field satisfying governing equations, but also the corrections on measured velocity data to force continuity. This corrective behavior promises more than just estimating pressure, such as quantifying the uncertainties in PIV system, assessing the error sensitivity of the experiments, calibrating numerical tools or filling missing data in PIV experiments.

The proposed method is originally developed for steady and transient laminar flows. Special attention is paid on forming higher order discretization schemes for calculations, since the method may also be used for further sensitivity analysis of existing PIV systems. After describing the method in details, it is validated with theoretical/numerical steady and transient flows. Method estimates the pressure field exactly -with minor truncation errors- for error free input velocity fields. Error-correcting capabilities of the proposed method is further tested via introducing artificial error to the theoretical flows. It is shown that even with extremely high experimental uncer-

tainties, the method can correct the flow-field to very accurate values. The effect of time-step is also tested and it is observed that error in the flow-field is reducing until a certain value with decreasing time-step. After converging to this case-specific value, no further accuracy improvement is observed.

The pressure estimation results of the methodology is also compared with conventional tools. The mean pressure field around a two-dimensional cylinder is measured with a five-hole probe. The two-dimensionality and accuracy of five-hole probe measurements are also assessed to achieve accurate comparisons. It is seen that the five hole probe and PIV pressure results agree well. It is significant to note that conventional multi hole probes are sensitive to the flow direction and could not be employed to reverse flows for accurate measurements. The non-intrusive nature of current methodology allows to have accurate pressure measurements even in highly vortical flows. This behavior is further tested via estimating pressure field around a flapping wing airfoil. It is observed that the discretization schemes do not introduce a significant difference in final pressure estimation. On the other hand, the corrections on experimental velocity fields are found to be related with the mass imbalance in the PIV velocity fields and inherent velocity gradients in PIV interrogation windows at high vorticity regions. As previously mentioned, in PIV experiments all particles in the same interrogation window are assumed to move with the same velocity. This assumption contradicts with any non-zero velocity gradient in interrogation windows and introduces an error in continuity. In addition to measuring an extra flow variable, proposed method could also enhance measured velocity fields by forcing them to obey governing equations. Moreover, the method could also be employed to assess the uncertainties in PIV arrangements or could be used for calibration purposes.

The method uses outer velocity values as boundary conditions and do not correct them with progressing iterations. This brings the relatively small residual errors in final estimation. To further improve the quality of final estimation, one may start with a wider domain of interest for initial pressure estimation. Then, using the corrected flow-field, another estimation could be performed by excluding the outermost cells which are not corrected.

The proposed pressure estimation method is described for two-dimensional, laminar

flows, but it could easily be extended to three-dimensional flows as shown in section 3.3 for tomographic PIV experiments. For laminar flows, Navier-Stokes equations could be solved directly without any modeling and that brings the strength to the current procedure. If current method is extended to turbulent flows, certain eddy viscosity models should be included to the procedure. Due to the structural similarities of LES and PIV, implementation of subgrid-scale modeling to the proposed methodology stands as a potential candidate. On the other hand, implementing turbulence models will lead to question the exactness of pressure estimation. Still, this attempt should be studied as a future work alongside with high-fidelity LES comparisons.

REFERENCES

[1] Gurka, R., Liberzon, A., Hefetz, D., Rubinstein, D., and Shavit, U., "Computation of pressure distribution using PIV velocity data," *Workshop on particle image velocimetry*, Vol. 2, 1999.

[2] Baur, T. and Kongeter, J., "PIV with high temporal resolution for the determination of local pressure reductions ffrom coherent turbulence phenomena," *Proceedings of the Third International Workshop on PIV*, Hosted by the University of California, Santa-Barbara, Sept. 1999.

[3] Jaw, S. Y., Chen, J. H., and Wu, P. C., "Measurement of pressure distribution from PIV experiments," *Journal of Visualization*, Vol. 12, No. 1, 2009, pp. 27–35.

[4] Hosokawa, S., Moriyama, S., Tomiyama, A., and Takada, N., "PIV Measurement of Pressure Distributions about Single Bubbles," *Journal of Nuclear Science and Technology*, Vol. 40, No. 10, 2003, pp. 754–762.

[5] Jeon, Y. J., Chatellier, L., and David, L., "Fluid trajectory evaluation based on an ensemble-averaged cross-correlation in time-resolved PIV," *Experiments in Fluids*, Vol. 55, No. 7, Jun 2014, pp. 1766.

[6] McClure, J. and Yarusevych, S., "Optimization of planar PIV-based pressure estimates in laminar and turbulent wakes," *Experiments in Fluids*, Vol. 58, No. 5, 2017, pp. 62.

[7] McClure, J. and Yarusevych, S., "Instantaneous PIV/PTV-based pressure gradient estimation: a framework for error analysis and correction," *Experiments in Fluids*, Vol. 58, No. 8, Jul 2017, pp. 92.

[8] Okuno, T., Sugii, Y., and Nishio, S., "Image measurement of flow field using physics-based dynamic model," *Measurement Science and Technology*, Vol. 11, No. 6, 2000, pp. 667.

[9] Dong, P., Hsu, T.-Y., Atsavapranee, P., and Wei, T., "Digital particle image accelerometry," *Experiments in Fluids*, Vol. 30, No. 6, Jun 2001, pp. 626–632.

[10] Liu, X. and Katz, J., "Measurements of pressure distribution in a cavity flow by integrating the material acceleration," *ASME 2004 Heat Transfer/Fluids Engineering Summer Conference*, No. 4692X, American Society of Mechanical Engineers, 2004, pp. 621–631.

[11] Liu, X. and Katz, J., "Instantaneous pressure and material acceleration measurements using a four-exposure PIV system," *Experiments in Fluids*, Vol. 41, No. 2, May 2006, pp. 227.

[12] Jensen, A., Sveen, J. K., Grue, J., Richon, J.-B., and Gray, C., "Accelerations in water waves by extended particle image velocimetry," *Experiments in Fluids*, Vol. 30, No. 5, May 2001, pp. 500–510.

[13] Freitas, C. J., Street, R. L., Findikakis, A. N., and Koseff, J. R., "Numerical simulation of three-dimensional flow in a cavity," *International Journal for Numerical Methods in Fluids*, Vol. 5, No. 6, 1985, pp. 561–575.

[14] Fujisawa, N., Tanahashi, S., and Srinivas, K., "Evaluation of pressure field and fluid forces on a circular cylinder with and without rotational oscillation using velocity data from PIV measurement," *Measurement Science and Technology*, Vol. 16, No. 4, 2005, pp. 989.

[15] Lynch, K. P. and Scarano, F., "Material acceleration estimation by four-pulse tomo-PIV," *Measurement Science and Technology*, Vol. 25, No. 8, 2014, pp. 084005.

[16] Schneiders, J. F. G., Avallone, F., Pröbsting, S., Ragni, D., and Scarano, F., "Pressure spectra from single-snapshot tomographic PIV," *Experiments in Fluids*, Vol. 59, No. 3, Feb 2018, pp. 57.

[17] Charonko, J. J., King, C. V., Smith, B. L., and Vlachos, P. P., "Assessment of pressure field calculations from particle image velocimetry measurements," *Measurement Science and Technology*, Vol. 21, No. 10, 2010, pp. 105401.

[18] Pan, Z., Whitehead, J., Thomson, S., and Truscott, T., "Error propagation dynamics of PIV-based pressure field calculations: How well does the pressure Poisson solver perform inherently?" *Measurement Science and Technology*, Vol. 27, No. 8, 2016, pp. 084012.

[19] van Gent, P. L., Schrijer, F. F. J., and van Oudheusden, B. W., "Assessment of the pseudo-tracking approach for the calculation of material acceleration and pressure fields from time-resolved PIV: part I. Error propagation," *Measurement Science and Technology*, Vol. 29, No. 4, 2018, pp. 045204.

[20] van Gent, P. L., Michaelis, D., van Oudheusden, B. W., Weiss, P. É., de Kat, R., Laskari, A., Jeon, Y. J., David, L., Schanz, D., Huhn, F., Gesemann, S., Novara, M., McPhaden, C., Neeteson, N. J., Rival, D. E., Schneiders, J. F. G., and Schrijer, F. F. J., "Comparative assessment of pressure field reconstructions from particle image velocimetry measurements and Lagrangian particle tracking," *Experiments in Fluids*, Vol. 58, No. 4, Mar 2017, pp. 33.

[21] Wang, Z., Gao, Q., Wei, R., and Wang, J., "Error propagation in the procedure of pressure reconstruction based on PIV data," *Journal of Physics: Conference Series*, Vol. 822, No. 1, 2017, pp. 012055.

[22] Azijli, I., Sciacchitano, A., Ragni, D., Palha, A., and Dwight, R. P., "A posteriori uncertainty quantification of PIV-based pressure data," *Experiments in Fluids*, Vol. 57, No. 5, Apr 2016, pp. 72.

[23] Wang, Z., Gao, Q., Wang, C., Wei, R., and Wang, J., "An irrotation correction on pressure gradient and orthogonal-path integration for PIV-based pressure reconstruction," *Experiments in Fluids*, Vol. 57, No. 6, June 2016, pp. 1.

[24] Patankar, S. and Spalding, D., "A calculation procedure for heat, mass and momentum transfer in three-dimensional parabolic flows," *International Journal of Heat and Mass Transfer*, Vol. 15, No. 10, 1972, pp. 1787 – 1806.

[25] Patankar, S. V., "A Calculation Procedure for Two-Dimensional Elliptic Situations," *Numerical Heat Transfer*, Vol. 4, No. 4, 1981, pp. 409–425.

[26] Schanz, D., Gesemann, S., and Schröder, A., "Shake-The-Box: Lagrangian particle tracking at high particle image densities," *Experiments in Fluids*, Vol. 57, No. 5, Apr 2016, pp. 70.

[27] Gesemann, S., Huhn, F., Schanz, D., and Schröder, A., "From Noisy Particle Tracks to Velocity, Acceleration and Pressure Fields using B-splines and Penalties," *18th International Symposium on the Application of Laser and Imaging Techniques to Fluid Mechanics*, July 4 – 7, 2016.

[28] Schneiders, J. F. G. and Scarano, F., "Dense velocity reconstruction from tomographic PTV with material derivatives," *Experiments in Fluids*, Vol. 57, No. 9, Aug 2016, pp. 139.

[29] Huhn, F., Schanz, D., Gesemann, S., and Schröder, A., "FFT integration of instantaneous 3D pressure gradient fields measured by Lagrangian particle tracking in turbulent flows," *Experiments in Fluids*, Vol. 57, No. 9, Sep 2016, pp. 151.

[30] Neeteson, N. J. and Rival, D. E., "Pressure-field extraction on unstructured flow data using a Voronoi tessellation-based networking algorithm: a proof-of-principle study," *Experiments in Fluids*, Vol. 56, No. 2, Feb 2015, pp. 44.

[31] Neeteson, N. J., Bhattacharya, S., Rival, D. E., Michaelis, D., Schanz, D., and Schröder, A., "Pressure-field extraction from Lagrangian flow measurements: first experiences with 4D-PTV data," *Experiments in Fluids*, Vol. 57, No. 6, Jun 2016, pp. 102.

[32] Stüer, H. and Blaser, S., "Interpolation of Scattered 3D PTV Data to a Regular Grid," *Flow, Turbulence and Combustion*, Vol. 64, No. 3, Jul 2000, pp. 215–232.

[33] Russo, G. P., *Aerodynamic measurements: from physical principles to turnkey instrumentation*, Woodhead Publishing, 2011.

[34] Willert, C. E. and Gharib, M., "Digital particle image velocimetry," *Experiments in Fluids*, Vol. 10, No. 4, Jan 1991, pp. 181–193.

[35] Adrian, R. J. and Westerweel, J., *Particle image velocimetry*, No. 30, Cambridge University Press, 2011.

[36] Raffel, M., Willert, C. E., Scarano, F., Kähler, C. J., Wereley, S. T., and Kompenhans, J., *Particle image velocimetry: A practical guide*, Springer International Publishing, 2018.

[37] DANTEC, "Measurement Principles of PIV," www.dantecdynamics.com, Accessed: September-2018.

[38] La Porta, A., Voth, G. A., Crawford, A. M., Alexander, J., and Bodenschatz, E., "Fluid particle accelerations in fully developed turbulence," *Nature*, Vol. 409, No. 6823, 2001, pp. 1017.

[39] Dabiri, J. O., Bose, S., Gemmell, B. J., Colin, S. P., and Costello, J. H., "An algorithm to estimate unsteady and quasi-steady pressure fields from velocity field measurements," *Journal of Experimental Biology*, Vol. 217, No. 3, 2014, pp. 331–336.

[40] Liu, X., Moreto, J. R., and Siddle-Mitchell, S., "Instantaneous pressure reconstruction from measured pressure gradient using rotating parallel ray method," *54th AIAA Aerospace Sciences Meeting*, 2016, p. 1049.

[41] Liu, X. and Katz, J., "Measurements of pressure distribution by integrating the material acceleration," *Cav03-GS-14-001, Fifth international symposium on cavitation (CAV2003), Osaka, Japan*, 2003, pp. 1–4.

[42] Liu, X. and Katz, J., "Cavitation phenomena occurring due to interaction of shear layer vortices with the trailing corner of a two-dimensional open cavity," *Physics of Fluids*, Vol. 20, No. 4, 2008, pp. 041702.

[43] Liu, X. and Katz, J., "Vortex-corner interactions in a cavity shear layer elucidated by time-resolved measurements of the pressure field," *Journal of Fluid Mechanics*, Vol. 728, 2013, pp. 417–457.

[44] Ghaemi, S., Ragni, D., and Scarano, F., "PIV-based pressure fluctuations in the turbulent boundary layer," *Experiments in Fluids*, Vol. 53, No. 6, Dec 2012, pp. 1823–1840.

[45] van Oudheusden, B. W., Scarano, F., Roosenboom, E. W. M., Casimiri, E. W. F., and Souverein, L. J., "Evaluation of integral forces and pressure fields from planar velocimetry data for incompressible and compressible flows," *Experiments in Fluids*, Vol. 43, No. 2, 2007, pp. 153–162.

[46] Violato, D., Moore, P., and Scarano, F., "Lagrangian and Eulerian pressure field evaluation of rod-airfoil flow from time-resolved tomographic PIV," *Experiments in Fluids*, Vol. 50, No. 4, Apr 2011, pp. 1057–1070.

[47] Glowinski, R. and Pironneau, O., "On a mixed finite element approximation of the Stokes problem (I)," *Numerische Mathematik*, Vol. 33, No. 4, Dec 1979, pp. 397–424.

[48] Auteri, F., Carini, M., Zagaglia, D., Montagnani, D., Gibertini, G., Merz, C. B., and Zanotti, A., "A novel approach for reconstructing pressure from PIV velocity measurements," *Experiments in Fluids*, Vol. 56, No. 2, Feb 2015, pp. 45.

[49] Hirt, C. W., "SOLA : A Numerical Solution Algorithm for Transient Fluid Flows," *LA-5852*, 1975.

[50] Patankar, S. V., *Numerical heat transfer and fluid flow*, Series on Computational Methods in Mechanics and Thermal Science, Hemisphere Publishing Corporation (CRC Press, Taylor & Francis Group), 1980.

[51] Versteeg, H. and Malalasekera, W., *An Introduction to Computational Fluid Dynamics: The Finite Volume Method*, Pearson Education Limited, 2007.

[52] Ferziger, J. and Peric, M., *Computational Methods for Fluid Dynamics*, Springer Berlin Heidelberg, 2001.

[53] Anderson, D. A., Pletcher, R. H., and Tannehill, J. C., *Computational fluid mechanics and heat transfer*, CRC Press, Taylor & Francis Group, 2013.

[54] Charonko, J. J. and Vlachos, P. P., "Estimation of uncertainty bounds for individual particle image velocimetry measurements from cross-correlation peak ratio," *Measurement Science and Technology*, Vol. 24, No. 6, 2013, pp. 065301.

[55] Neal, D. R., Sciacchitano, A., Smith, B. L., and Scarano, F., "Collaborative framework for PIV uncertainty quantification: the experimental database," *Measurement Science and Technology*, Vol. 26, No. 7, 2015, pp. 074003.

[56] Sciacchitano, A., Wieneke, B., and Scarano, F., "PIV uncertainty quantification by image matching," *Measurement Science and Technology*, Vol. 24, No. 4, 2013, pp. 045302.

[57] Sciacchitano, A., Neal, D. R., Smith, B. L., Warner, S. O., Vlachos, P. P., Wieneke, B., and Scarano, F., "Collaborative framework for PIV uncertainty quantification: comparative assessment of methods," *Measurement Science and Technology*, Vol. 26, No. 7, 2015, pp. 074004.

[58] Sciacchitano, A. and Wieneke, B., "PIV uncertainty propagation," *Measurement Science and Technology*, Vol. 27, No. 8, 2016, pp. 084006.

[59] Wieneke, B., "PIV uncertainty quantification from correlation statistics," *Measurement Science and Technology*, Vol. 26, No. 7, 2015, pp. 074002.

[60] Boomsma, A., Bhattacharya, S., Troolin, D., Pothos, S., and Vlachos, P., "A comparative experimental evaluation of uncertainty estimation methods for two-component PIV," *Measurement Science and Technology*, Vol. 27, No. 9, 2016, pp. 094006.

[61] Bhattacharya, S., Charonko, J. J., and Vlachos, P. P., "Stereo-particle image velocimetry uncertainty quantification," *Measurement Science and Technology*, Vol. 28, No. 1, 2017, pp. 015301.

[62] Scarborough, J., *Numerical Mathematical Analysis*, Johns Hopkins Press, 1958.

[63] Spalding, D. B., "A novel finite difference formulation for differential expressions involving both first and second derivatives," *International Journal for Numerical Methods in Engineering*, Vol. 4, No. 4, 1972, pp. 551–559.

[64] Leonard, B., "A stable and accurate convective modelling procedure based on quadratic upstream interpolation," *Computer Methods in Applied Mechanics and Engineering*, Vol. 19, No. 1, 1979, pp. 59 – 98.

[65] Leschziner, M., "Practical evaluation of three finite difference schemes for the computation of steady-state recirculating flows," *Computer Methods in Applied Mechanics and Engineering*, Vol. 23, No. 3, 1980, pp. 293 – 312.

[66] Han, T., Humphrey, J., and Launder, B., "A comparison of hybrid and quadratic-upstream differencing in high Reynolds number elliptic flows," *Computer Methods in Applied Mechanics and Engineering*, Vol. 29, No. 1, 1981, pp. 81 – 95.

[67] Pollard, A. and Siu, A. L.-W., "The calculation of some laminar flows using various discretisation schemes," *Computer Methods in Applied Mechanics and Engineering*, Vol. 35, No. 3, 1982, pp. 293 – 313.

[68] Perng, C.-Y. and Street, R. L., "Three-dimensional unsteady flow simulations: Alternative strategies for a volume-averaged calculation," *International Journal for Numerical Methods in Fluids*, Vol. 9, No. 3, 1989, pp. 341–362.

[69] Hayase, T., Humphrey, J., and Greif, R., "A consistently formulated QUICK scheme for fast and stable convergence using finite-volume iterative calculation procedures," *Journal of Computational Physics*, Vol. 98, No. 1, 1992, pp. 108 – 118.

[70] Sweby, P. K., "High resolution schemes using flux limiters for hyperbolic conservation laws," *SIAM journal on numerical analysis*, Vol. 21, No. 5, 1984, pp. 995–1011.

[71] Harten, A., "High resolution schemes for hyperbolic conservation laws," *Journal of Computational Physics*, Vol. 49, No. 3, 1983, pp. 357 – 393.

[72] Godunov, S. K., "A difference method for numerical calculation of discontinuous solutions of the equations of hydrodynamics," *Matematicheskii Sbornik*, Vol. 89, No. 3, 1959, pp. 271–306.

[73] Warming, R. F. and Beam, R. M., "Upwind Second-Order Difference Schemes and Applications in Aerodynamic Flows," *AIAA Journal*, Vol. 14, No. 9, Sept. 1976, pp. 1241–1249.

[74] Lax, P. and Wendroff, B., "Systems of conservation laws," *Communications on Pure and Applied Mathematics*, Vol. 13, No. 2, 1960, pp. 217–237.

[75] van Leer, B., "Towards the ultimate conservative difference scheme. II. Monotonicity and conservation combined in a second-order scheme," *Journal of Computational Physics*, Vol. 14, No. 4, 1974, pp. 361 – 370.

[76] Roe, P. L., "Some contributions to the modelling of discontinuous flows," *Lectures in Applied Mathematics*, Vol. 22, 1985, pp. 163–193.

[77] van Albada, G. D., van Leer, B., and Roberts, Jr., W. W., "A comparative study of computational methods in cosmic gas dynamics," *Astronomy and Astrophysics*, Vol. 108, April 1982, pp. 76–84.

[78] Lien, F.-S. and Leschziner, M., "Upstream monotonic interpolation for scalar transport with application to complex turbulent flows," *International Journal for Numerical Methods in Fluids*, Vol. 19, No. 6, 1994, pp. 527–548.

[79] Harten, A. and Osher, S., "Uniformly high-order accurate nonoscillatory schemes. I," *SIAM Journal on Numerical Analysis*, Vol. 24, No. 2, 1987, pp. 279–309.

[80] Koren, B., *A robust upwind discretization method for advection, diffusion and source terms*, Centrum voor Wiskunde en Informatica Amsterdam, 1993.

[81] Van Leer, B., "Towards the ultimate conservative difference scheme III. Upstream-centered finite-difference schemes for ideal compressible flow," *Journal of Computational Physics*, Vol. 23, No. 3, 1977, pp. 263–275.

[82] Elsinga, G. E., Scarano, F., Wieneke, B., and van Oudheusden, B. W., "Tomographic particle image velocimetry," *Experiments in Fluids*, Vol. 41, No. 6, Dec 2006, pp. 933–947.

[83] Scarano, F., "Tomographic PIV: principles and practice," *Measurement Science and Technology*, Vol. 24, No. 1, 2013, pp. 012001.

[84] Harlow, F. H. and Welch, J. E., "Numerical Calculation of Time-Dependent Viscous Incompressible Flow of Fluid with Free Surface," *The Physics of Fluids*, Vol. 8, No. 12, 1965, pp. 2182–2189.

[85] Murai, Y., Nakada, T., Suzuki, T., and Yamamoto, F., "Particle tracking velocimetry applied to estimate the pressure field around a Savonius turbine," *Measurement Science and Technology*, Vol. 18, No. 8, 2007, pp. 2491.

[86] Thomas, L. H., "Elliptic Problems in Linear Differential Equations over a Network," Tech. rep., Columbia University, 1949.

[87] ANSYS® Fluent, Release 14.5.

[88] Gomit, G., Acher, G., Chatellier, L., and David, L., "Uncertainty analysis of an optical method for pressure estimation in fluid flows," *Measurement Science and Technology*, Vol. 29, No. 2, 2018, pp. 024004.

[89] Walpole, R. E., Myers, R. H., Myers, S. L., and Ye, K., *Probability and statistics for engineers and scientists*, Vol. 5, Macmillan New York, 1993.

[90] Kurtulus, D. F., Scarano, F., and David, L., "Unsteady aerodynamic forces estimation on a square cylinder by TR-PIV," *Experiments in Fluids*, Vol. 42, No. 2, 2007, pp. 185–196.

[91] Treaster, A. L. and Yocum, A. M., "The calibration and application of five-hole probes," *ISA Transactions*, Vol. 18, No. 3, 1979, pp. 23–34.

[92] Morrison, G., Schobeiri, M., and Pappu, K., "Five-hole pressure probe analysis technique," *Flow Measurement and Instrumentation*, Vol. 9, No. 3, 1998, pp. 153 – 158.

[93] Ramakrishnan, V. and Rediniotis, O. K., "Development of a 12-Hole Omnidirectional Flow-Velocity Measurement Probe," *AIAA Journal*, Vol. 45, No. 6, June 2007, pp. 1430–1432.

[94] Wang, H., Zeng, W., and Zhang, Q., "Development of an Omnidirectional Five-Hole Pressure Probe," *AIAA Journal*, Vol. 54, No. 7, July 2016, pp. 2190–2193.

[95] Wang, H., Chen, X., and Zhao, W., "Development of a 17-Hole Omnidirectional Pressure Probe," *AIAA Journal*, Vol. 50, No. 6, June 2012, pp. 1426–1430.

[96] Kurtulus, D. F., *Numerical and Experimental Analysis of Flapping Motion in Hover, Application to Micro Air Vehicles*, Ph.D. thesis, Joint Ph.D thesis Poitiers University/ENSMA (Poitiers France) and METU (Ankara-Turkey),, 2005.

[97] Hunt, J. C. R., Wray, A. A., and Moin, P., "Eddies, streams, and convergence zones in turbulent flows," *Studying Turbulence Using Numerical Simulation Databases, 2*, Dec. 1988.

[98] Kurtulus, D. F., David, L., Farcy, A., and Alemdaroglu, N., "Aerodynamic characteristics of flapping motion in hover," *Experiments in Fluids*, Vol. 44, No. 1, Jan 2008, pp. 23–36.

[99] Westerweel, J., "On velocity gradients in PIV interrogation," *Experiments in Fluids*, Vol. 44, No. 5, May 2008, pp. 831–842.

[100] Hagen, H., Müller, H., and Nielson, G., *Focus on scientific visualization*, Springer Science & Business Media, 1993.

CURRICULUM VITAE

PERSONAL INFORMATION

Surname, Name	:	Günaydınoğlu, Erkan
Nationality	:	Turkish
Date and Place of Birth	:	January 1986, Beyoğlu
Phone	:	+90 533 4824013
E-mail	:	erk@erk.aero, gunaydin@ae.metu.edu.tr

EDUCATION

Degree	**Institution**	**Year**
R.M.	VKI Aeronautics and Aerospace	2011
M.S.	METU Aerospace Engineering	2010
B.S.	METU Aerospace Engineering	2009
High School	Tekirdağ Science High School	2004

PROFESSIONAL EXPERIENCE

Year	**Place**	**Enrollment**
2018-	Turkish Aerospace Industries	Design Specialist
2012-2017	UTAA Flight Training	Lecturer

PUBLICATIONS

Journal Publications

Gökcan, M.K., Günaydinoğlu, E. and Kurtuluş, D.F., "Effect of glottic geometry on breathing: three-dimensional unsteady numerical simulation of respiration in a case

with congenital glottic web", *Eur Arch Otorhinolaryngol*, 2016, 273: 3219.

International Conference Publications

Günaydınoğlu, E., and Kurtuluş, D.F., "Two Dimensional Pressure Field Determination on Flapping Flat Plate from PIV Measurements", *Workshop on Non-Intrusive Measurements for Unsteady Flows and Aerodynamics*, Poitiers, France, 26-29 October 2015

Masutti, M., Pinna, F., Günaydınoğlu, E., Sopek, T., Chazot, O., and Rambaud, P, "Natural and Induced Transition on a 7deg Half-Cone at Mach 6", *NATO RTO AVT-200 Specialists Meeting on Hypersonic Laminar-Turbulent Transition*, San Diego, April 16-19, 2012

Masutti, D., Günaydınoğlu, E., Chazot, O., "Surface Pressure Measurements on a Flat Plate and a 7 degree Cone at Mach 6", *7th European Symposium on Aerothermodynamics for Space Vehicles*, Brugge, Belgium, 9-12 May 2011

Günaydınoğlu, E., and Kurtuluş, D.F.; "Effect of Vertical Translation on Unsteady Aerodynamics of a Hovering Airfoil", *Fifth European Conference on Computational Fluid Dynamics ECCOMAS CFD 2010*, Lisbon, Portugal, 14-17 June 2010

Günaydınoğlu, E., and Kurtuluş, D.F., "Flow Characteristics of Pitching and Plunging SD7003 Airfoil for Different Reduced Frequencies", *Ankara International Aerospace Conference, Ankara*, Turkey, 17-19 August 2009

Günaydınoğlu, E., and Kurtuluş, D.F., "Numerical Investigation of Pure Plunge and Pitch/Plunge Motions at Low Reynolds Numbers", *International Symposium of Light Weight Unmanned Aerial Vehicle Systems and Subsystems*, Ostend, Belgium, 11-13 March 2009

National Conference Publications

Günaydınoğlu, E., ve Kurtuluş, D.F., "İki Boyutlu Parçacık Görüntülemeli Hızölçer Verilerinden Basınç Alanı Tahmini", *VI. Ulusal Havacilik ve Uzay Konferansı 2016*,

Kocaeli Üniversitesi, Kocaeli, 28-30 Eylül 2016

Günaydınoğlu, E., Masutti, D. ve Chazot, O., "Hipersonik Sınır Tabakalarda Türbülansa Geçişin Deneysel Olarak İncelenmesi", *IV. Ulusal Havacilik ve Uzay Konferansi 2012*, Hava Harp Okulu, Yeşilköy, İstanbul, 12-14 Eylül 2012

Günaydınoğlu, E., ve Kurtuluş, D.F., "Çırpan Düz Levha Kesiti Etrafındaki Akışın Sayısal Yöntemlerle İncelenmesi", *5.Savunma Teknolojileri Kongresi SAVTEK 2010*, Orta Doğu Teknik Universitesi, Ankara, 23-25 Haziran 2010

Günaydınoğlu, E., ve Kurtuluş, D.F., "Reynolds sayısının Havada Asılı Sekiz Hareketi Yapan Çırpan Kanat Aerodinamiğine Etkisi", I*II. Ulusal Havacilik ve Uzay Konferansi 2010*, Anadolu Üniversitesi, Eskişehir, 16-18 Eylül 2010